

NUMERICAL STUDY OF TURBULENT
CHARACTERISTICS AND AERATION PATTERNS IN
BREAKING SURGE WAVES

ZHUORAN LI

A THESIS SUBMITTED TO
THE FACULTY OF GRADUATE STUDIES
IN PARTIAL FULFILLMENT OF THE REQUIREMENTS
FOR THE DEGREE OF
MASTER OF APPLIED SCIENCE

GRADUATE PROGRAMME IN CIVIL ENGINEERING
YORK UNIVERSITY
TORONTO, ONTARIO

JANUARY 2022

© ZHUORAN LI, 2022

ABSTRACT

Positive breaking surge waves are caused by a sudden change in flow. Surge wave front is often associated with high aeration that is linked with a high turbulent behaviour. The 3-dimensional (3D) turbulent structures across a breaking surge are induced by the velocity gradient across the surge and phase discontinuity at the front. Existing experimental studies on this transient phenomenon provide insight into the perturbation measurements, and velocity profiles, in the front and behind the surge wave. However, many experimental measurements only provide pointwise data for this flow of highly transient nature. Furthermore, existing numerical simulations are very limited, where many are mainly 2-dimensional, and a few 3-dimensional (3D) studies have a narrow scope. 3D numerical simulation provides a holistic approach to simulate the turbulent behaviour behind a breaking surge wave. A combination of Volume of Fluid (VOF) method and Large Eddy Simulation (LES) is utilized to capture air entrainment and turbulent structures simultaneously for Froude numbers ranging from 1.71 to 2.49. Computational domain and numerical schemes are designed to model the fully developed surge and parameters precisely. Computational mesh is refined sufficiently to improve the LES quality by resolving at least 90% of the total Turbulent Kinetic Energy (TKE). Using a spanwise periodic boundary, this study ensured the eddies were not compressed by the domain. Air entrainment, TKE and surface perturbations obtained from the present numerical simulations are consistent with laboratory observations reported in the literature. At surge

toe, strong aeration and surface perturbation are observed caused by intense TKE in the area. Velocity perturbations show positive turbulent production in xy -plane rather than yz -plane as the shear instability exists in xy -plane. Finally, the vortices result from shear instability concentrate near the toe in Q-criterion. The vortices start from a 1D structure at the toe and exhibit rod shape upstream in anisotropy maps. This study firstly demonstrated that the computational model is capable of reproducing the key turbulent mechanisms across the surge front and behind the surge. Furthermore, this study highlights the role of instability mechanisms in the formation of a breaking surge wave. Meanwhile, the simulation approaches in the present study contribute to the foundation of future investigation related to positive surge waves and potentially in the fields of aquatic environment and building structure.

ACKNOWLEDGEMENTS

Firstly, I would like to truly appreciate my supervisor, Dr. Shooka Karimpour, who always provided vital advice when I was facing questions and challenges during the research. Your constant guidance and support inspired me and made this thesis possible. Especially during the pandemic, I am very grateful for the extra time Dr. Karimpour has spent to help. In addition, I wish to thank Dr. Rashid Bashir in the supervisor committee, who provided valuable suggestions during my master's study.

Secondly, many thanks to other Dr. Karimpour's research group members: Preet Patel, Arefeh Shamskhany and Akash Venkateshwaran. Thank you for helping me with specific questions with patience.

Finally, I wish to thank my family for their encouragement and support during my research time. Meanwhile, thanks for their understanding and company.

TABLE OF CONTENTS

Abstract.....	ii
Acknowledgements.....	iv
Table of Contents.....	v
List of Tables	viii
List of Figures.....	ix
Chapter 1 Introduction	1
1.1 Background.....	1
1.2 Literature Review.....	5
1.2.1 Experimental Studies	5
1.2.2 Numerical Studies.....	16
1.3 Research Motivation and Objectives	19
1.4 Thesis Structure	22
Chapter 2 Methodology	23
2.1 Governing Equations	23
2.1.1 Turbulent Modelling: Large Eddy Simulation.....	23
2.1.2 LES Governing Equations	25
2.1.3 Sub-grid Scale Models.....	28
2.1.4 Volume of Fluid Method (VOF).....	29

2.2	Numerical Solutions.....	31
2.2.1	Discretization Schemes.....	31
2.2.2	InterFoam Solver and PIMPLE	35
2.3	Numerical Flow Framework.....	36
2.3.1	Surge Wave Froude Number, Fr_s	36
2.3.2	Method of Characteristics (MOC)	38
2.3.3	Computational Domain and Flow Conditions	40
2.3.4	Boundary Conditions	42
2.3.5	Computational Resources	43
Chapter 3 Results and Discussion.....		46
3.1	Phase and Velocity Contours.....	46
3.2	Q-criterion Analysis and Relation to Production.....	54
3.3	Shifting and Ensemble Average.....	62
3.4	Subgrid Scale Resolution.....	64
3.5	Water Depth Perturbations.....	71
3.6	Air Entrainment Profiles and Mixing Cones	78
3.7	Velocity Perturbation and Quadrant Analysis	84
3.8	Turbulence Anisotropy	89
Chapter 4 Summary and Recommendations.....		97
4.1	Summary.....	97

4.2	Recommendations for Future Work.....	99
	Bibliography	100

LIST OF TABLES

Table 1. Flow conditions of the modelled positive surge flows and mesh information. .. 41

Table 2. Computational resources and duration for the simulated cases. 45

LIST OF FIGURES

Figure 1. Photo of a tidal bore with a breaking front. Reprinted with permission from Chanson et al. (2011). Copyright 2011, Elsevier Science & Technology Journals.....	2
Figure 2. Definition sketch of the breaking positive surge wave.	4
Figure 3. Air concentration, α_a at different distance range upstream of the surge front were plotted against vertical distances, h normalized by initial reservoir water depth, d_0 . Reprinted with permission from Chanson (2005). Copyright 2005, Elsevier.	5
Figure 4. Plot of air entrainment, α_a ; x_1 is the distance from gate to jump toe. Reprinted with permission from Murzyn and Chanson (2009). Copyright 2009, Springer Nature BV.	7
Figure 5. Demonstration of velocity measurement with the fixed ADV. Reprinted with permission from Leng and Chanson (2018). Copyright 2018, Elsevier.	8
Figure 6. Change of averaged velocity and its perturbations in streamwise direction with time. Reprinted with permission from Leng and Chanson (2017). Copyright 2017, Elsevier.	9
Figure 7. Water depth median (h_{median}), perturbation ($h_{75} - h_{25}$) from the breaking surge for multiple x measurement positions. Reprinted with permission from Leng and Chanson (2016). Copyright 2016, Springer Nature BV.	11

Figure 8. Maximum water depth perturbations ($(h_{75} - h_{25})_{\max}$, η'_{\max}) vs. Froude numbers for several experimental works where surge wave studies are in blue and hydraulic jump studies are in black. Reprinted with permission from Leng and Chanson (2016). Copyright 2016, Springer Nature BV.	12
Figure 9. Velocity profiles for (a) smooth channel and (b) rough channel with breaking surge, u , v , w are velocities in streamwise, transverse and spanwise directions, respectively. Reprinted with permission from Chanson (2010). Copyright 2010, ASCE.	14
Figure 10. Plot of TKE spectrum vs. wavenumber n . A good LES model should resolve at least 80% or into the shaded zone.	19
Figure 11. Water volume fraction (α_w) example during the interface capture where blue color is under the water and white color is in the air, using VOF.	30
Figure 12. Illustration of the finite volume method nodes for TVD schemes.	34
Figure 13. Analogy method of transferring the transient positive surge waves to quasi-steady state hydraulic jump assuming the observer is moving together with the surge front at a celerity of c . Positive surge waves can be generated with (a) suddenly closure of the gate; (b) opening of the gate, also known as the dam-break wave.	37
Figure 14. Illustration of the MOC for positive surge waves, m is the slope of the characteristics line.	39
Figure 15. Sketch of the computational domain. (a) 3D view of the initial reservoir; (b) front view of the surge wave.	40

Figure 16. Demonstration of subdomains in parallel processing.....	45
Figure 17. Propagating surge wave where α_w is water volume fraction, toward downstream with time, at $t = 4.0, 4.5$ and 5.0 s, for Fr_s of (a) 1.71, (b) 2.13, (c) 2.49. Red line outlines the free surface based on c from MOC. (d) shows initial stage at $Fr_s = 2.49$	51
Figure 18. Plot of the velocity field (u , m/s) variation with time, at $t = 4.0, 4.5$ and 5.0 s, for Fr_s of (a) 1.71, (b) 2.13 and (c) 2.49.	53
Figure 19. Plot of the velocity field relative to theoretical velocity behind the surge (u/U_2), at $t = 4.0, 4.5$, and 5.0 s, for $Fr_s = 2.13$	54
Figure 20. Plots of the instantaneous Q-criterion contour and $Q = 2000$ isosurfaces on the xy-plane at $z = 0.2$ m. The isosurfaces are colored with the resultant velocity. (a) (c) $t = 4.25$ s; (b) (d) $t = 4.50$ s; (e) (g) $t = 4.75$ s; (f) (h) $t = 5.00$ s for $Fr_s = 1.71$	56
Figure 21. Plots of the instantaneous Q-criterion contour and $Q = 2000$ isosurfaces on the xy-plane at $z = 0.2$ m. The isosurfaces are colored with the resultant velocity. (a) (c) $t = 4.25$ s; (b) (d) $t = 4.50$ s; (e) (g) $t = 4.75$ s; (f) (h) $t = 4.93$ s for $Fr_s = 2.13$	57
Figure 22. Plots of the instantaneous Q-criterion contour and $Q = 2000$ isosurfaces on the xy-plane at $z = 0.2$ m. The isosurfaces are colored with the resultant velocity. (a) (c) 4.50 s; (b) (d) $t = 4.75$ s; (e) (g) $t = 5.00$ s; (f) (h) $t = 5.50$ s for $Fr_s = 2.49$	58
Figure 23. Plots of Q-Criterion contour on the yz-plane at $(x - ct)/d_1 = 1.5$ for $Fr_s = 1.71$ at (a) $t = 4.25$ s; (b) $t = 4.50$ s; (c) $t = 4.75$ s; (d) $t = 5.00$ s.	59

Figure 24. Plots of Q-Criterion contour on the yz-plane at $(x - ct)/d_1 = 1.5$ for $Fr_s = 2.13$ at (a) $t = 4.25$ s; (b) $t = 4.50$ s; (c) $t = 4.75$ s; (d) $t = 4.93$ s.	60
Figure 25. Plots of Q-Criterion contour on the yz-plane at $(x - ct)/d_1 = 1.5$ for $Fr_s = 2.49$ at (a) $t = 4.50$ s; (b) $t = 4.75$ s; (c) $t = 5.00$ s; (d) $t = 5.50$ s.	61
Figure 26. Illustration of the weighted algorithm at $t = 4.05$ s for $c = 2.9835$ m/s and uniform grid of $\Delta x = 0.005$ m. The boundaries of the ensemble box are located at $x_1 = 35$ m and $x_2 = 39$ m at $t = 4.00$ s. The weighted factors, W , are calculated based on the vicinity of the shifted domain to the nearest grid point.	63
Figure 27. k_p at Fr_s of (a) 1.71, (b) 2.13 without toe refinement of AR2.	66
Figure 28. Plots of (a) time and z-averaged k_{res} ; (b) k_{SGS} at $t = 4.2$ s and $z = 0.02$ m; (c) time and z-averaged k_p with 80% as the threshold for case#1 with $Fr_s = 1.71$. Water surface is shown as the black line. Yellow box outlines AR2.	68
Figure 29. Plots of (a) time and z-averaged k_{res} ; (b) k_{SGS} at $t = 4.2$ s and $z = 0.02$ m; (c) time and z-averaged k_p with 80% as the threshold for case#2-3 with $Fr_s = 2.13$. Water surface is shown as the black line. Yellow box outlines AR2.	69
Figure 30. Plots of (a) time and z-averaged k_{res} ; (b) k_{SGS} at $t = 4.2$ s and $z = 0.02$ m; (c) time and z-averaged k_p with 80% as the threshold for case#3 with $Fr_s = 2.49$. Water surface is shown as the black line. Yellow box outlines AR2.	70
Figure 31. Plot of L/d_1 against Fr_s , where L is the surge length.	73

Figure 32. Normalized water surface perturbation analysis: (a) time and z-averaged wave surface (blue line), \bar{h} and instantaneous profiles, h ; (b) Squared rms of h' , $h' = h - \bar{h}$; (c) skewness of h , S_h ; (d) Kurtosis of h , K_h for case#1 with $Fr_s = 1.71$ 75

Figure 33. Normalized water surface perturbation analysis: (a) time and z-averaged wave surface (blue line), \bar{h} and instantaneous profiles, h ; (b) Squared rms of h' , $h' = h - \bar{h}$; (c) skewness of h , S_h ; (d) Kurtosis of h , K_h for case#2-3 with $Fr_s = 2.13$ 76

Figure 34. Normalized water surface perturbation analysis: (a) time and z-averaged wave surface (blue line), \bar{h} and instantaneous profiles, h ; (b) Squared rms of h' , $h' = h - \bar{h}$; (c) skewness of h , S_h ; (d) Kurtosis of h , K_h for case#3 with $Fr_s = 2.49$.
..... 77

Figure 35. Normalized wave surface, v_t mixing cone boundary, air mixing cone boundary plots of (a) at $t = 4.0$ s, $z = 0.2$ m; (b) at $t = 4.5$ s, $z = 0.2$ m; (c) time and z-averaged; (d) α_h for case#1 with $Fr_s = 1.71$ 79

Figure 36. Normalized wave surface, v_t mixing cone boundary, air mixing cone boundary plots of (a) at $t = 4.0$ s, $z = 0.2$ m; (b) at $t = 4.5$ s, $z = 0.2$ m; (c) time and z-averaged; (d) α_h for case#2-3 with $Fr_s = 2.13$ 80

Figure 37. Normalized wave surface, v_t mixing cone boundary, air mixing cone boundary plots of (a) at $t = 4.0$ s, $z = 0.2$ m; (b) at $t = 4.5$ s, $z = 0.2$ m; (c) time and z-averaged; (d) α_h for case#3 with $Fr_s = 2.49$ 81

Figure 38. Plots of instantaneous α_a against h/d_2 for $t = 4.25$ s, 4.50 s, 4.75 s, and averaged α_a at $(x-ct)/d_1$ is (a) 1.505; (b) 2.505 and (c) 3.505 for $Fr_s = 2.13$.

..... 84

Figure 39. Velocity perturbation plots normalized by U_2 . (a) and (c) are u'/U_2 vs. v'/U_2 ; (b) and (d) are v'/U_2 vs. w'/U_2 at $y = d_1$ and $= d_1 + 0.5(d_2 - d_1)$, respectively.

Column (1) is for case#2-1; column (2) for case#2-2 and column (3) for case#2-3. 87

Figure 40. Velocity perturbation plots normalized by U_2 . (a) and (c) are u'/U_2 vs. v'/U_2 ; (b) and (d) are v'/U_2 vs. w'/U_2 at $y = d_1$ and $= d_1 + 0.5(d_2 - d_1)$, respectively. Column (1) is for case#1; column (2) for case#2-3 and column (3) for case#3.

..... 88

Figure 41. Lumley triangle (upper) and barycentric map (lower) of surge front turbulence at $Fr_s = 1.71$. Blue dots are given at $h/d_2 = 0.520$ at the toe, orange points are given at $h/d_2 = 0.638$ at a quarter of surge, grey points are given at $h/d_2 = 0.755$ at half of surge and yellow points are given at $h/d_2 = 0.872$ at three quarters of surge. 93

Figure 42. Lumley triangle (upper) and barycentric map (lower) of surge front turbulence at $Fr_s = 2.13$. Blue dots are given at $h/d_2 = 0.410$ at the toe, orange points are given at $h/d_2 = 0.546$ at a quarter of surge, grey points are given at $h/d_2 = 0.682$ at half of surge and yellow points are given at $h/d_2 = 0.819$ at three quarters of surge.

..... 94

Figure 43. Lumley triangle (upper) and barycentric map (lower) of surge front turbulence at $Fr_s = 2.49$. Blue dots are given at $h/d_2 = 0.325$ at the toe, orange points are given at $h/d_2 = 0.456$ at a quarter of surge, grey points are given at $h/d_2 = 0.607$ at half of surge and yellow points are given at $h/d_2 = 0.738$ at three quarters of surge. 95

Chapter 1

Introduction

1.1 Background

Surge waves are transient open channel flows that form due to an abrupt change in flow depth or velocity. Surge waves appear in man-made hydraulic conveyance structures and natural systems. Tsunami waves, for instance, are generated by the displacement of water caused by landslides, volcanic activities, or earthquakes (Xie and Chu, 2019). Breach in dams can lead to the release of massive amount of reservoir water and lead to the formation of dam break waves which is another example of a surge wave. Both phenomena lead to destruction and adversely impact both built and natural environments. For example, the Tohoku Earthquake led to a Tsunami that removed 30.3% of buildings near the ocean. Also, another 17.3% of buildings fell, as mentioned by Xie and Chu (2019). For the dam break, Buffalo Creek Valley dam failure in the US, 1972, caused by poor dam construction, led to 125 deaths (ASDSO, 2020). Natural factors, including intense rainstorms accompanying spillway blockage, will lead to overtopping as the most common reason behind dam failure in the last ten years (ASDSO, 2020). Destruction of the dam by an earthquake can also cause dam failure. The tidal bore is also a well-known example of surge waves. It forms when the low depth river coincides with the ocean at the estuary and the river is forced back with a positive surge wave generated (NGS, 2012). Flooding is the main issue to the community adjacent to the river and fulfills the condition to generate tidal bore (Mubarak et al., 2017). Therefore, it is vital to understand the surge wave from different perspectives,

such as its dynamic properties, transport ability, and wave forces to reduce the damage caused by such extreme events to public health and property. In man-made canals, surge waves are often initiated by the gate closure downstream (Chanson, 2004).



Figure 1. Photo of a tidal bore with a breaking front. Reprinted with permission from Chanson et al. (2011). Copyright 2011, Elsevier Science & Technology Journals.

A highly turbulent wave front is one of the most important features of the positive surge waves, which contributes to air entrainment, sediment gathering, and induces contaminant and debris transport (Li and Chanson, 2018). In addition, turbulent structures under the front of the tidal bore may lead to bed erosion (Chanson and Tan, 2010). Bed erosion results in river channel expansion, adverse effects on water safety and habitat environment, and jeopardizes bridges over the river (Department of Environment and Resource Management of Queensland, 2009). Like tidal bores, the dam break waves cause sediment movement and channel bed erosion and can cause swift changes in the bed formation across the channel downstream. Consequently, the flow will be altered, and the

estimation of factors such as peak water depth and time to reach the residence area for alert purposes will become difficult (Zech et al., 2008). Therefore, understanding the turbulent characteristics of the surge wave will contribute to environmental and water resources management in aquatic systems.

Figure 2 is a definition sketch of the positive surge wave, where the red dots indicate the locations of “surge toe” and “surge heel”, and the horizontal distance between two points is known as the “surge length”. U_1 is the downstream flow velocity, U_2 is the flow velocity behind the surge, d_1 is the downstream water depth, d_2 is the water elevation of surge from the channel bed and c is the celerity or speed of the surge wave front. There are generally two types of surge waves: undular wave with a smooth surface and little aeration compared with the breaking wave with a significant amount of air entrainment. They can be categorized by the surge wave Froude number:

$$Fr_s = \frac{c - U_1}{\sqrt{gd_1}} \quad Eq. 1$$

As reported by literature such as Leng and Chanson (2017) and Zheng et al. (2018), breaking surge was observed in the range of $Fr_s > 1.5$, whereas undular surge waves are observed at Froude numbers below this threshold.

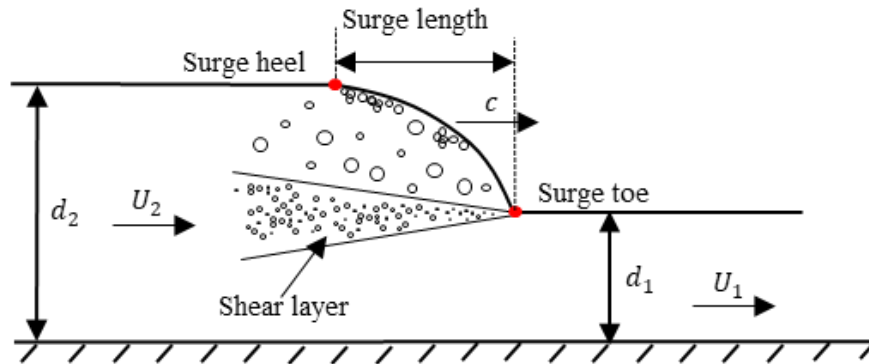


Figure 2. Definition sketch of the breaking positive surge wave.

The turbulence and air entrainment characteristics (shown in Figure 2) are caused by the discontinuity in water depth and velocity, which is pronounced across the wave front. A similar structure is also observed across hydraulic jumps. Hydraulic jumps and surge waves have been historically known to be analogous to shock waves in compressible flow (Gilmore et al., 1950) as both categories are compression waves of finite amplitude.

Chaos and disorder are the nature of a turbulent flow and are also observed across breaking surge waves. The source of instability includes the breaking surge front and the area of shear layer as shown in Figure 2. Meanwhile, the air entrainment near the surge front varies rapidly, along with the surface profile and turbulent properties. In addition, there are concentrated small-scale perturbations to capture. Since then, all these properties have made studying the subject using numerical or experimental methods complex. Below are reviews of some existing works in surge waves and hydraulic jump conducted using experimental or computational methods outlined in the literature. The aim is to identify the

knowledge gap and signify the importance of the research conducted in the scope of this thesis.

1.2 Literature Review

1.2.1 Experimental Studies

1.2.1.1 Surge Wave Aeration

Chanson (2005) presented a surge wave experimental study focusing on air entrainment patterns. The results showed intense air entrainment near the surge front. Chanson (2005) used “single-tip conductivity probes” in the middle of the flume span.

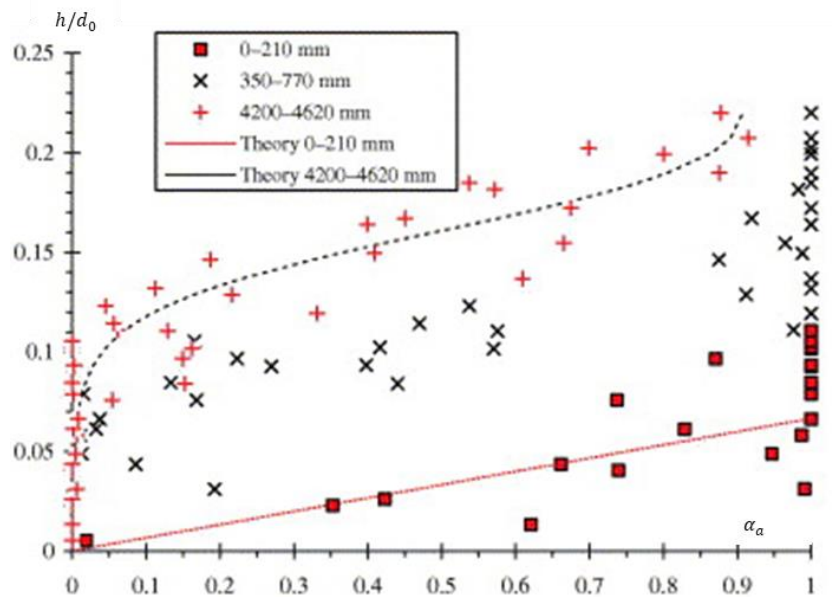


Figure 3. Air concentration, α_a at different distance range upstream of the surge front were plotted against vertical distances, h normalized by initial reservoir water depth, d_0 .

Reprinted with permission from Chanson (2005). Copyright 2005, Elsevier.

The air concentration α_a profile in Figure 3 shows that measurement within the different range of distance in streamwise direction relative to the surge front (0 mm), such as 4200-4620 mm has smaller air entrainment compared to the point near surge front at the same h/d_0 . A useful theoretical relation was developed by Chanson and Toombes (2002), shown in Figure 3, which is plotted from $\frac{h}{d_0} = 0$:

Near surge front

$$\alpha_a = 0.9 * \frac{h}{H_{90}} \quad \text{Eq. 2}$$

Near surge behind

$$\alpha_a = 1 - \tanh^2 \left(K' - \frac{h}{2D_0} + \frac{\left(\frac{h}{H_{90}} - \frac{1}{3}\right)^3}{3D_0} \right) \quad \text{Eq. 3}$$

where α_a is the air concentration, H_{90} is the height at air concentration of 0.9, K' and D_0 is solely based on average aeration. By comparing in Figure 3, the theoretical equations can predict the air concentration with reasonable accuracy.

Air entrainment was well studied in hydraulic jump, for instance, by Murzyn and Chanson (2015). With the conductivity sensor, air concentration was recorded, which was plotted with y -direction in Figure 4. From Figure 4, the shear layer and recirculation region can be identified. Although the paper experimented with hydraulic jumps, it is applicable to surge waves as they share the exact nature.

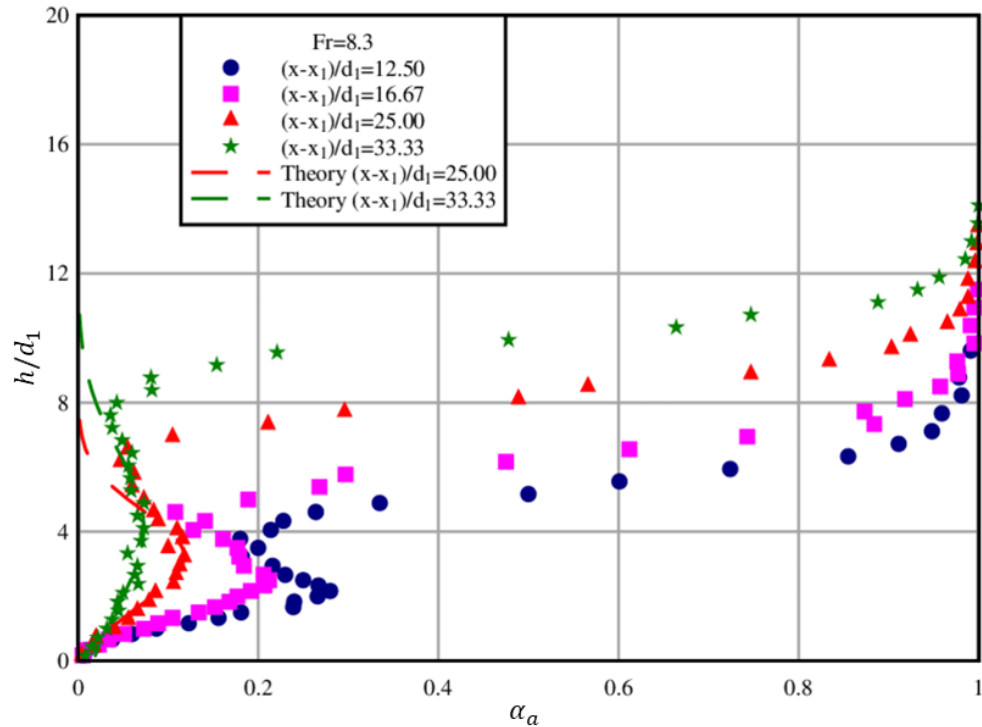


Figure 4. Plot of air entrainment, α_a ; x_1 is the distance from gate to jump toe. Reprinted with permission from Murzyn and Chanson (2009). Copyright 2009, Springer Nature BV.

Blenkinsopp and Chaplin (2011) investigated aeration characteristics within different compositions of water. As a result, the density of small air bubbles was higher for seawater, but the overall air concentration and variation with respect to time and space were close among different fluids.

1.2.1.2 Turbulent Characteristics

Koch and Chanson (2009) reported the surge wave turbulence by obtaining velocity with Acoustic Doppler Velocimeter (ADV) and corresponding Reynolds stresses. As shown in Figure 5, the ADV started collecting velocity data as the surge wave passed. This pointwise

measurement was then used to calculate and plot velocity perturbation and Reynolds stresses. Align with the depth data from the fixed displacement probe, figures like Figure 6 can be plotted with respect to time. Thus, a sudden rise in the water depth profile represented the arrival of the surge wave.



Figure 5. Demonstration of velocity measurement with the fixed ADV. Reprinted with permission from Leng and Chanson (2018). Copyright 2018, Elsevier.

For the breaking surge wave, Leng and Chanson (2017) point measurements showed a sharp drop of x -direction velocity as surge moved by. Another significant observation in the work of Koch and Chanson (2009) was the shortly change of direction for velocity in x -direction for the area under the surge due to “flow separation”, which was also reported by Gualtieri & Chanson (2011) for a momentary period. For the Reynolds stresses, a sharp jump was observed with the surge arrival, which can be associated with the mixing cone; however, for the dominant area of the mixing cone which was the upper surge, its turbulent characteristics were not measured in this paper.

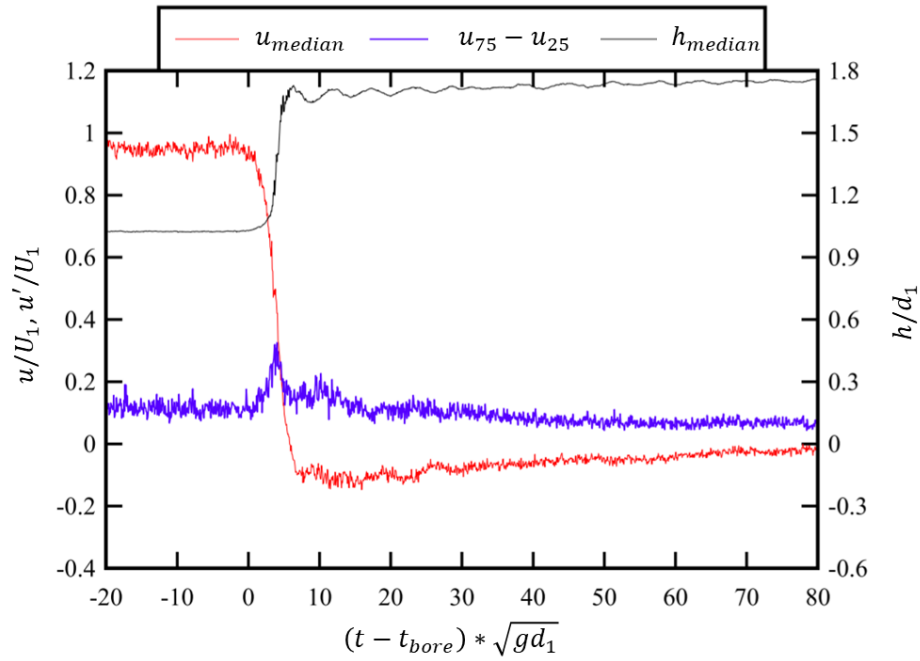


Figure 6. Change of averaged velocity and its perturbations in streamwise direction with time. Reprinted with permission from Leng and Chanson (2017). Copyright 2017, Elsevier.

The surface profiles are usually analyzed together with the turbulent properties. The outward bending shape is typical to observe for the surge front free surface, as reported by both Koch and Chanson (2009) and Gualtieri and Chanson (2011).

Leng and Chanson (2016) also investigated the turbulent structures of positive surge waves along with the water depth perturbation. In their study, both displacement meters and velocimeter were adapted to capture the velocity and water depth, respectively. The experiment was proceeded in a repeated manner and used ensemble average for result presentation. The water depth perturbation equalled to $h_{75} - h_{25}$, which was the third

quartiles minus the first quartiles of water depth. Each experiment was performed 25 times. The corresponding third quartiles and first quartiles were determined and used to define the water depth perturbations.

Here, Figure 7 shows the instantaneous water depth and corresponding perturbations, also from the breaking surge. From Figure 7, Leng and Chanson (2016) noticed a peak of water depth perturbation when the surge arrived. The paper also summarized other works with itself for the relation between Froude number and maximum water depth perturbations. The empirical equation derived based on the data points described maximum water depth perturbations increased with Froude number was a general trend for surge wave and hydraulic jump as shown in Figure 8. The paper also reported the Reynolds stresses changed with time and observed a time lag between the moment that surge reaches the probe and peak normal Reynold stresses. Similar patterns were also observed in Koch and Chanson (2009).

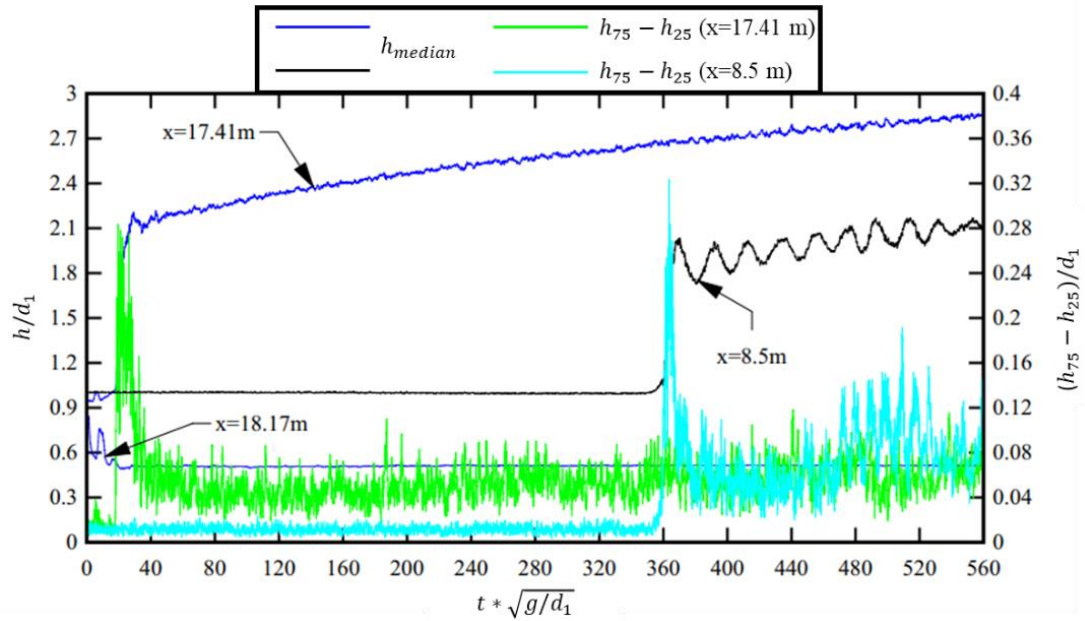


Figure 7. Water depth median (h_{median}), perturbation ($h_{75} - h_{25}$) from the breaking surge for multiple x measurement positions. Reprinted with permission from Leng and Chanson (2016). Copyright 2016, Springer Nature BV.

1.2.1.3 Instability Mechanisms

The air entrainment as a result of instability at the surge breaking front was modelled physically by Wang et al. (2017). They have observed and indicated the three most common mechanisms that were possible to induce instability (air entrainment) for hydraulic jump and breaking surge. The first mechanism was caused by the encounter of moving surge with downstream flow. The downstream flow can have a velocity at the opposite direction of the moving surge or have no velocity. Initially, there was a layer of air above the downstream free surface. Therefore, the air layer moved into propagating surge led to the formation of air cavity near the surge toe.

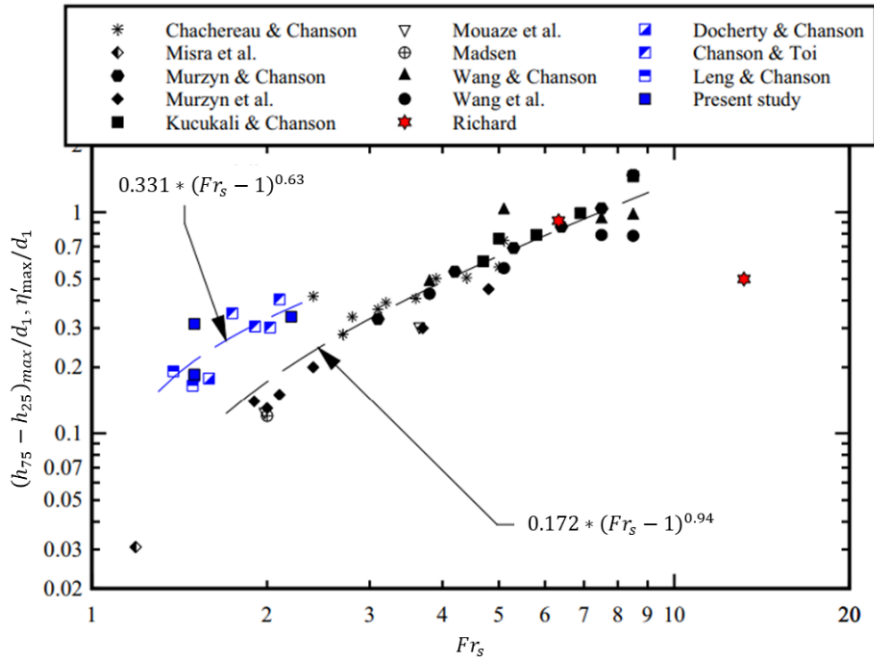


Figure 8. Maximum water depth perturbations $((h_{75} - h_{25})_{max} , \eta'_{max})$ vs. Froude numbers for several experimental works where surge wave studies are in blue and hydraulic jump studies are in black. Reprinted with permission from Leng and Chanson (2016). Copyright 2016, Springer Nature BV.

The air cavity will be broken into small air bubbles by shear stress and water nearby. The bubbles will breakup after float to the free surface. The second mechanism was caused by plunging wave and trapped air within the surge wave. The third mechanism was due to the breaking of wave in the air. It was related to strong turbulence with massive vortices caused by Kelvin-Helmholtz shear instability. It led to air entrainment near the air-water interface and surge toe as well. In sum, most of the instability in the surge wave is firstly caused by shear effect at the surge toe when the moving surge slides over the downstream

flow. It generates TKE and divides the large bubbles into small bubbles. Secondly, with two different phases, the splashing wave due to Kelvin-Helmholtz shear instability is another source of turbulence.

The existence of shear layer that starts from the instability at the surge toe is reported by several works of literature. Wang and Chanson (2015) conducted experimental works and maximum air entrainment (α_a) was identified within the shear layer of a hydraulic jump. Chanson (2007) identified that the toe was the entrance of air bubbles and reached the shear layer, exhibiting strong turbulent behaviour. Kucukali and Chanson (2008) also reported the shear layer based on the α_a profile and measured intense turbulence within the shear region.

1.2.1.4 Roughness of Channel

The affect of channel friction on positive surge wave was also well investigated. Such as Chanson (2010), compared the undular and breaking surge with either smooth or rough channel. The velocity comparison in x -direction exhibited a frequent reversal of x velocity behind the surge front, also known as “transient recirculation”. The region of transient recirculation in the case with rough channel was extended compared to the smooth channel. It was shown that with an increase of channel friction, the transient recirculation also increases, as shown in Figure 9.

Besides the whole application of a rough surface on the bed, the affect from an object with a rough surface on the channel was studied by Yeow et al. (2016). For the case

with the object, the transient recirculation also lasted longer. It means the region was farther extended compared with the case without the object.

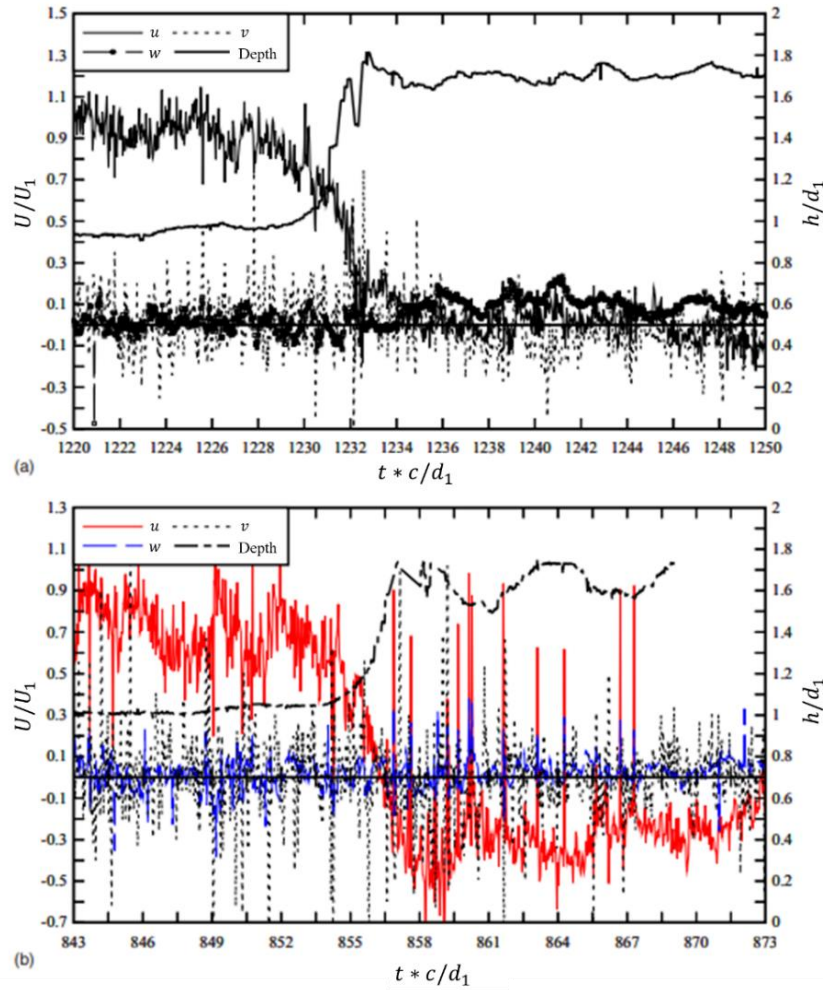


Figure 9. Velocity profiles for (a) smooth channel and (b) rough channel with breaking surge, u , v , w are velocities in streamwise, transverse and spanwise directions, respectively. Reprinted with permission from Chanson (2010). Copyright 2010, ASCE.

Similarly, the exhibition of transient recirculation was represented by the enhanced velocity perturbation. According to Yeow et al. (2016), it was 60% greater with the object.

Therefore, by increasing the roughness of bed, either at a fixed location or through the whole bed, the velocity perturbation will be sharper and more obvious compared with a smooth bed.

To summarize the experimental studies that have been reviewed in this chapter, and other similar experimental studies such as Murzyn and Chanson (2009), Toi and Chanson (2013) and Frazao and Zech (2002), these studies either focused on the aeration property or turbulent structure such as velocity measurements and Reynolds stresses. However, the interconnection between two characteristics of positive surge waves is overlooked. Therefore, part of the research will investigate the turbulent structure and air entrainment patterns together with the numerical method. Besides, the experimental studies introduced above performed measurements that were point based, which means a fixed location probe will collect data such as water depth, velocity as the wave passes by. Such time series results were plotted, for example, in Figure 6. Patterns can be found from this type of setup but the numerical simulation can provide a more direct view. The numerical results give access to not only the velocity field, air entrainment field but also other turbulent characteristics such as eddy viscosity, Q-criterion and so on. Meanwhile, it's more convenient to obtain the domain averaged data compared to experimental method, especially with respect to the spanwise direction. The following section will discuss the numerical studies about the positive surge waves.

1.2.2 Numerical Studies

1.2.2.1 Two Dimensional (2D) and Three Dimensional (3D) Numerical Simulations

Leng et al. (2018) compared the 2D simulation results with available laboratory results for the water depth, velocity in streamwise and perpendicular directions. The difference is evident by comparing velocity and water depth profiles between laboratory results and 2D simulations. For example, the numerical u behind surge was larger in terms of magnitude and fluctuation compared with experimental u . Moreover, the information about flow characteristics in the third dimension remained unknown.

Lubin et al. (2010) performed numerical simulation also on a 2D domain, as one of the earliest groups modelled the surge waves. Although the overall shape of the 2D water depth profile and position of the air entrainment exhibited similarity to the experimental phenomenon, the 2D numerical results did not reflect the physical free surface and air entrainment patterns accurately, especially near the turbulent surge front. The 3D nature of fully cascading turbulent flow has been overlooked in these studies.

On the other hand, Lubin and Glockner (2015) were one of the few papers that incorporated 3D nature into the surge waves modelling. Watanabe et al. (2005) also conducted 3D simulations of plunging wave and presented the undular shape vortex in spanwise direction. Thus, the 3D modelling provides the opportunity for a comprehensive understanding of the turbulent structure of the surge wave, and it is closer to the realistic surge behaviour. However, these existing 3D numerical simulations mainly focus on one feature of the surge wave, for instance, on the plunging jet at the surge front. Furthermore,

as outlined by Lubin and Glockner (2015), the 3D turbulent process is quite critical to capture. This requires proper set-up of the spanwise domain, as outlined in the coming subsection. Therefore, to capture the behaviour of flow, in the vicinity of toe, at the surge front, and behind the surge, 3D simulations are necessary. Further discussion on the set-up of 3D simulations will be discussed in the coming sections of Chapter 1 and Chapter 2.

1.2.2.2 Spanwise Simulation and Periodic Boundary Condition

It is important to perform 3D simulation rather than 2D simulation which has been indicated by various literature in the past, especially for the study of turbulent structure in a breaking wave. As noted by Lubin and Glockner (2015), for breaking waves, the initial 2D turbulent eddies transformed to 3D structure along flow direction, due to the shear effect, which led to fluctuation. Also, they have mentioned the existence of 3D “obliquely descending eddies” near upstream of a breaking surge. Therefore, to capture the full dimension of the 3D turbulent structure, it is vital to perform a 3D simulation for the breaking wave. In order to incorporate the simulation in the spanwise dimension, the boundary condition for the front and back faces are typically set to periodic boundary condition, which has the perturbations are fed back into the domain. It is adapted mainly to reduce the size of domain and save computational time. For the case of preparing fully-developed inlet flow, spanwise periodic boundary conditions can recirculate the flow to reach the final state without involving a large domain size. The dimension between two periodic boundaries plays an important role when designing and applying the periodic boundary condition. The periodic boundaries should not generate any affect on the flow,

especially to the turbulent structure, that are physical. Therefore, the dimension between two periodic boundaries needs to accommodate the largest scale of eddies (Munters et al., 2016).

Periodic boundary condition also has a broad application across different fields of study in CFD. Including gas and solid phase modelling (Kuang et al., 2013), contaminant transportation (Labovský, 2011), heat exchange (Barletta et al., 2009), open-channel flow (Bradbrook et al., 2000).

1.2.2.3 LES Quality and Grid Resolution

Large Eddy Simulation (LES) is one of the three turbulent models available, the other two are Direct Numerical Simulation (DNS), and Reynolds Averaged Navier-Stokes equations (RANS). RANS will resolve only the averaged portion of the turbulent flow and model the perturbation portion in the flow. DNS will resolve every scale in the flow from integral to Kolmogorov's scale. LES will resolve the scale greater than the filter size and model the smaller scale. Then the computational effort required and simulation accuracy follow as $DNS > LES > RANS$. Therefore, LES is a popular approach since it doesn't require an extreme amount of computational resources as DNS but can resolve larger than scale turbulent motion. Since surge wave dynamics are tightly connected to turbulent flow at the surge front, LES is preferred over RANS to present sufficient turbulent characteristics. To achieve a high quality LES simulation, the grid size needs to be sufficiently small which is capable to resolve the majority of total TKE. A widely accepted standard is to resolve at least 80% of total TKE. The 80% threshold is determined based on analytical methods in

Pope (2001). Matheou and Chung (2014) have conducted convergence studies for the larger than filter turbulent scales and have concluded that a 90% resolved rate can satisfy a convergence threshold instead of the 80% originally proposed by Pope (2001). As further discussed by Matheou and Chung (2014), the variation of domain structure during the convergence test did not affect the 90% result significantly. Meanwhile, they have suggested the 90% can be applied to different models under LES to achieve convergence.

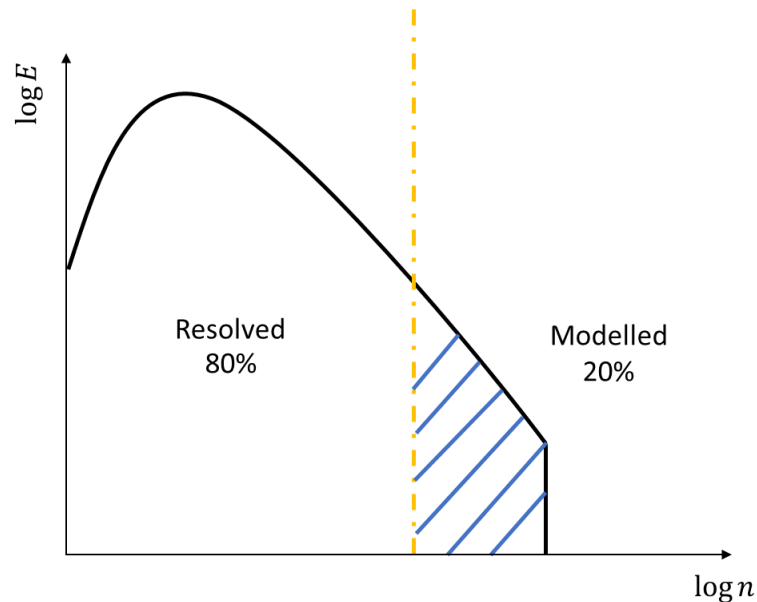


Figure 10. Plot of TKE spectrum vs. wavenumber n . A good LES model should resolve at least 80% or into the shaded zone.

1.3 Research Motivation and Objectives

The research focuses on the numerical investigation of breaking positive surge waves on their turbulent structure and air entrainment patterns. The surge wave is produced by simulating a sudden lift of the gate, which is often used to generate surge waves

numerically and experimentally (see e.g., Liu et al., 2017). As indicated in the literature review, most of the studies either studied the turbulent property or the aeration patterns. The thesis aims to correlate two aspects of breaking surge waves of Froude numbers higher than 1.6. The turbulent structures across the mixing layer and breaking surge are initiated due to two instability mechanisms: velocity gradient in depth and pressure gradient in the streamwise direction. Although some of the structures are induced and initiated as two-dimensional, in time they evolve into 3D structures (Watanabe et al., 2005; Lubin and Glockner, 2015). Several numerical studies have investigated the turbulent structures and Reynolds stresses across breaking and undular surge waves. Many of these studies, however, have overlooked the 3D nature of the fully cascading turbulent flow across a breaking wave (e.g., Leng et al., 2018). Despite their intricate nature, only a few numerical studies investigated the 3D nature of rolling, breaking, and energy cascade in surge waves (Kimmoun and Branger, 2007; Lubin and Glockner, 2015). Therefore, the thesis explicitly targets the 3D development of turbulent breaking surge waves using a robust and accurate LES model. Due to the 3D nature of fully cascading eddies at the surge front, it is critical to capture the turbulent spanwise perturbations. Capturing this dimension requires delicate consideration for the spanwise scale of eddies. The extent of the spanwise boundary condition has a significant effect on the suppression of large-scale eddies, and it has to be selected to accommodate the largest scales (Munters et al., 2016). Therefore, here great emphasis is focused on the spanwise extension of the periodic domain. Furthermore, most existing 3D numerical studies use Large Eddy Simulation (LES). The performance of LES,

however, significantly depends on grid resolution and filter size (Pope, 2001). Considerations for the impact of spanwise boundary and LES filter resolution are often overlooked in many existing 3D studies on breaking surge waves (Watanabe et al., 2005; Chanson et al., 2012). Thus, the thesis also aims to improve the quality of simulation by improving the implementation of the LES while incorporating spanwise periodic boundary, allowing the full development of 3D structures noted in the literature.

In sum, the objectives are:

- Study the interconnection between turbulent characteristics and air entrainment patterns, such as perturbations, turbulent kinetic energy, and vortices in positive breaking surge waves, especially near the locations of instability mechanisms.
- Comparing several analyses between different surge Froude numbers, Fr_s , in order to identify the trend associated with Fr_s .
- Perform fully 3D numerical simulations of surge waves to conduct the comprehensive studies of the surge waves.
- Delicate consideration about spanwise dimension between periodic boundary conditions, which will not limit the growth of turbulence in the dimension and highlights its role within the surge waves.
- Improve the quality of Large Eddy Simulation (LES) by reaching a minimum turbulent kinetic energy resolving rate of 80% with proper mesh refinement, which will increase the resolution of simulation as well.

1.4 Thesis Structure

- **Chapter 1** introduces the breaking surge waves and relative approaches of studies, followed by the literature review related to the study of positive surge waves comprehensively. Two aspects of the studies are covered: Section 1.2.1 includes the example works of experimental studies, and Section 1.2.2 includes the example works of numerical studies, which is followed by the research objectives of the thesis.
- **Chapter 2** is the methodology chapter which describes the governing equation for the turbulent modelling and two-phase flow modelling, numerical solutions related to the surge wave simulation in OpenFOAM, surge wave Froude number definition, 1D Method of Characteristics (MOC), and computation domain, boundary conditions. Lastly, the discussion about computational time, capacity, and resources.
- **Chapter 3** is the result and discussion chapter, which starts with the overview of a positive surge wave from the simulation, including phase and velocities. Then the Turbulent Kinetic Energy (TKE) analysis regards the critical mesh resolution, water depth perturbations, turbulent mixing relation with the air entrainment patterns, domain width determination in the 3D simulation with periodic boundary conditions, turbulence production and vortex properties and turbulence anisotropy.
- **Chapter 4** concludes this thesis and discusses possible gaps and future research.

Chapter 2

Methodology

2.1 Governing Equations

2.1.1 Turbulent Modelling: Large Eddy Simulation

As computer technology has developed rapidly in the past 20 years, Computational Fluid Dynamics (CFD) has become a fundamental approach in simulating and designing fluid mechanics challenges. It surpasses the original analytical fluid dynamics with a high level of complexity in terms of geometry and flows conditions (Vold, 2017). Compared with experimental fluid dynamics, CFD is more economical to save the financial and time expense of building the physical model. For specific large-scale models and flow parameters challenging to measure, CFD is an excellent choice as well (Karimpour, 2019). The CFD tool used is called “Open-source Field Operation and Manipulation” (OpenFOAM), which is an open-source CFD tool developed based on C++ language (Greenshields, 2019). Every OpenFOAM case has three necessary folders where users can set up numerical modelling inputs instead of using the graphical user interface (GUI). With numerous solvers designed for different study fields and flow conditions such as steady/unsteady, turbulent/laminar, compressible/incompressible, the user needs to choose the appropriate solver.

Moreover, OpenFOAM solvers range from fluid problems to areas including stress studies, electromagnetics, etc (OpenCFD, n.d.). As open-source software, any modifications in the source code are possible. Nevertheless, it is critical to select the

appropriate solver for the simulations. Simulation results are stored in a series of time folders in OpenFOAM. The software named “ParaView” is usually adapted jointly with OpenFOAM to view the simulation results and perform post-processing.

For a sudden release of millions of cubic meters of water in a reservoir, the wave generated is expected to be turbulent flow, and most of the fluid flow observed in life belongs to turbulent flow rather than laminar flow where the layers are parallel and smooth. Turbulent flow has the properties of irregular turbulence and chaotic flow. For instance, Reynolds number exceeds 4000 for pipe transportation (Menon, 2014). As a result, the turbulent model should reflect the complicated structure, especially the small-scale turbulent fluctuation in the flow. Based on a different scale of eddies, there are three approaches: Direct Numerical Simulation (DNS) approach from original Navier-Stokes equations, Large Eddy Simulation (LES), and Reynolds Averaged Navier-Stokes equations (RANS) modelling methods. DNS can resolve every scale in the turbulence, as well as the mesh size and time steps need to be decreased significantly to resolve the smallest time and length scales. These limitations make DNS the most computationally expensive method among the three due to the high computational frequency and amount of meshes in each calculation; LES with a spatial filter will solve the eddies greater than the grid scale with the LES governing equation. Meanwhile, the tolerance on mesh size and time steps is higher compared with DNS since the small-scale turbulent motion can be calculated based on sub-grid scale models. Here the turbulence with a greater size above the filter dominates the energy movement that is highly related to the hydraulic conditions. On the other hand,

the existence of eddies that are below the filter is widespread and controlled by viscosity (J. C. Bennetsen, 2000). The RANS models can only resolve the time-averaged part of the turbulent structure and modelled the perturbation part of the flow as there will always be more unknowns in Reynold stress terms than equations available, so it has a closure problem which can be solved by additional terms in many RANS turbulence modelling methods (ANSYS, 2010). For this thesis, LES is selected as it can present more detailed eddies than RANS, and it is not as computation demanding as DNS. From a broader perspective, LES has the benefits of providing the modelling data of eddies specifically, in terms of its transient behaviour and 3-D spatial variation. These data of eddies will not be obvious to capture from the previous turbulent models, including RANS. In comparison with the statistical model, LES can exhibit the development of turbulence along with time (J. C. Bennetsen, 2000).

2.1.2 *LES Governing Equations*

LES governing equation is derived by filtering the Navier-Stokes equations:

$$\frac{\partial \rho}{\partial t} + \frac{\partial(\rho u_i)}{\partial x_i} = 0 \quad \text{Eq. 4}$$

$$\frac{\partial(\rho u_i)}{\partial t} + \frac{\partial(\rho u_i u_j)}{\partial x_j} = -\frac{\partial p}{\partial x_i} + \mu \frac{\partial^2 u_i}{\partial x_j^2} \quad \text{Eq. 5}$$

where Equation 4 represents the conservation of mass and Equation 5 represents the conservation of momentum within the control volume. Here, u is the flow velocity, x indicates the locations and t indicates the time, ρ is the constant density of the fluids, p is

the pressure and μ is the dynamic viscosity; Equations 4 and 5 are presented in the suffix notation and i or $j = 1$ in this notation corresponds to the x -direction, i or $j = 2$ corresponds to the y -direction, and i or $j = 3$ to the z -direction.

The different terms in the Navier-Stokes equations respectively represent: $\frac{\partial(\rho u_i)}{\partial t}$ for velocity's rate of variation with respect to time, $\frac{\partial(\rho u_i u_j)}{x_j}$ represents the convection term when it is related to the fluids' transportation or advection terms when it is related to the other variables such as the volume fraction, kinetic energy within the flow; $\frac{\partial p}{\partial x_i}$ is the pressure gradient term; and $\mu \frac{\partial^2 u_i}{\partial x_j^2}$ stands for the molecular diffusion in the flow.

In LES, to filter any parameter, ϕ , it is decomposed into two parts, one is above the grid scale which will be solved with the LES governing equation: $\bar{\phi}$; the second part is below the grid scale or as known as the sub-grid scale (SGS), which will be modelled with numerical models associated with the LES: ϕ' . The reason that filter size (Δ) is determined as the mesh size is based on the following equation:

$$\Delta = (V_{cell})^{\frac{1}{3}} \quad Eq. 6$$

where V_{cell} is the cell volume. Since the meshes are cube, the filter size equals the grid length in any direction. As a result:

$$\phi = \bar{\phi} + \phi' \quad Eq. 7$$

Similarly, for the velocity, u and pressure, p :

$$u = \bar{u} + u' \quad \text{Eq. 8}$$

$$p = \bar{p} + p' \quad \text{Eq. 9}$$

Starting with the continuity equation, the first assumption made is the filter being homogeneous which means the “filter and derivative commute”, therefore:

$$\frac{\partial \rho}{\partial t} + \overline{\left(\frac{\partial \rho u_i}{\partial x_i} \right)} = \frac{\partial \rho}{\partial t} + \frac{\partial (\rho \bar{u}_i)}{\partial x_i} = 0 \quad \text{Eq. 10}$$

Similarly for the momentum equation:

$$\overline{\frac{\partial \rho u_i}{\partial t}} + \overline{\frac{\partial \rho u_i u_j}{\partial x_j}} = -\frac{\partial \bar{p}}{\partial x_i} + \mu \overline{\frac{\partial^2 u_i}{\partial x_j^2}} \quad \text{Eq. 11}$$

Same as:

$$\frac{\partial (\rho \bar{u}_i)}{\partial t} + \overline{\frac{\partial \rho u_i u_j}{\partial x_j}} = -\frac{\partial \bar{p}}{\partial x_i} + \mu \frac{\partial^2 \bar{u}_i}{\partial x_j^2} \quad \text{Eq. 12}$$

To solve $\overline{\frac{\partial \rho u_i u_j}{\partial x_j}}$, u_i is an unknown. On the other hand, \bar{u}_i can be used as the substitution to

solve the equation instead, therefore Equation 12 becomes:

$$\frac{\partial (\rho \bar{u}_i)}{\partial t} + \frac{\partial (\rho \bar{u}_i \bar{u}_j)}{\partial x_j} = -\frac{\partial \bar{p}}{\partial x_i} + \mu \frac{\partial^2 \bar{u}_i}{\partial x_j^2} - \left(\overline{\frac{\partial \rho u_i u_j}{\partial x_j}} - \frac{\partial (\rho \bar{u}_i \bar{u}_j)}{\partial x_j} \right) \quad \text{Eq. 13}$$

The last term in Equation 13 can also be written with the sub-grid scale turbulent shear stress, τ_{ij}^{SGS} :

$$\tau_{ij}^{SGS} = \rho (\overline{u_i u_j} - \bar{u}_i \bar{u}_j) \quad \text{Eq. 14}$$

And Equation 13 becomes:

$$\frac{\partial(\rho\bar{u}_i)}{\partial t} + \frac{\partial(\rho\bar{u}_i\bar{u}_j)}{\partial x_j} = -\frac{\partial\bar{p}}{\partial x_i} + \mu\frac{\partial^2\bar{u}_i}{\partial x_j^2} - \frac{\partial\tau_{ij}^{SGS}}{\partial x_j} \quad Eq. 15$$

which is the final momentum equation for LES.

2.1.3 Sub-grid Scale Models

The SGS turbulent shear stress term in Equation 15 needs to be modelled, also known as the SGS models. The models will target the movement of eddies that are not resolved within the pre-defined mesh during the simulation process. Compared to the eddies with greater sizes, the SGS eddies are further homogeneous and sensitive to the physical fluctuation, which allows the potential of models to anticipate extra details of the flow in addition to the portion above the filter size. Generally, the SGS models mainly will represent eddy viscosity, μ_t differently and with the strain rate, \bar{S}_{ij} , as a function of greater than filter size eddies, τ_{ij}^{SGS} will be computed (J. C. Bennetsen, 2000).

The SGS model applied for the project is the k-equation model, initially proposed by Yoshizawa and Horiuti (1985). Firstly, the turbulent shear stress is defined by the SGS turbulence model:

$$\tau_{ij}^{SGS} = -2\mu_t\bar{S}_{ij} + \frac{1}{3}\tau_{ii}^{SGS}\delta_{ij} \quad Eq. 16$$

where δ_{ij} is the Kronecker delta and \bar{S}_{ij} is the strain rate, defined as:

$$\bar{S}_{ij} = \frac{1}{2}\left(\frac{\partial\bar{u}_i}{\partial x_j} + \frac{\partial\bar{u}_j}{\partial x_i}\right) \quad Eq. 17$$

The eddy viscosity of the SGS motion is constructed based on the k-equation model (Yoshizawa and Horiuti, 1985):

$$\mu_t = \rho C_k \Delta \sqrt{k_{SGS}} \quad Eq. 18$$

where $C_k = 0.094$ in the model, k_{SGS} is the turbulent kinetic energy in the sub-grid scale, and Δ is the filter size of the SGS model, represented as the size of the mesh. The k_{SGS} is calculated with its transport equation:

$$\frac{\partial(\rho k_{SGS})}{\partial t} + \frac{\partial(\rho \bar{u}_i k_{SGS})}{\partial x_i} = \partial \left[\rho (\nu + \nu_t) \left(\frac{\partial k_{SGS}}{\partial x_i} \right) \right] - \rho \tau_{ij}^{SGS} \bar{S}_{ij} - C_\epsilon \frac{\rho k_{SGS}^{\frac{3}{2}}}{\Delta} \quad Eq. 19$$

where kinetic viscosity is represented by ν , $\nu_t = \frac{\mu_t}{\rho}$, and C_ϵ is a constant.

2.1.4 Volume of Fluid Method (VOF)

To determine the boundary between water and air, interFoam solver adapts the Volume of Fluid method (VOF) proposed by Hirt and Nichols (1981). The assumption made is that the velocity for water (u_w) and air (u_a) are not separated and they are both represented in the same velocity field:

$$u = u_a = u_w \quad Eq. 20$$

VOF introduces a key parameter for phase, α , to represent the phase volume fraction for every cell in the computational domain.

The α can be water volume fraction, α_w or air volume fraction, α_a and their relation is:

$$1 - \alpha_w = \alpha_a \quad \text{Eq. 21}$$

Therefore, $\alpha_w = 1$ indicates the cell has water only and $\alpha_w = 0$ indicates the cell has air only. For the interface, surge front, and in-depth where air entrainment is expected, the water volume fraction is $0 < \alpha_w < 1$.

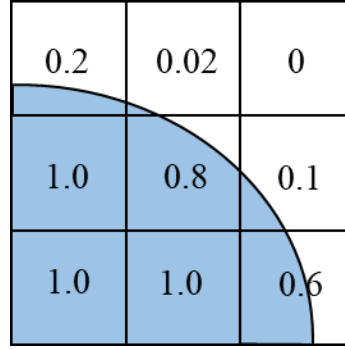


Figure 11. Water volume fraction (α_w) example during the interface capture where blue color is under the water and white color is in the air, using VOF.

Fluid properties in this method are estimated using the fractional fluid volume in each cell. For the current simulation for 2-phase air and water, based on water and air volume fractions, α_w and α_a , combined phase density and viscosity are:

$$\rho = \rho_w \alpha_w + \rho_a (1 - \alpha_w); \mu = \mu_w \alpha_w + \mu_a (1 - \alpha_w) \quad \text{Eq. 22}$$

where ρ and μ are the overall density and dynamic viscosity, respectively. With the transport equation of α_w , the interface and air entrainment patterns can be determined:

$$\frac{\partial \alpha_w}{\partial t} + \frac{\partial (\bar{u}_i \alpha_w)}{\partial x_i} + \frac{\partial}{\partial x_i} [u_{ci} \alpha_w (1 - \alpha_w)] = 0 \quad \text{Eq. 23}$$

The third term is an artificial compression term intended to sharpen the interface (Cifani et al., 2016). u_{ci} represents the relative velocity for water and air is calculated as:

$$u_{ci} = C_\alpha \frac{|u|}{|\nabla\alpha_w|} \frac{\partial\alpha_w}{\partial x_i} \quad Eq. 24$$

where C_α is a model constant for compression strength, and set to 1.

2.2 Numerical Solutions

2.2.1 Discretization Schemes

The numerical schemes are assigned in the *fvSchemes* file for various derivatives in the relative governing equations. Numerical schemes are a series of algorithms for solving partial differential equations with respect to time and space. In the *fvSchemes*, the schemes are selected for the derivative terms and discretized depending on the numerical schemes. As a result, different schemes can obtain different accuracy and stability level.

For the time derivative terms ($\partial/\partial t$), Euler scheme is assigned. According to the OpenFOAM User Guide v2012, it is applicable for transient problems, including the simulated dam-break wave in this thesis. With the following discretization:

$$\frac{\partial}{\partial t}(\phi) = \frac{\phi^{n+1} - \phi^n}{\Delta t} \quad Eq. 25$$

where ϕ is a field variable, $n+1$ is the next time step, and n is the current time step.

It is a first-order implicit time-marching scheme. Other methods include explicit and semi-implicit methods. When the time derivative term is discretized, the explicit

method is used to calculate the next time step ($n+1$) variables with the current time step (n) values such that:

$$\frac{\partial u}{\partial t} = f(u, t) \quad \text{Eq. 26}$$

discretized and transferred to

$$u_i^{n+1} = u_i^n + \Delta t f_i(u^n, t^n) \quad \text{Eq. 27}$$

And implicit method will calculate the variables in terms of the next time step as:

$$u_i^{n+1} = u_i^n + \Delta t f_i(u^{n+1}, t^{n+1}) \quad \text{Eq. 28}$$

Semi-implicit is between these two methods which adapted both current and future time steps variables. Compared between explicit and implicit methods, a larger time step is preferred for steady simulation so that a steady state can be achieved faster. For implicit method, the limit on time step is little compared to that of explicit which could benefit the process to become steady. Since the explicit method is conditionally stable, it's necessary to maintain the stability condition, Levy-Courant number. The maximum Levy-Courant number is set to one in the simulation. Also, in the case when the simulation needs to be "time accurate" for unsteady case and "local refinement" is applied, it is common to observe the implicit method as the standard built-in for CFD software rather than explicit method; even with explicit method's time step becomes smaller which could fulfill the stability demand but that doesn't necessarily provide higher accuracy (Ferziger et al., 2002). As for present simulations, the interest is placed on the fully developed surge wave which can be

further converted to a quasi-steady problem. With the implementation of implicit related schemes, it will allow for larger time steps and reach the quasi-steady state faster. The shorter process can reduce the computational time cost as well. Meanwhile, local refinement is applied along the surge front passage to increase the resolution and accuracy of the analysis. Therefore, implicit schemes are preferred for the performed simulations.

For the divergence schemes, they are applied over the advection and convection terms in the momentum equation, k_{sgs} and α_w transport equations. The spatial discretization of the convection terms is performed using different schemes based on the sensitivity of the term in the computation. The flux of sub-grid scale turbulent kinetic energy, k_{SGS} , appearing the convection term in Equation 19 is performed using a first-order upwind biased interpolation. Upwind scheme will estimate the face values as the upstream values depend on the flow direction. In the finite-volume method, with the face values, the values at next time step are determined. With fine enough mesh size, accuracy level can also be satisfied to compensate the numerical diffusion (Ferziger et al., 2002). However, the convection term in the momentum equation requires a higher-order approximation and, therefore, an upwind biased central differencing is selected. It is a combination of central differencing and upwind where the face value is estimated as the average of two points upwind (OpenFOAM User Guide v2012). As for the α_w term associated with the relative velocity, the second-order linear interpolation (central differencing) is adapted. On the other hand, for the flux of phase, α_w , in Equation 23, the van Leer Total Variation Diminishing (TVD) method is selected. TVD schemes have the advantages over upwind

which can provide a stable simulation but lower accuracy order and high order central differencing which tends to generate undesirable oscillations. TVD schemes limit the wiggling and maintain the monotonic behaviour of flow and provide a higher accuracy order meanwhile (Karimpour & Chu, 2015).

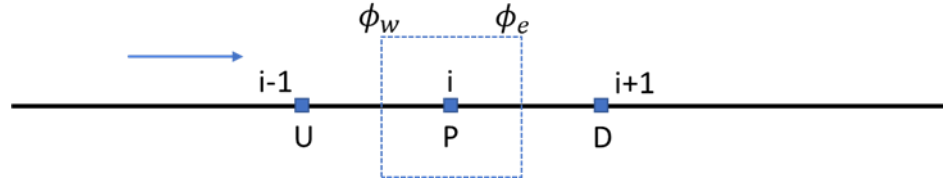


Figure 12. Illustration of the finite volume method nodes for TVD schemes.

For the flow identified in Figure 12, the schemes can be generalized to one equation to determine the face value, ϕ_e :

$$\phi_e = \phi_P + DWF(\phi_D - \phi_P) = (1 - DWF)\phi_P + DWF\phi_D \quad Eq. 29$$

The DWF in the equation is known as Downward Weight Factor. Therefore, for the case of the upwind scheme, $DWF = 0$ to achieve $\phi_e = \phi_P$; for the case of the central differencing scheme, $DWF = \frac{1}{2}$ to achieve $\phi_e = \frac{1}{2}(\phi_P + \phi_D)$. And for linear upwind differencing, DWF is defined as:

$$DWF = \frac{\phi_P - \phi_U}{2(\phi_D - \phi_P)} \quad Eq. 30$$

Then

$$\phi_e = \phi_P + \frac{1}{2}(\phi_P - \phi_U) \quad Eq. 31$$

DWF can be re-written as a function of r, where:

$$r = \frac{\phi_P - \phi_U}{\phi_D - \phi_P} \quad \text{Eq. 32}$$

Since oscillatory free is equivalent to monotonic flow, and from the Equation 32, r needs to be greater than zero. In terms of Total Variation (TV), when TV does not increase with time, the oscillatory is managed as well (Karimpour & Chu, 2015).

The applied van Leer TVD scheme is second-order accurate and is bounded and its accuracy can drop to as low as first order in regions with discontinuity. As demonstrated in Figure 2, starting from its initial condition, the moving surge wave exhibits discontinuity in phase at the surge front and it requires a TVD (or an alternative) scheme to ensure numerical stability (Karimpour & Chu, 2015). Its DWF function is defined as:

$$DWF(r) = \frac{\frac{1}{r} + \left|\frac{1}{r}\right|}{1 + \frac{1}{r}} \quad \text{Eq. 33}$$

The van Leer TVD can ideally reduce sudden changes and provide a flat transition (Tryggvason, 2017).

2.2.2 *InterFoam Solver and PIMPLE*

Since I am interested in the two phases: air and water of the positive surge wave, a multiphase solver should be selected within OpenFOAM. InterFoam is one of the multiphase solvers specifically designed for two fluids that are immiscible. Meanwhile, it is suitable for incompressible, transient flow and it supports the turbulent modelling and finite volume method (Greenshields, 2015). It is using the PIMPLE algorithm to solve the Navier-Stokes equations for velocity pressure decoupling and is a combination of two

different algorithms: one is based on Semi-Implicit time integration, for Pressure-Linked Equations (SIMPLE) and the second is Pressure Implicit Splitting Operator (PISO).

SIMPLE, PISO and PIMPLE are commonly applied in OpenFOAM and they are working in the similar way called "predictor-corrector". The goal is to solve for the next time instance t^{n+1} , which is the current time instance t^n plus the time step, Δt . For PIMPLE algorithm, start with the “predictor” which will have an initial guess of pressure, and according to the pressure, perform discretization on the momentum equation to determine the corresponding velocity. The next step will be the “corrector”, from the velocity, build and perform discretization on the pressure equation to determine the updated pressure. With the updated pressure, find the new velocity with the momentum equation. When the results are converged, the new fields are calculated for t^{n+1} . Otherwise, the loop will restart since the “predictor” step, until it is converged (Ye et al., 2020).

2.3 Numerical Flow Framework

2.3.1 Surge Wave Froude Number, Fr_s

As shown in Figure 13, the wave will move with a speed, also known as the positive surge celerity, c ; the water level downstream is d_1 ; the water level behind the surge front is annotated as d_2 ; downstream water velocity, U_1 ; velocity behind the surge front, U_2 .

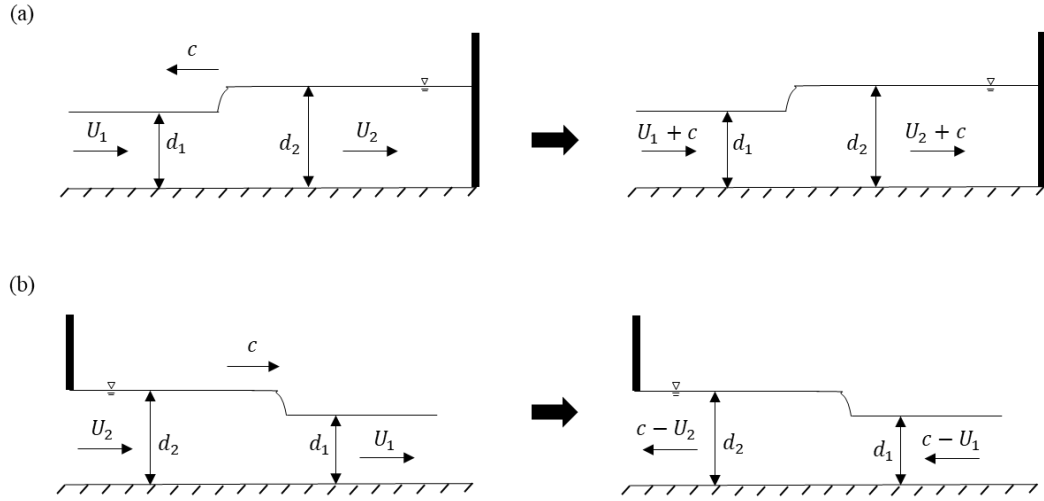


Figure 13. Analogy method of transferring the transient positive surge waves to quasi-steady state hydraulic jump assuming the observer is moving together with the surge front at a celerity of c . Positive surge waves can be generated with (a) suddenly closure of the gate; (b) opening of the gate, also known as the dam-break wave.

Therefore, for case (a) in Figure 13(a), surge wave Froude numbers can be defined as the following in the quasi-steady state:

$$Fr_1 = \frac{U_1 + c}{\sqrt{gd_1}} \quad Eq. 34$$

$$Fr_2 = \frac{U_2 + c}{\sqrt{gd_2}} \quad Eq. 35$$

This definition is analogous with convective Froude number defined by Karimpour and Chu (2016, 2019) based on the velocity difference across the mixing layer. Similarly, for the dam break waves that are simulated:

$$Fr_1 = \frac{c - U_1}{\sqrt{gd_1}} \quad Eq. 36$$

$$Fr_2 = \frac{c - U_2}{\sqrt{gd_2}} \quad Eq. 37$$

As noted by Chanson (2004), the positive surge waves are typically characterized by the surge wave Froude number at the front, Fr_1 . Since $U_1 = 0 \text{ m/s}$, for the dam-break wave:

$$Fr_s = Fr_1 = \frac{c}{\sqrt{gd_1}} \quad Eq. 38$$

2.3.2 Method of Characteristics (MOC)

The flow conditions of the positive surge waves can be predicted based on an analytical solution known as Method of Characteristics (MOC). Figure 14 shows how three points of interest are represented in the plot of time and x locations, which are the negative surge wave point, behind surge wave point and a surge front point. d_0 is the reservoir depth and c_0 is the negative surge celerity.

According to Chanson (2004), by solving the system of continuity, momentum and MOC equations the unknown variables: U_2 , c and d_2 can be solved by knowing d_1 and d_0 .

Continuity equation:

$$d_1(c - U_1) = d_2(c - U_2) \quad Eq. 39$$

Momentum equation:

$$d_2(c - U_2)^2 - d_1(c - U_1)^2 = \frac{1}{2}gd_1^2 - \frac{1}{2}gd_2^2 \quad Eq. 40$$

Forward characteristics:

$$U_2 + 2\sqrt{gd_2} = 2\sqrt{gd_0} \quad Eq. 41$$

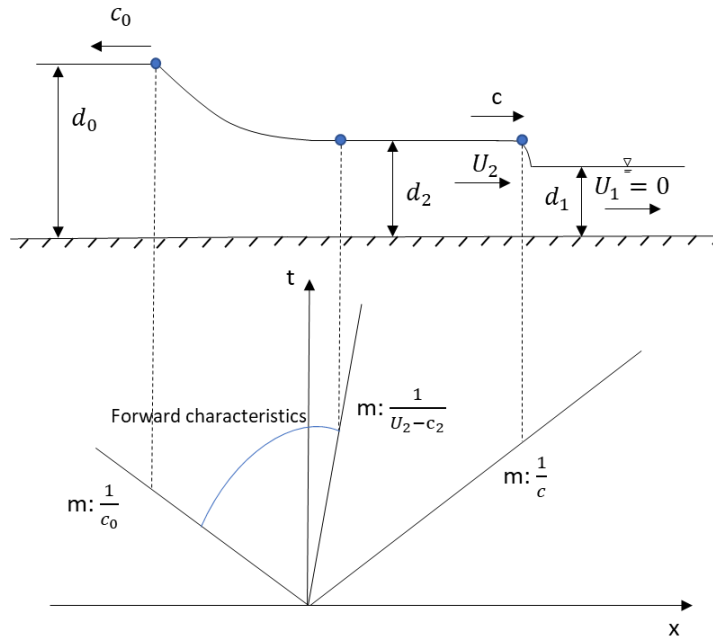


Figure 14. Illustration of the MOC for positive surge waves, m is the slope of the characteristics line.

Also the following semi-analytical equations were proposed by Chanson (2004):

$$c_0 = \sqrt{gd_0} \quad Eq. 42$$

$$\frac{d_2}{d_1} = 0.9319671 \left(\frac{d_1}{d_0} \right)^{0.371396} \quad Eq. 43$$

$$Fr_1 = \frac{c}{\sqrt{gd_1}} = \frac{0.63545 + 0.3286 \left(\frac{d_1}{d_0}\right)^{0.65167}}{0.00251 + \left(\frac{d_1}{d_0}\right)^{0.65167}} \quad Eq. 44$$

2.3.3 Computational Domain and Flow Conditions

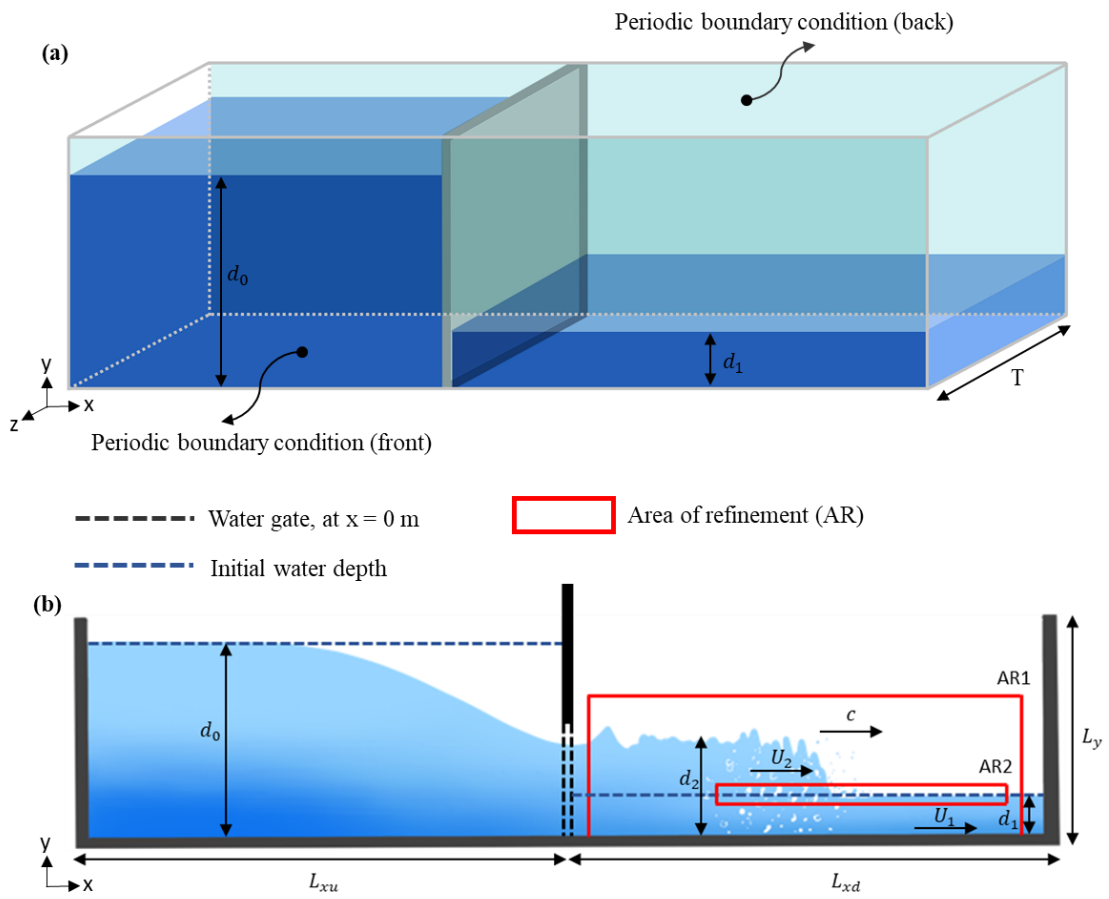


Figure 15. Sketch of the computational domain. (a) 3D view of the initial reservoir; (b) front view of the surge wave.

Figure 15 shows the 3D view of the computational domain and 2D front view of a positive surge wave. AR1 covers the passage of the surge wave so that the detail behind and at the surge front increases. With one level of refinement in AR1, the resolved percentage of Turbulent Kinetic Energy did not meet the 80% threshold near the toe for high quality simulation. The detail is provided in the later section. Therefore, an additional level of refinement is incorporated near the toe, labelled as AR2 to provide sufficient fine mesh and reach the 80% threshold. L_y is the height of the domain, L_{xu} is the length before the gate, L_{xd} the length after the gate, and T is the thickness of the domain.

Leng and Chanson (2017) and Zheng et al. (2018) have reported undular waves at surge wave Froude numbers up to $Fr_s \approx 1.5$. This project, therefore, covers surge Froude numbers beyond this range as it aims to investigate the turbulent properties across the surge breaking front. For all the modelled cases, $d_0 = 1$ m, $L_y = 1.2$ m, $c_0 = \sqrt{gd_0} = 3.13$ m/s.

ID	d_1 (m)	d_0 (m)	c (m/s)	d_2 (m)	AR1 (m ²)	dx_1 (m)	AR2 (m ²)	dx_2 (m)	Fr_s	T (m)
1	0.3	1.0	2.93	0.596	22*0.7	0.005	6.95*0.1	0.0025	1.71	40 Δx
2-1	0.2	1.0	2.98	0.513	22*0.6	0.005	7.30*0.1	0.0025	2.13	10 Δx
2-2	0.2	1.0	2.98	0.513	22*0.6	0.005	7.30*0.1	0.0025	2.13	20 Δx
2-3	0.2	1.0	2.98	0.513	22*0.6	0.005	7.30*0.1	0.0025	2.13	40 Δx
3	0.15	1.0	3.02	0.461	22*0.56	0.005	7.01*0.1	0.0025	2.49	40 Δx

Table 1. Flow conditions of the modelled positive surge flows and mesh information.

The flow variables in Table 1 were selected based on the Method of Characteristics, described in the previous section. From Equation 44, pre-defined $\frac{d_1}{d_0}$ will determine the expected Fr_s of a surge wave to be in the range of breaking wave. Therefore, c can be calculated and the $L_{xu} = c_0 * t$, $L_{xd} = c * t$, where t is the moving time of the surge. The computational domain length design will ensure that the wave will not be reflected at the end wall, and the depth of the upstream reservoir will not be reduced. d_2 is calculated with Equation 43, and U_2 is calculated with Equation 39.

2.3.4 Boundary Conditions

The computational domain is surrounded by three rigid walls where smooth boundary conditions are applied, for the left, right and bottom patches and with the top patch open to the atmosphere. Therefore, for the velocity, U , no-slip boundary conditions are assigned for the walls; for the subgrid scale TKE, k_{SGS} , and eddy viscosity, ν_t , wall functions are assigned for the walls.

The front and back patches are set to periodic boundary conditions. In order to achieve fully-developed turbulent flow across a breaking surge wave, this study has implemented periodic boundary condition in the spanwise z -direction. This technique is used in open-channel flow, such as the work of Kim et al. (1987) and in other flow types Munters et al. (2016) to produce a fully developed turbulent flow, where the perturbations are fed back into the domain. The size of the periodic domain width, T , however, should be selected so that it is several times larger than the largest scale in the domain (Munters

et al., 2016). The turbulent scale, however, is not studied for breaking waves. Therefore, in order to fully capture all turbulent scales, including large scales, this study has implemented multiple domain width sizes, T , and have assessed the role of domain width on the growth of spanwise turbulent fluctuations.

2.3.5 Computational Resources

The modelling of positive surge waves starts with the investigation of 2D cases. The 2D cases are different from the 3D cases by setting the number of grids in z-direction as 1 and the front and back patches are empty in the OpenFOAM, during the mesh generation. The 2D study is conducted by connecting to the computers on campus. The desktop computer has better performance in terms of computational speed. Also, it has a NVIDIA Quadro p400 graphic card which allows for the visualization and post-processing of results without transferring the data from the saved location. The desktop is equipped with Intel Core i9-10900K CPU @ 3.70GHz, 10 Cores, and 64GB physical memory and the corresponding computational time for a 2D case with local refinement is to be completed in about one month. Besides the hardware perspective, to further increase the computational speed, “parallel processing” technique is applied. The idea of parallel processing is to make use of multiple processors instead of only letting a single processor perform a serial processing (Afzal et al., 2017). In OpenFOAM, the parallel processing is achieved by “domain decomposition” and message passing interface (MPI) tool (OpenFOAM User Guide). So that the domain is decomposed into several subdomains with each of them is taken care of by a processor. For a particular time instance, instead of putting all the pressure on one

processor to solve the whole domain, each processor only solves a portion of the domain. Processors amount is determined based on trial and error of a test case. The simulation is selected to be short and the number of processors that has the shortest time to complete is selected. After reconstructing the decomposed data, the data for the overall domain is obtained. MPI is common to use for parallel computing and computers with excellent performance. The information is transferred from a subdomain to the adjacent one (Afzal et al., 2017). With the parallel processing implemented, the computational time for the 2D cases is reduced to half.

The computational domain is decomposed into 12 subdomains and the method selected will arrange subdomains horizontally. The array of subdomains is similar to the sketch shown in Figure 16, where each of them has the same amount of meshes. Therefore, each processor will finish the calculation for the time step with a similar time to avoid the waste of resources by waiting for other processors to complete. The reason that 12 subdomains are distributed horizontally only but not divided in the y or z direction is to lower the communication load with fewer grids at subdomains' interfaces, which will increase the efficiency of parallel processing. The communication is necessary to maintain coherence of the overall simulation (Keough, 2014).

As moving on to the 3D simulations, the maximum number of grids in the domain quadrupled. Therefore, the computational time increased significantly as well. A solution that can provide a substantial improvement of computing capacity is needed. Compute Canada which includes different clusters across Canada provides high-performance

computing (HPC). As shown in Table 2, even with the top-tier HPC, and optimal number of processors and physical memory selected, the computational time will still be about a month for every $T = 40\Delta x$ case. Besides the cases that are presented here, there have been many trial simulations and meanwhile the abandoned cases that were not properly simulated. Thus, with such exceedingly long computational time and numerous data points for post-processing, eventually the cases that can represent three breaking surge Froude numbers are exhibited in the thesis.

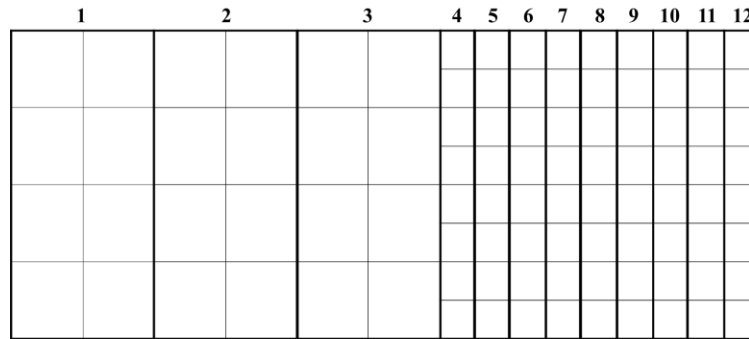


Figure 16. Demonstration of subdomains in parallel processing.

Case ID	Number of processors	Processor's type	Memory per CPU	Simulation duration
1	12	Intel E5-2683 v4 Broadwell @ 2.1 Ghz	10 GB	33 d
2-1	12	Intel E5-2683 v4 Broadwell @ 2.1 Ghz	10 GB	12 d
2-2	12	Intel E5-2683 v4 Broadwell @ 2.1 Ghz	10 GB	18 d
2-3	12	Intel E5-2683 v4 Broadwell @ 2.1 Ghz	10 GB	29 d
3	12	Intel E5-2683 v4 Broadwell @ 2.1 Ghz	10 GB	32 d

Table 2. Computational resources and duration for the simulated cases.

Chapter 3

Results and Discussion

After the completion of the simulation produced by OpenFOAM, results can be visualized and post-processed using ParaView. The simulations were used to calculate the values of variables such as velocity, phase, pressure, eddy viscosity, and the subgrid scale turbulent kinetic energy. The primary objective is to correlate the turbulent structure statistics and air entrainment patterns for the surge front at different surge Froude numbers along with the investigation of 3D spanwise size and grid resolution regards LES turbulent modelling. Beyond ParaView, “in-house” MATLAB codes were developed for air-water interface identification and ensemble averaging of this transient phenomenon. This chapter starts with the general behaviour of the computed surge waves, and then analysis of the turbulent kinetic energy (TKE), water depth perturbations, air entrainment profiles, velocity perturbations quadrant analysis and finally the turbulent vortices.

3.1 Phase and Velocity Contours

To demonstrate the appearance of a propagating surge wave, firstly, the water volume fraction, α_w , is plotted in time. The process of the water being released from the gate and becoming a fully developed state of wave can be observed as well. Moreover, the variation of the surface profiles and air entrainment properties with respect to time play an important role in the analysis. Based on the simulated results, the surge front and surrounding have the strongest and chaotic turbulent structure accompanied with abundant air entrainment.

Meanwhile, at $t < 2$ s the wave front is not fully developed and therefore, developing stage of the surge waves can not represent the characteristics of the surge wave properly, as shown in Figure 17(d).

Therefore, the results are plotted by focusing on the surge front area and after $t = 4$ s corresponding to the stage of a developed surge wave as shown in Figures 17(a), (b) and (c) for Fr_s of 1.71, 2.13 and 2.49, respectively.

As demonstrated in Figure 17, three time instants are selected: $t = 4.0, 4.5, 5.0$ s, of the positive surge waves move from upstream to downstream (left to right) and intruding into the downstream still water with a celerity, c . The surge wave height maintains nearly constant as the wave moving.

Solid blue colour represents the pure water such as at the undisturbed downstream; whitish colour represents aeration zone. Firstly, as waves move forward, air bubbles are generated near the surge front, with numerous small air bubbles trailing behind the surge. Since the Fr_s are in the range of breaking surge waves, it is expected to observe a significant amount of air entrainment.

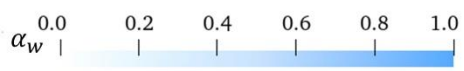
Secondly, discontinuity over depth is observed which starts from the surge toe. Typically, the free surface at the surge front is bending outward. These observations agree with the laboratory work by Gualtieri & Chanson (2012) for breaking waves by probing data collection approach. The red lines in Figures 17(a) (b) and (c) are developed based on the celerity calculated from the MOC for three Fr_s mentioned in section 2.3.2. The surge front's position predicted by the MOC celerity is similar to the simulated results.

Therefore, the impact of friction is negligible and MOC celerity can properly estimate the relative position of the surge front. Thus, the theoretical c is utilized during finding the ensemble average which will be provided with more details in the next section.

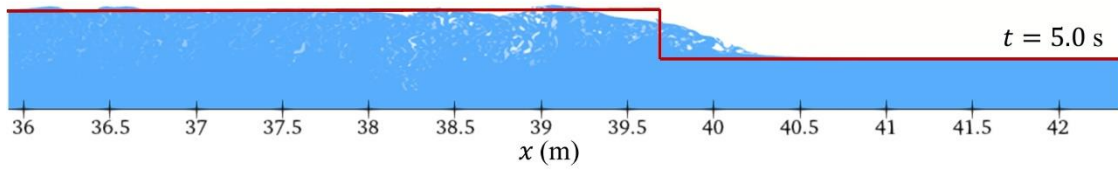
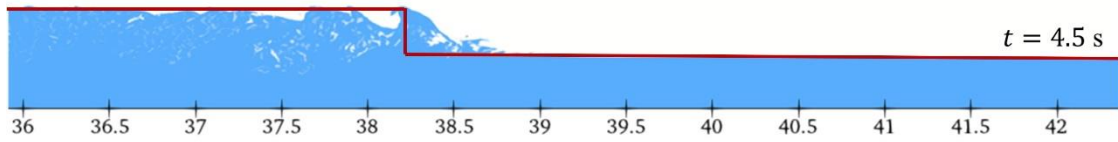
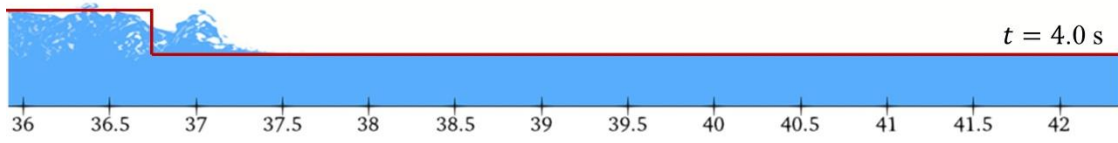
Streamwise velocity, u , dominates the movement of the wave and it has a greater magnitude relative to y-direction velocity, v and z-direction velocity, w . Therefore, u contours are plotted as shown in Figure 18. With the contour filter applied during post-processing the velocity data in ParaView, isolines of $\alpha_w = 0.5$ are added above the u field. They are shown as dark grey lines in Figure 18. Isolines of $\alpha_w = 0.5$ represents the surface profiles of the surge waves.

The strongest u is observed near the toe in common for different times and Fr_s and diminishing as the surge front has passed. The range of u at $Fr_s = 1.71$ is between -0.7 and 6.1 m/s, at $Fr_s = 2.13$ is between -0.97 and 5.52 m/s and at $Fr_s = 2.49$ is between -3.01 and 5.94 m/s.

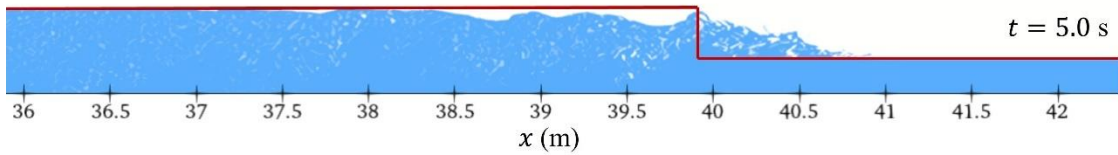
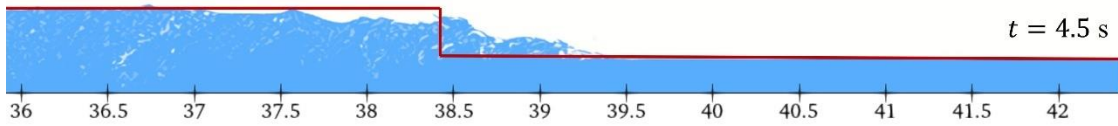
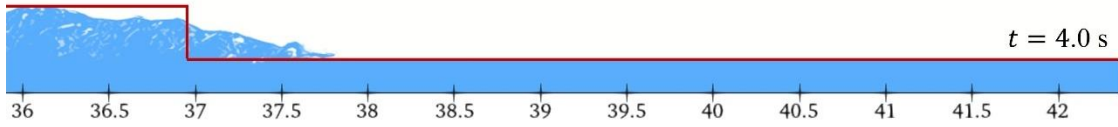
Meanwhile, in the vertical direction, there is also a velocity discontinuity, especially behind the surge front. For example, in Figure 18(a) at $t = 5$ s, near the surge front surface, the flow velocity can reach as high as 3.8 m/s but decrease sharply to about 0.5 m/s next to the bed behind the surge. With the u fields that are shared by the water and air, negative u are observed mostly in the air zone. Some exceptions have negative u under the surge wave. Such as the enlarged view in Figure 18(a) for $Fr_s = 1.71$ at $t = 5$ s, as well as in Figure 18(b) for $Fr_s = 2.13$ at $t = 4$ s also locates under the surge wave, which exhibits blue color as negative u .



(a)



(b)



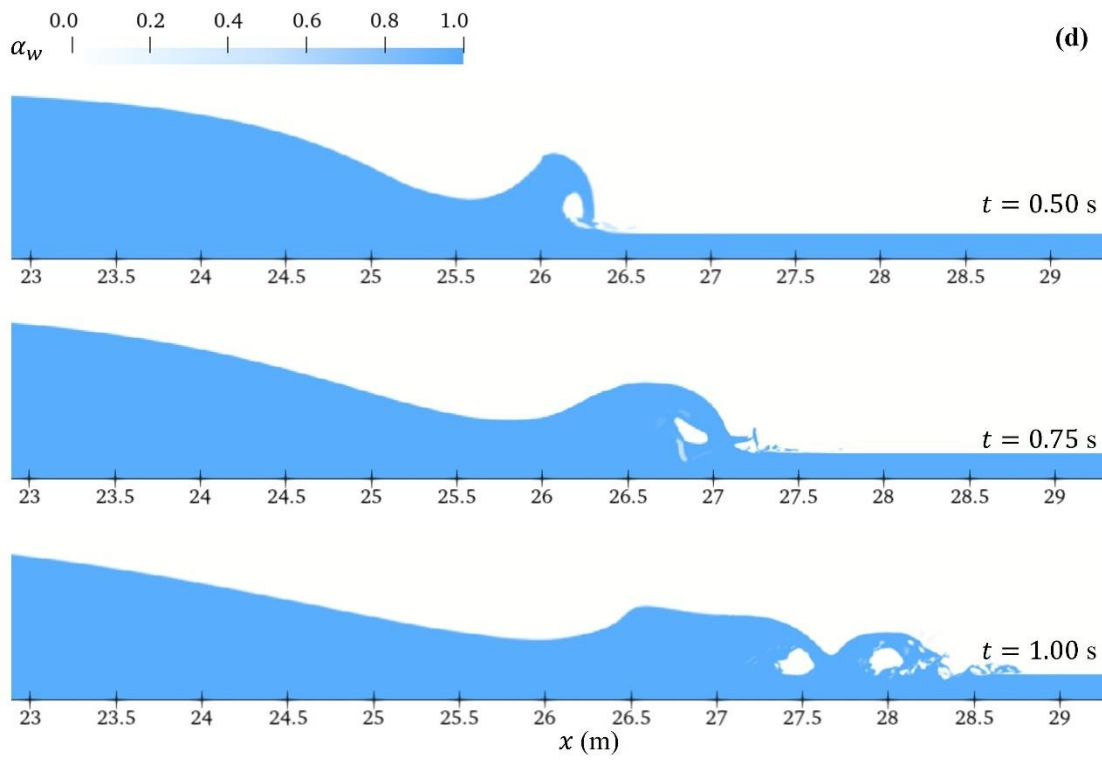
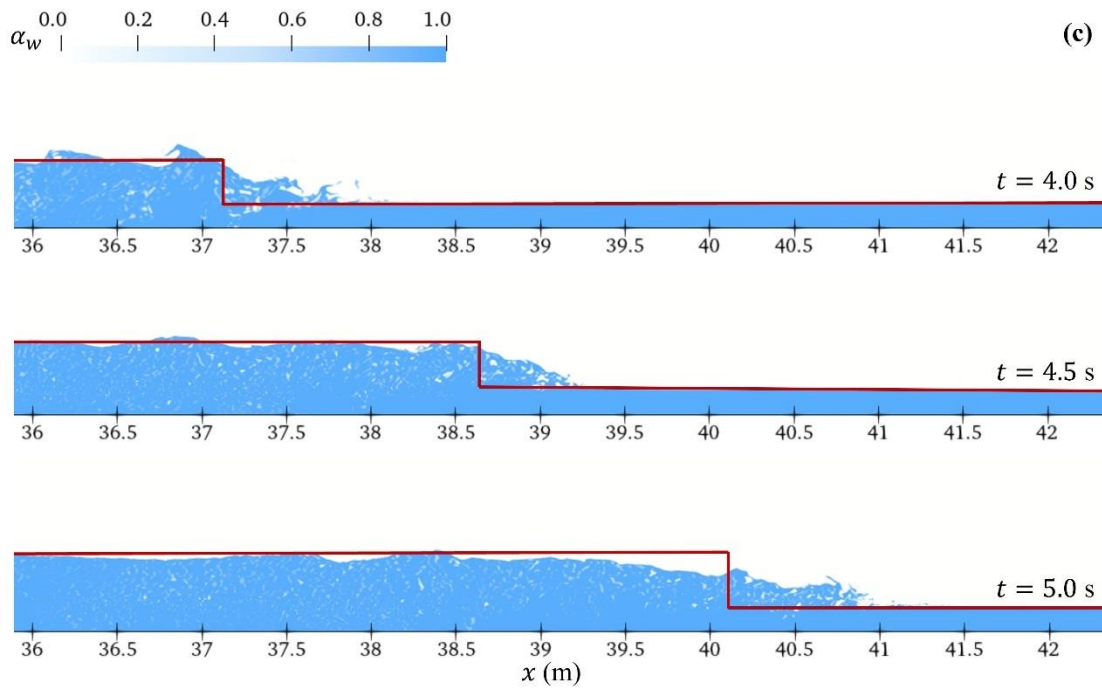
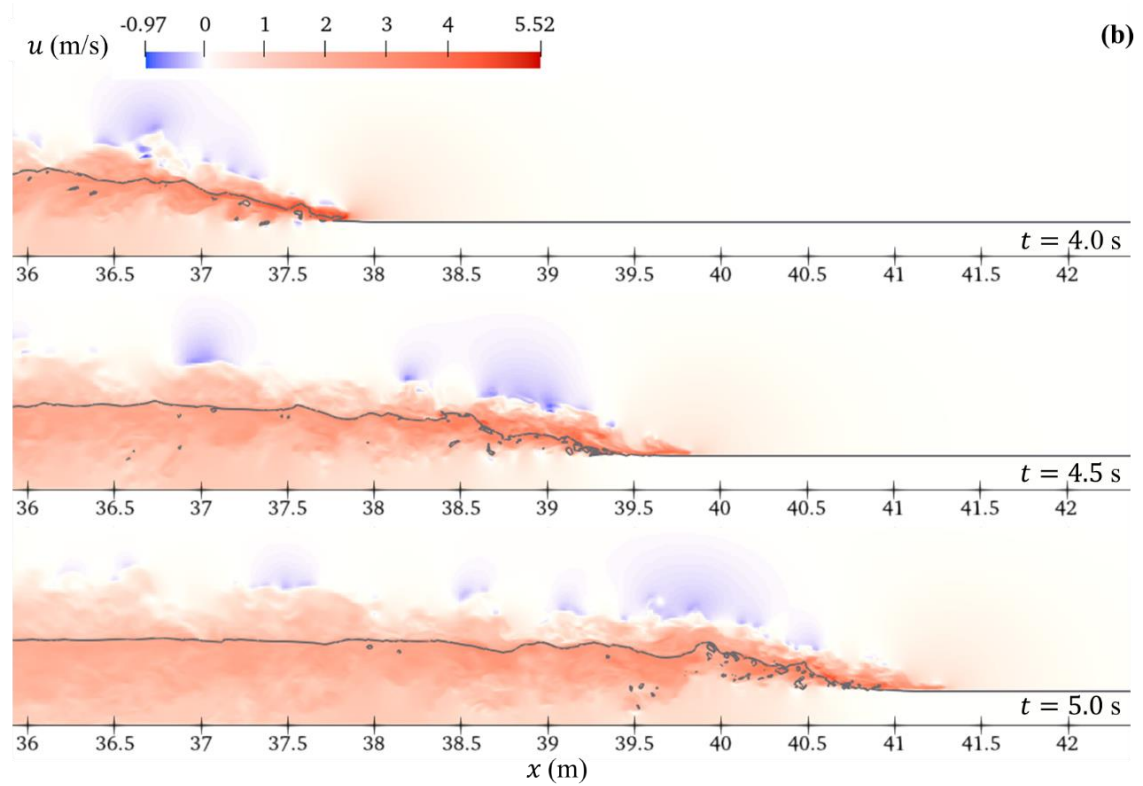
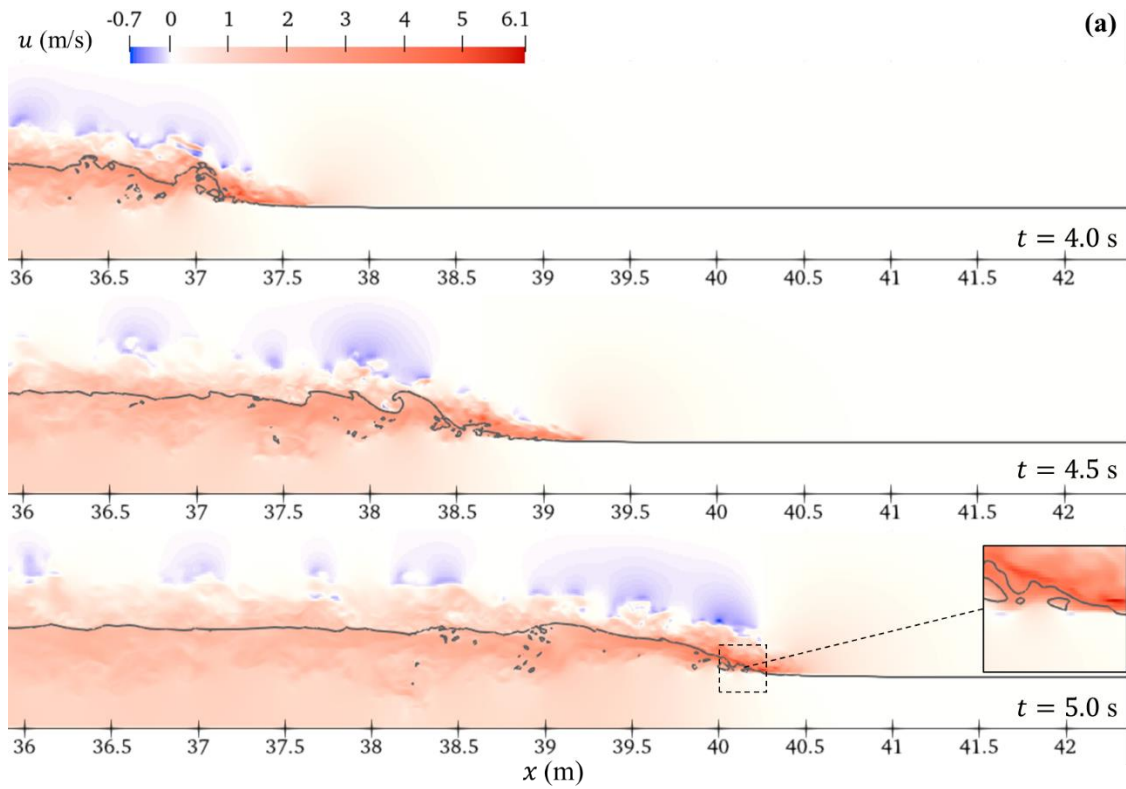


Figure 17. Propagating surge wave where α_w is water volume fraction, toward downstream with time, at $t = 4.0, 4.5$ and 5.0 s, for Fr_s of (a) 1.71, (b) 2.13, (c) 2.49. Red line outlines the free surface based on c from MOC. (d) shows initial stage at $Fr_s = 2.49$.

This phenomenon is also reported by Gualtieri & Chanson (2011) which is captured by the probe with a momentary period. Such rapid direction-changing behaviour can be explained as “flow separation” under the transient wave.

The streamwise velocity relative to the theoretical velocity behind the surge, u/U_2 , is plotted in Figure 19 for $Fr_s = 2.13$. U_2 is calculated based on the MOC mentioned in section 2.3.2. From the plots, theoretical velocity behind the surge, U_2 , has an obvious difference with the actual velocity behind the surge in the simulation. At the area closer to the surge front, the difference is greater. At a distance further upstream from the surge front, the difference between two velocities is smaller. Besides, the flow is not uniform so a constant velocity U_2 can not represent the actual flow. Therefore, from this comparison, 3D numerical modelling of the positive surge wave has a great advantage compared to the 1D analytical methods, such as MOC.



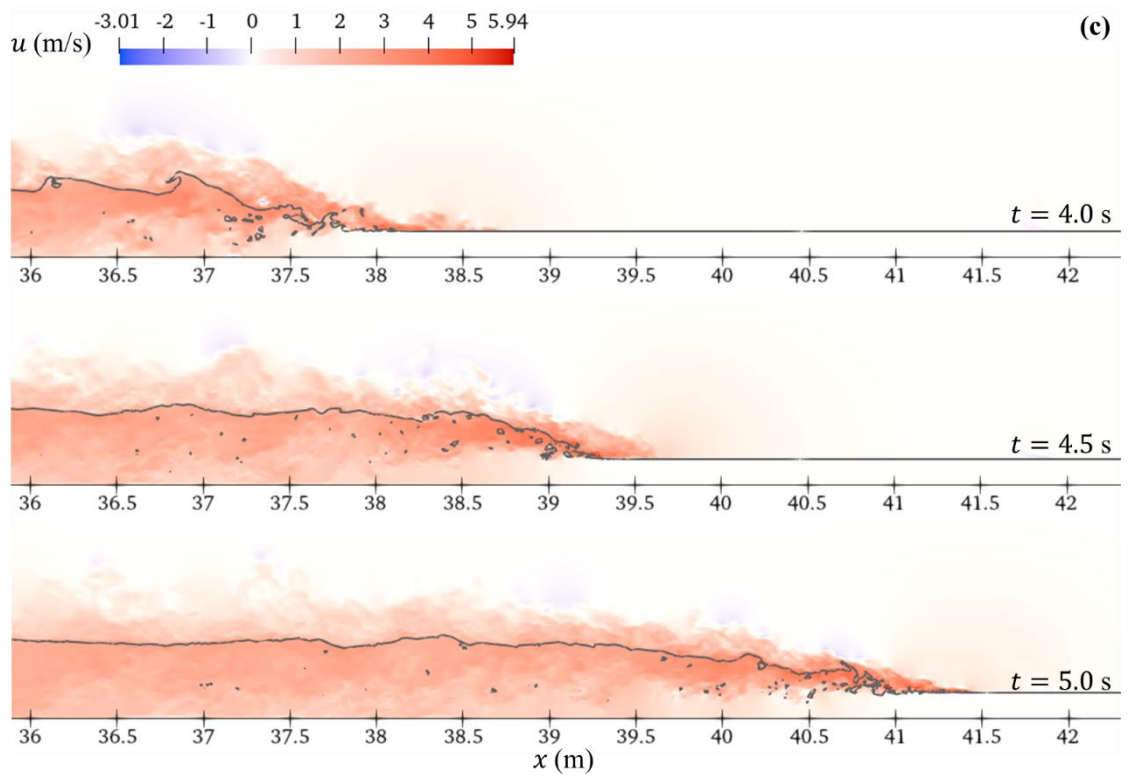


Figure 18. Plot of the velocity field (u , m/s) variation with time, at $t = 4.0, 4.5$ and 5.0 s, for Fr_s of (a) 1.71, (b) 2.13 and (c) 2.49.

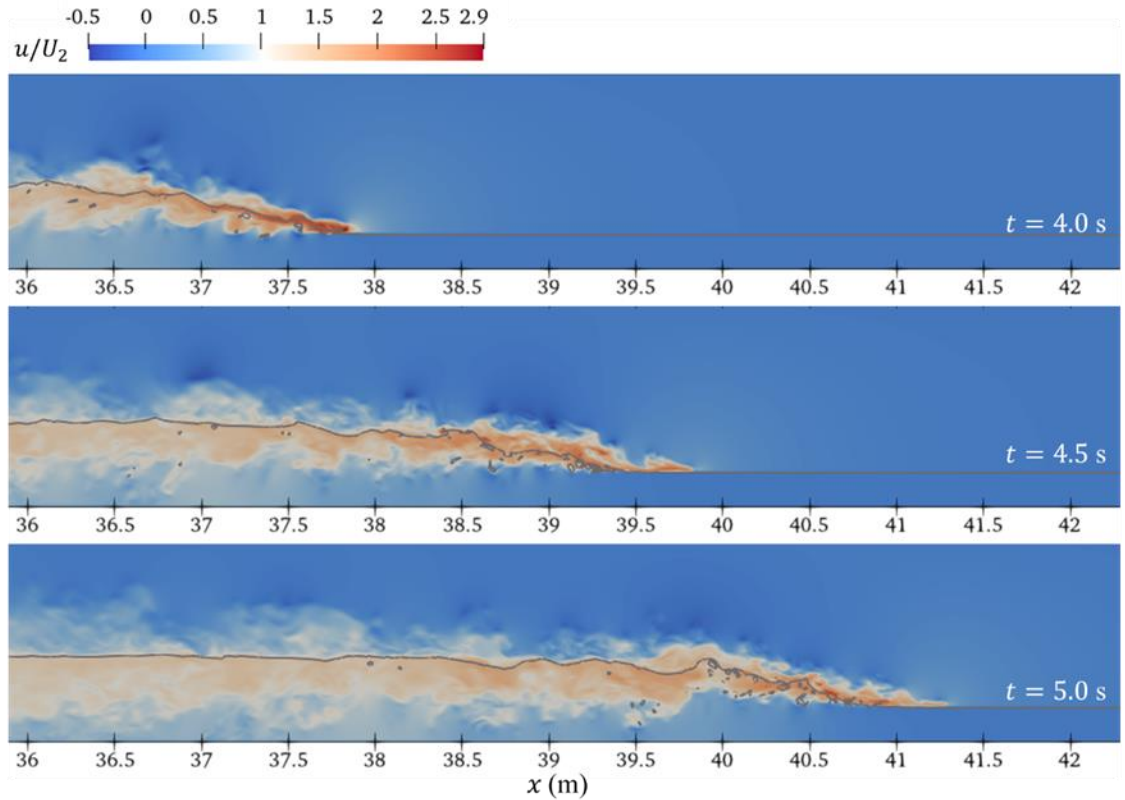


Figure 19. Plot of the velocity field relative to theoretical velocity behind the surge (u/U_2), at $t = 4.0, 4.5,$ and 5.0 s, for $Fr_s = 2.13$.

3.2 Q-criterion Analysis and Relation to Production

Due to the complexity of the flow, with multiple instability inducing mechanisms, the plot of vorticity alone does not shed light on the vortical circulations, also reported by Lubin and Glockner (2015). Instead, Q-criterion is used to visualize the formation, rolling, and merging of the coherent structures.

This criterion was introduced by Hunt et al. (1988) and it is defined in terms of the instantaneous velocity gradients.

$$Q = \frac{1}{2} (\|\boldsymbol{\Omega}\|^2 - \|\mathbf{S}\|^2) \quad \text{Eq. 45}$$

where $\boldsymbol{\Omega}$ represents the rotational vortices, \mathbf{S} represents strain-related movement.

$$\boldsymbol{\Omega} = \frac{1}{2} [\nabla \mathbf{U} - (\nabla \mathbf{U})^T] \quad \text{Eq. 46}$$

$$\mathbf{S} = \frac{1}{2} [\nabla \mathbf{U} + (\nabla \mathbf{U})^T] \quad \text{Eq. 47}$$

Positive value for Q-criterion identifies rotation-dominated regions of the flow, or vortices. Similarly, negative values are associated with straining regions of the flow. Figures 20, 21 and 22 are the plots of Q-criterion and Q iso-surface (at Q=2000) in the xy -plane for $Fr_s = 1.71, 2.13$ and 2.49 for $T = 40\Delta x$. The instantaneous plots of Q contours, show the accumulation of vortices adjacent to the toe and behind the breaking surge front. Vortices are generated by two instability mechanisms outlined earlier and are advected behind the surge. Therefore, concentrated vortices are observed near the toe where shear instability happens and right behind the breaking surge front where phase discontinuity exists.

As seen in Figure 20, both from instantaneous contour plots and isosurfaces, the vorticity formation is constrained to the vicinity of the toe and surge front. As the Froude number increases, the Q-criterion contours, as should in Figures 21 and 22, progressively spreads further in depth. This is evident from $Fr_s = 1.71$ to 2.13 and to 2.49 . Furthermore, as explained in the literature review, Chapter 1, a shear layer is originated at the toe and forms and spreads behind the toe. The Q-criterion profiles in Figures 23 and 24 shows the spread of vorticity with moving the yz cross section further upstream.

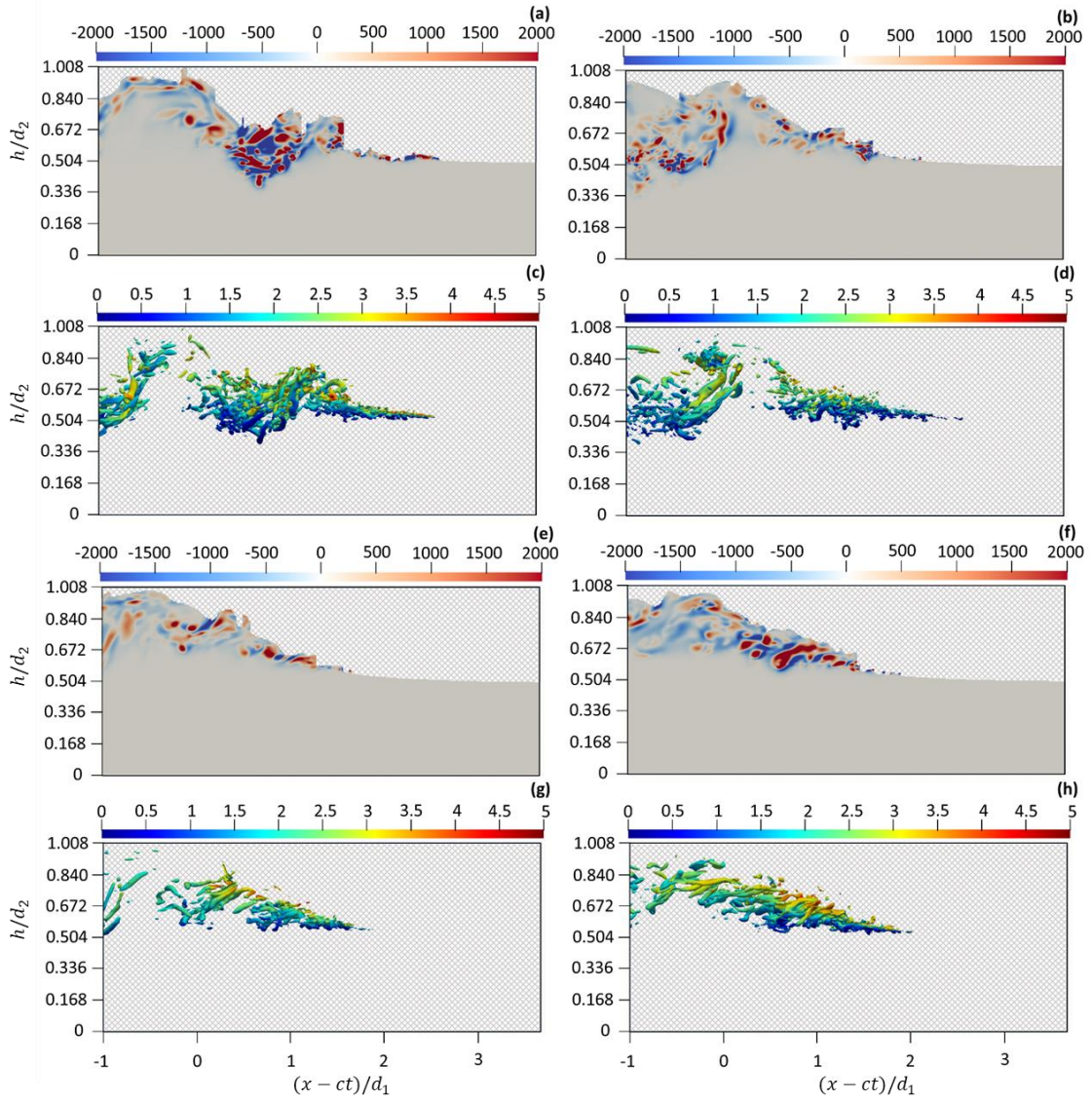


Figure 20. Plots of the instantaneous Q -criterion contour and $Q = 2000$ isosurfaces on the xy -plane at $z = 0.2$ m. The isosurfaces are colored with the resultant velocity. (a) (c) $t = 4.25$ s; (b) (d) $t = 4.50$ s; (e) (g) $t = 4.75$ s; (f) (h) $t = 5.00$ s for $Fr_S = 1.71$.

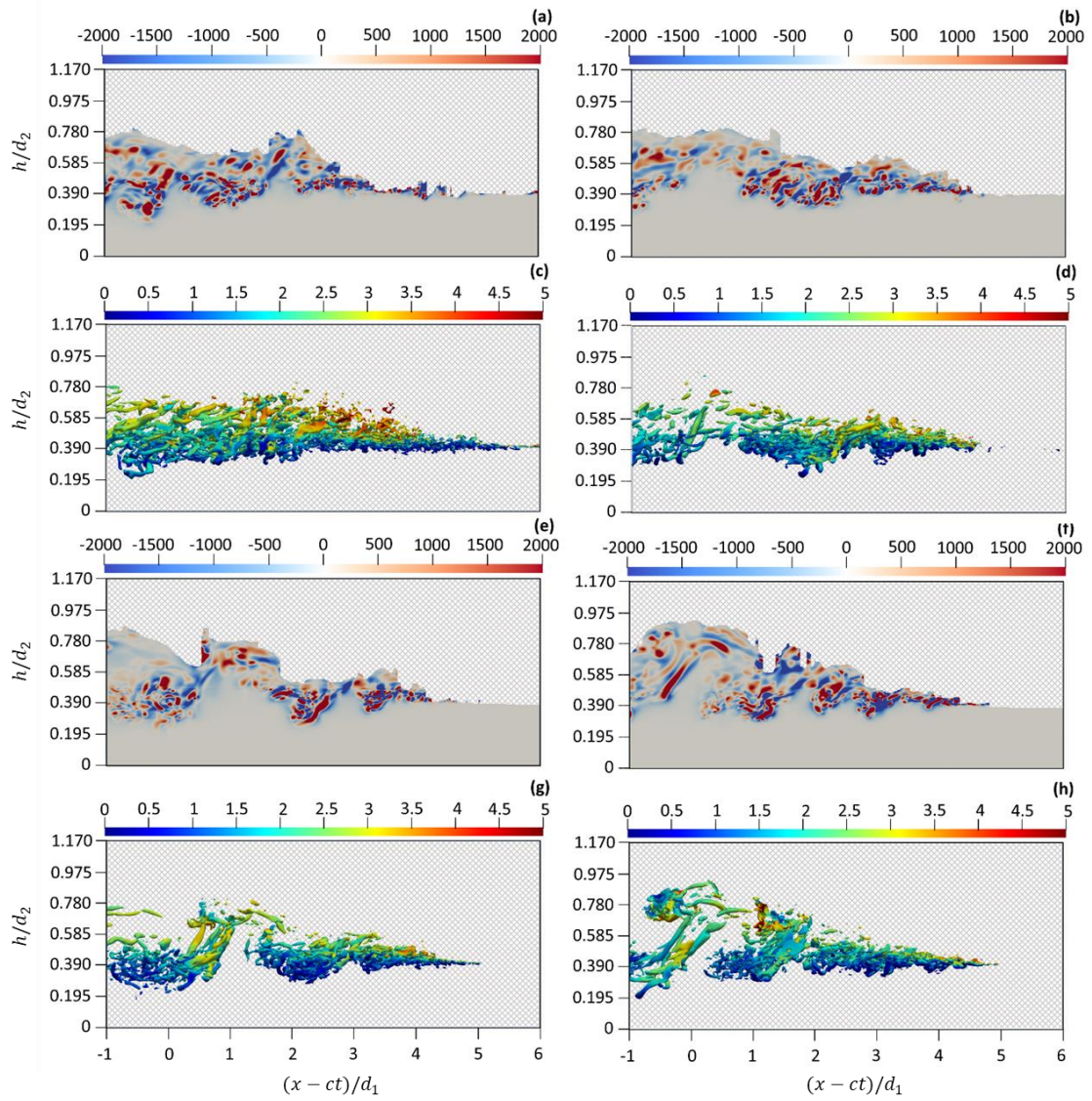


Figure 21. Plots of the instantaneous Q -criterion contour and $Q = 2000$ isosurfaces on the xy -plane at $z = 0.2$ m. The isosurfaces are colored with the resultant velocity. (a) (c) $t = 4.25$ s; (b) (d) $t = 4.50$ s; (e) (g) $t = 4.75$ s; (f) (h) $t = 4.93$ s for $Fr_s = 2.13$.

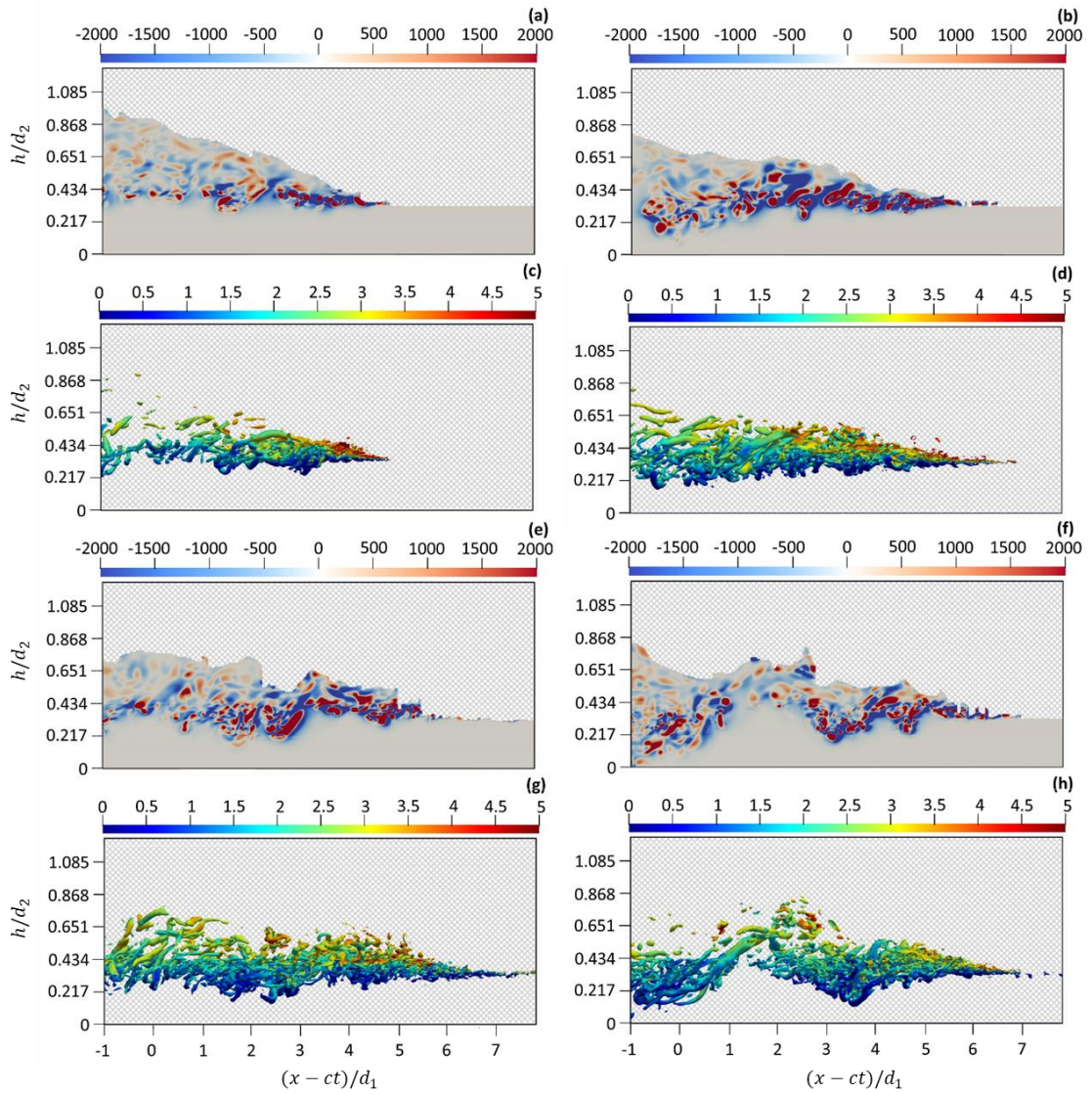


Figure 22. Plots of the instantaneous Q -criterion contour and $Q = 2000$ isosurfaces on the xy -plane at $z = 0.2$ m. The isosurfaces are colored with the resultant velocity. (a) (c)

4.50 s; (b) (d) $t = 4.75$ s; (e) (g) $t = 5.00$ s; (f) (h) $t = 5.50$ s for $Fr_s = 2.49$.

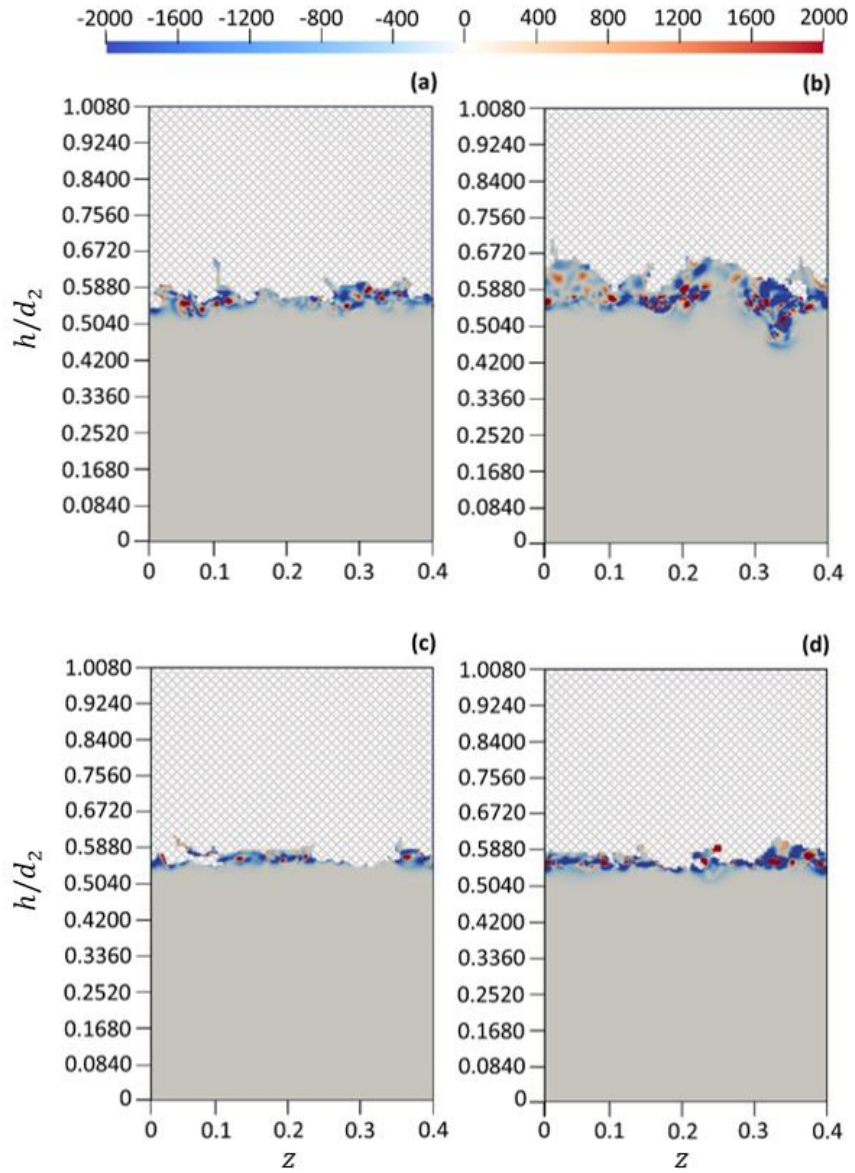


Figure 23. Plots of Q -Criterion contour on the yz -plane at $(x - ct)/d_1 = 1.5$ for $Fr_s = 1.71$ at (a) $t = 4.25$ s; (b) $t = 4.50$ s; (c) $t = 4.75$ s; (d) $t = 5.00$ s.

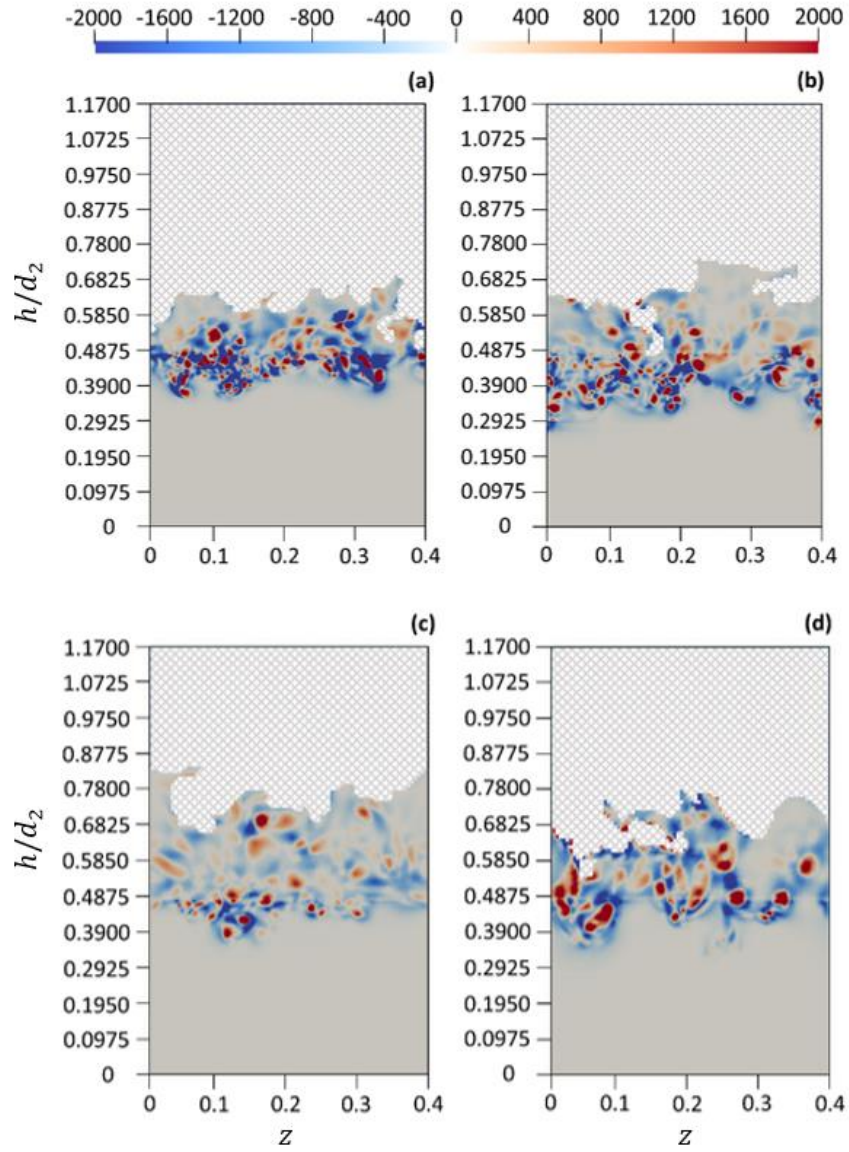


Figure 24. Plots of Q -Criterion contour on the yz -plane at $(x - ct)/d_1 = 1.5$ for $Fr_s =$

2.13 at (a) $t = 4.25$ s; (b) $t = 4.50$ s; (c) $t = 4.75$ s; (d) $t = 4.93$ s.

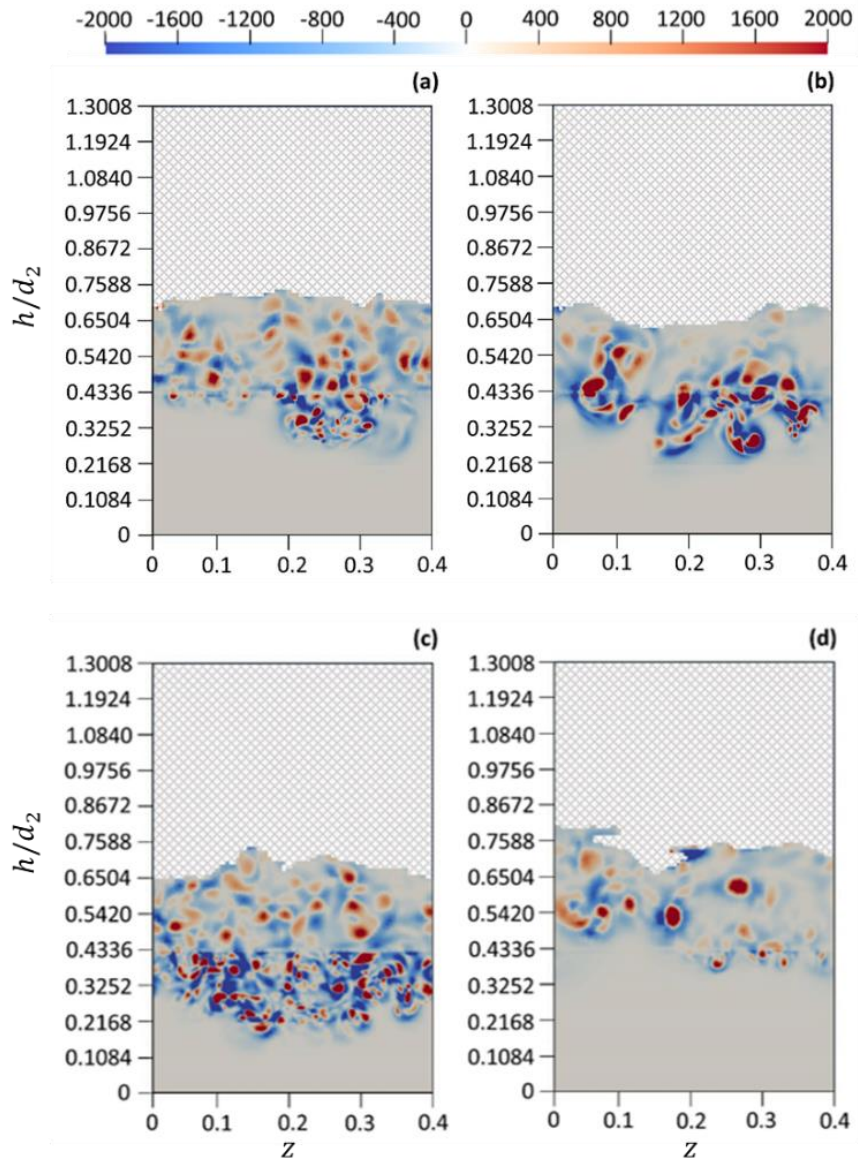


Figure 25. Plots of Q -Criterion contour on the yz -plane at $(x - ct)/d_1 = 1.5$ for $Fr_s =$

2.49 at (a) $t = 4.50$ s; (b) $t = 4.75$ s; (c) $t = 5.00$ s; (d) $t = 5.50$ s.

3.3 Shifting and Ensemble Average

As surge waves are moving and varying with time towards downstream, it is a challenge to obtain the average results of the wave. Since it is important to determine the general behaviour of the moving surge, a shifting mechanism is applied in the data analysis. The surge front moves with a celerity that is approximated with the Method of Characteristics (MOC). The ensembles, therefore, have a space lag, x_{lag} , moving with surge wave celerity, c . The results are obtained by using 100 ensembles between $t = 4$ and 6 s when the turbulent at the wave front is fully developed. To capture this transient nature, a 4-meter rectangular domain spanning from $x_1 = 35$ m to $x_2 = 39$ m is selected at $t = 4$ s. The domain boundaries in the x-direction move with the surge wave celerity of c , estimated from MOC. In cases where the shifted boundaries do not overlap with the grid alignment, a weighted algorithm is applied. The weight factors are determined based on the distance to the two adjacent grid points. This is demonstrated in Figure 26 for $t = 4.05$ s and $Fr_s = 2.13$, where the celerity is $c = 2.9835$ m/s. Two factors in the example are calculated as:

W for $x_1 = 35.145$ m, $x_2 = 39.145$ m:

$$\frac{0.15 \text{ m} - 0.149175 \text{ m}}{0.15 \text{ m} - 0.145 \text{ m}} = 0.165$$

W for $x_1 = 35.15$ m, $x_2 = 39.15$ m:

$$\frac{0.149175 \text{ m} - 0.145 \text{ m}}{0.15 \text{ m} - 0.145 \text{ m}} = 0.835$$

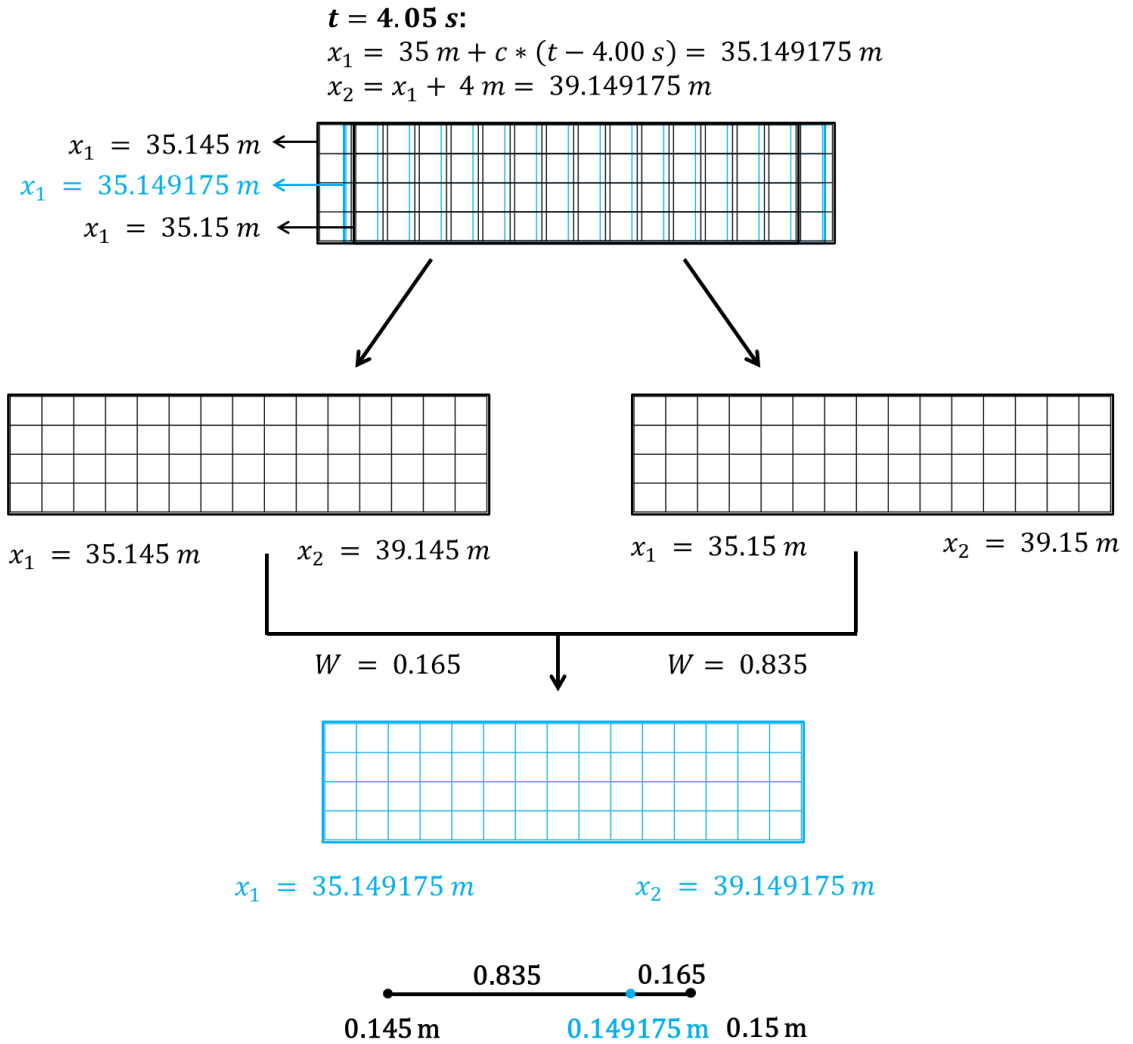


Figure 26. Illustration of the weighted algorithm at $t = 4.05 \text{ s}$ for $c = 2.9835 \text{ m/s}$ and uniform grid of $\Delta x = 0.005 \text{ m}$. The boundaries of the ensemble box are located at $x_1 = 35 \text{ m}$ and $x_2 = 39 \text{ m}$ at $t = 4.00 \text{ s}$. The weighted factors, W , are calculated based on the vicinity of the shifted domain to the nearest grid point.

3.4 Subgrid Scale Resolution

Energy cascade happens during the LES modelling where turbulent kinetic energy (TKE) dissipates in the descending order of scales. At the tiny scales, where SGS viscosity controls, the dissipation stops and TKE becomes internal energy (Li et al., 2020). One of the primary functions of a LES model is to dissipate the energy from the resolved scales at an appropriate rate. In the Smagorinsky model, the SGS viscosity is directly proportional to the strain rate (Smagorinsky, 1963):

$$\mu_t = \rho(C_s\Delta)^2(2S_{ij}S_{ij})^{1/2} \quad \text{Eq. 48}$$

where μ_t is SGS viscosity, C_s is Smagorinsky constant, and S_{ij} is strain rate. Therefore, the model performs poorly in shear-driven flows, where the strain rate, S_{ij} is large due to the initial condition. In near-wall on the other hand, the majority of the energy containing eddies are smaller than the filter size, which leads again to poor performance of the model. A similar limitation close to the boundary, where the subgrid scale viscosity, μ_t , dominates. As a result, k -equation model is selected instead of the Smagorinsky model.

In order to justify the mesh size that is applied in the simulation to be effective and lead to high-quality results, the percentage of TKE that is solved, k_p , is defined and presented in the domain. The selection of filter size is a critical issue around LES, and it should be able to resolve the majority of large-scale energy-containing eddies. Pope (2001) provided a popular approach to evaluate the LES simulation quality, who suggested that the resolved TKE, denoted by k_{res} was expected to be greater than 80% of total TKE in a

high quality simulation. Matheou and Chung (2014), on the other hand, suggested the ratio to be more than 90%.

The equation to calculate the percentage of resolved turbulent kinetic energy, k_p , is:

$$k_p = \frac{k_{res}}{k_{res} + k_{SGS}} \quad Eq. 49$$

Subgrid scale TKE, k_{SGS} , is modelled with Equation 19, which is a direct output from the simulation since k -equation SGS model is used. k_{res} also known as the energy in larger than scale turbulence and is defined as:

$$k_{res} = \frac{1}{2} (\overline{u'u'} + \overline{v'v'} + \overline{w'w'}) \quad Eq. 50$$

where u' , v' , and w' are the resolved perturbation components in x, y, and z directions, respectively. Furthermore, $\overline{u'u'}$, $\overline{v'v'}$, and $\overline{w'w'}$ are the normal stresses in the Reynolds stress tensor:

$$R_{ij} = -\rho \begin{bmatrix} \overline{u'u'} & \overline{u'v'} & \overline{u'w'} \\ \overline{v'u'} & \overline{v'v'} & \overline{v'w'} \\ \overline{w'u'} & \overline{w'v'} & \overline{w'w'} \end{bmatrix} \quad Eq. 51$$

The free surface is also delineated at $\alpha_w = 0.5$ based on the VOF method. Splash and separation are not accounted for, in delineating the free surface shown in Figure 27 in black. Firstly, the simulation was performed with refinement over AR1 in Figure 15 for $Fr_s = 1.71$ and 2.13. The time and z averaged k_p fields are shown in Figure 27 with h normalized by surge wave height d_2 and $(x - ct)/d_1$ is the x coordinates shifted to $t = 0$ s and with gate location as the origin normalized by downstream water depth, d_1 .

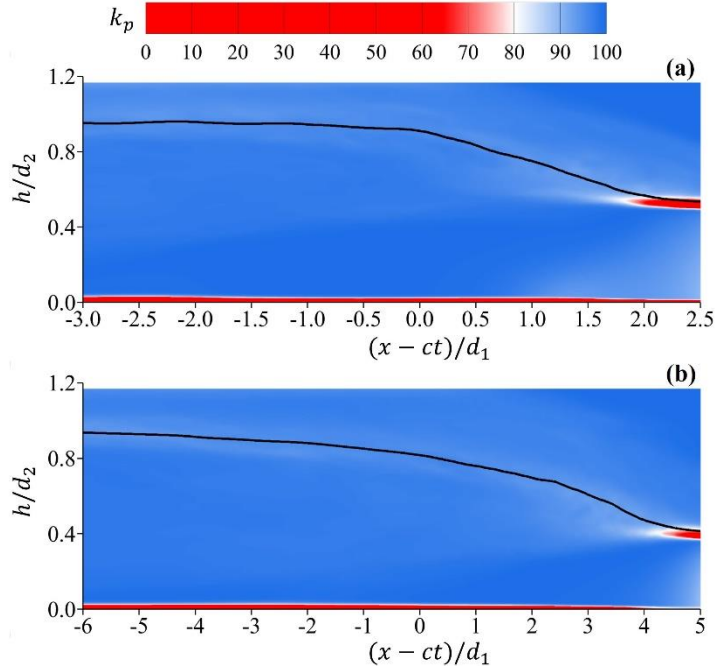


Figure 27. k_p at Fr_s of (a) 1.71, (b) 2.13 without toe refinement of AR2.

As shown in Figure 27, for both Froude numbers, $Fr_s = 1.71$ and 2.13 , a large area of red presents near the toe. According to the scale, the k_p , 80% threshold is indicated as white colour, smaller than 80% is indicated as red colour and greater than 80% is indicated as blue colour. Therefore, the surge toe area is not resolved well compared to the rest of the domain. A second level refinement is applied near the toe, AR2 in Figure 15, which has the h covers $d_1 \pm 0.05$ m. The second level refinement results are presented in Figures 28, 29 and 30. Figures 28(a), 29(a) and 30(a) show larger than scale TKE, k_{res} , for $Fr_s = 1.71$, 2.13 and 2.49 , respectively. Higher values in these plots are observed around the surge front in both air and water, but it also spreads in depth and extends between surge heel and toe. Furthermore, k_{res} peaks in the vicinity of the surge toe for three Froude

numbers. Existing laboratory experiments (Koch and Chanson, 2009; Leng and Chanson, 2016) have also shown a sharp rise in the normal Reynolds stresses, $\overline{u'u'}$ and $\overline{v'v'}$ as components of TKE, near the toe. Figures 28(b), 29(b) and 30(b), on the other hand, those are the plots of instantaneous subgrid scale TKE, k_{SGS} , the darker colours are concentrated around the toe and around the surge front. Due to higher k_{SGS} around the toe, the ratio of resolved to total TKE is at the lowest value of about 86% in this area. However, this ratio remains above the recommended value for LES (Pope, 2001).

In the surge, the ratio of k_p remains consistently above 90%. This indicates that the LES model resolves mostly 90% of the TKE. This is achieved by designing two areas of refinement, in the surge propagation area (AR1) and further refinement across the toe (AR2), where shear layer is formed. Although the overall TKE is small and mainly concentrates near the surge toe, velocity gradient at the surge toe is one of the primary reasons causes the instability.

Therefore, it is important to refine the mesh around this particular area in order to fully understand the turbulent characteristics of the flow. The k_{SGS} transport equation does not treat the near-wall nor the near-wall region is refined to resolve the very small scales. Therefore, this area has very low k_p . However, as shown in the later sections, the lower envelope of mixing in the breaking surge is not affected by the near-wall region, and therefore, this does not impact the development of turbulent structures in the vicinity of surge front.

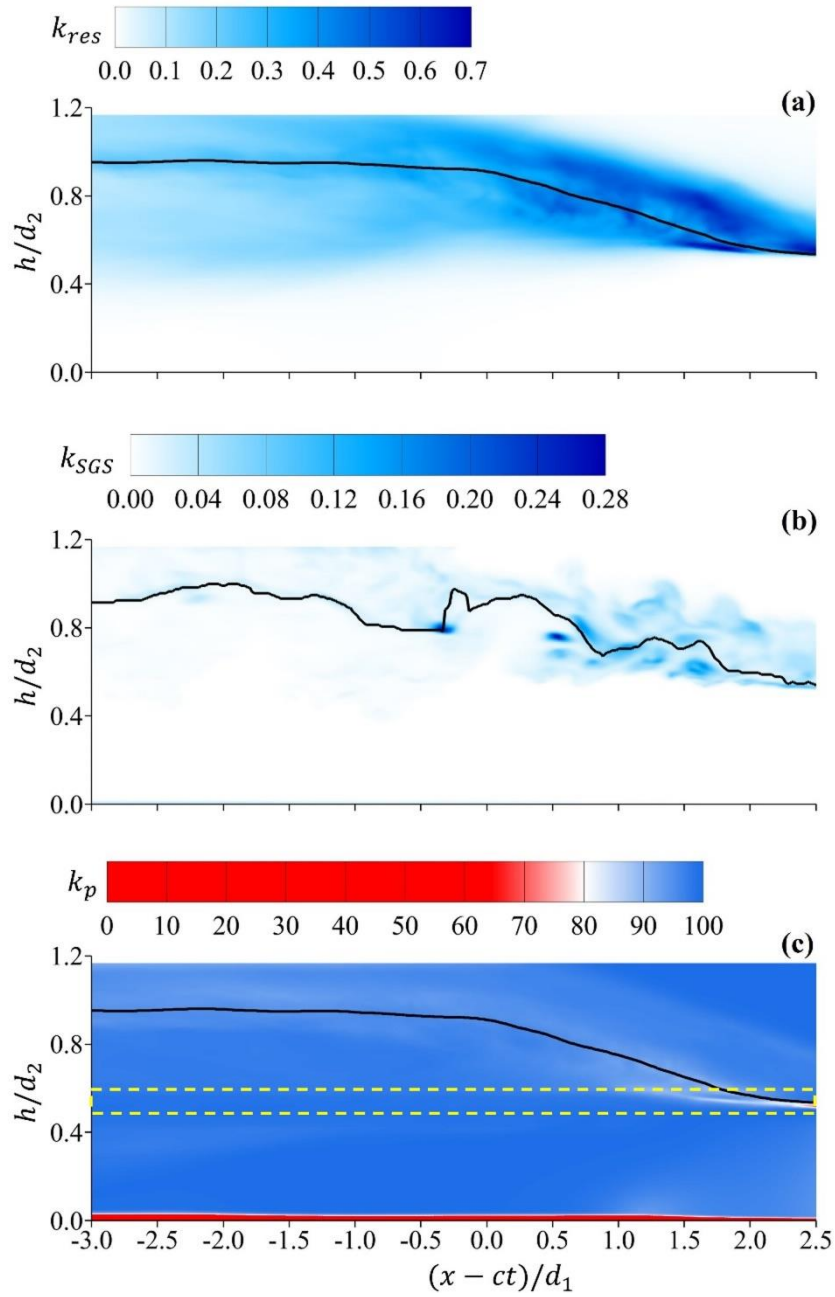


Figure 28. Plots of (a) time and z-averaged k_{res} ; (b) k_{SGS} at $t = 4.2$ s and $z = 0.02$ m; (c) time and z-averaged k_p with 80% as the threshold for case#1 with $Fr_s = 1.71$. Water surface is shown as the black line. Yellow box outlines AR2.

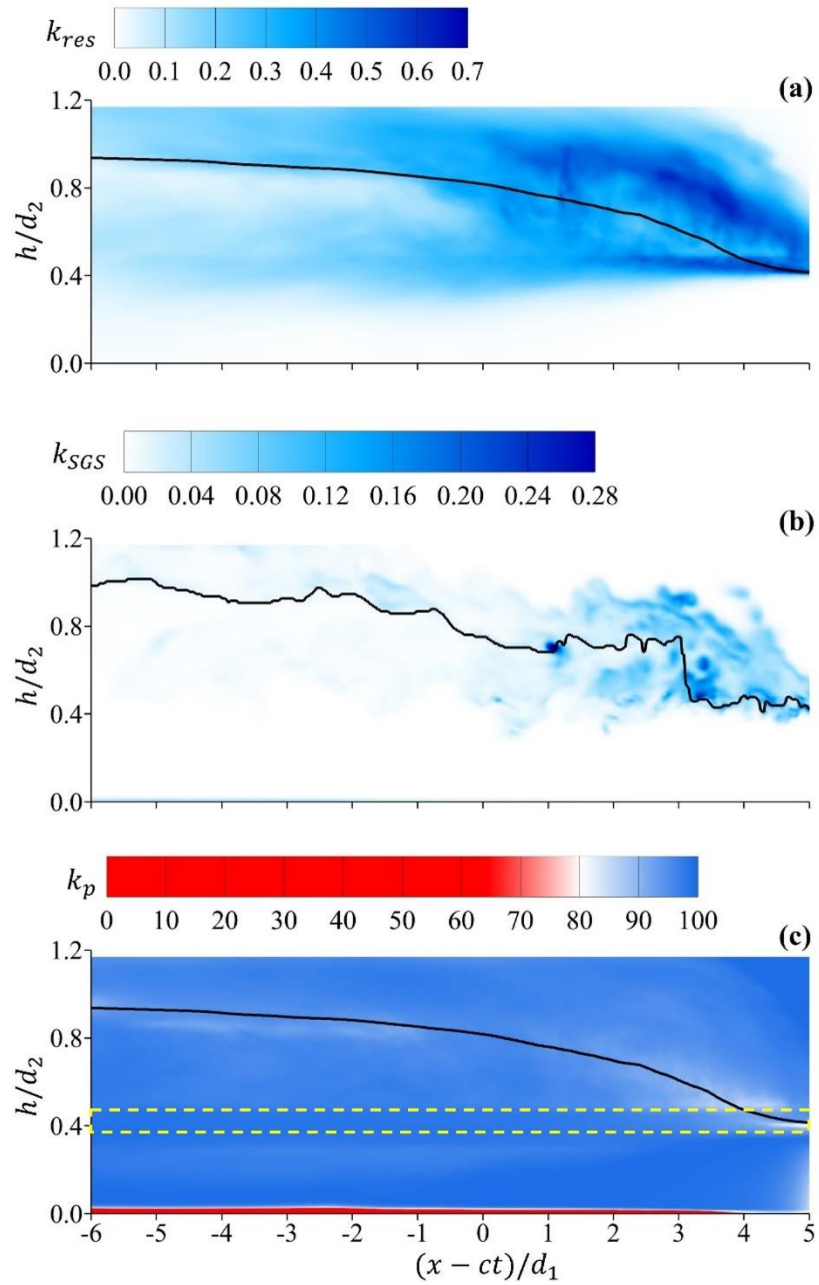


Figure 29. Plots of (a) time and z-averaged k_{res} ; (b) k_{SGS} at $t = 4.2$ s and $z = 0.02$ m; (c) time and z-averaged k_p with 80% as the threshold for case#2-3 with $Fr_s = 2.13$.

Water surface is shown as the black line. Yellow box outlines AR2.

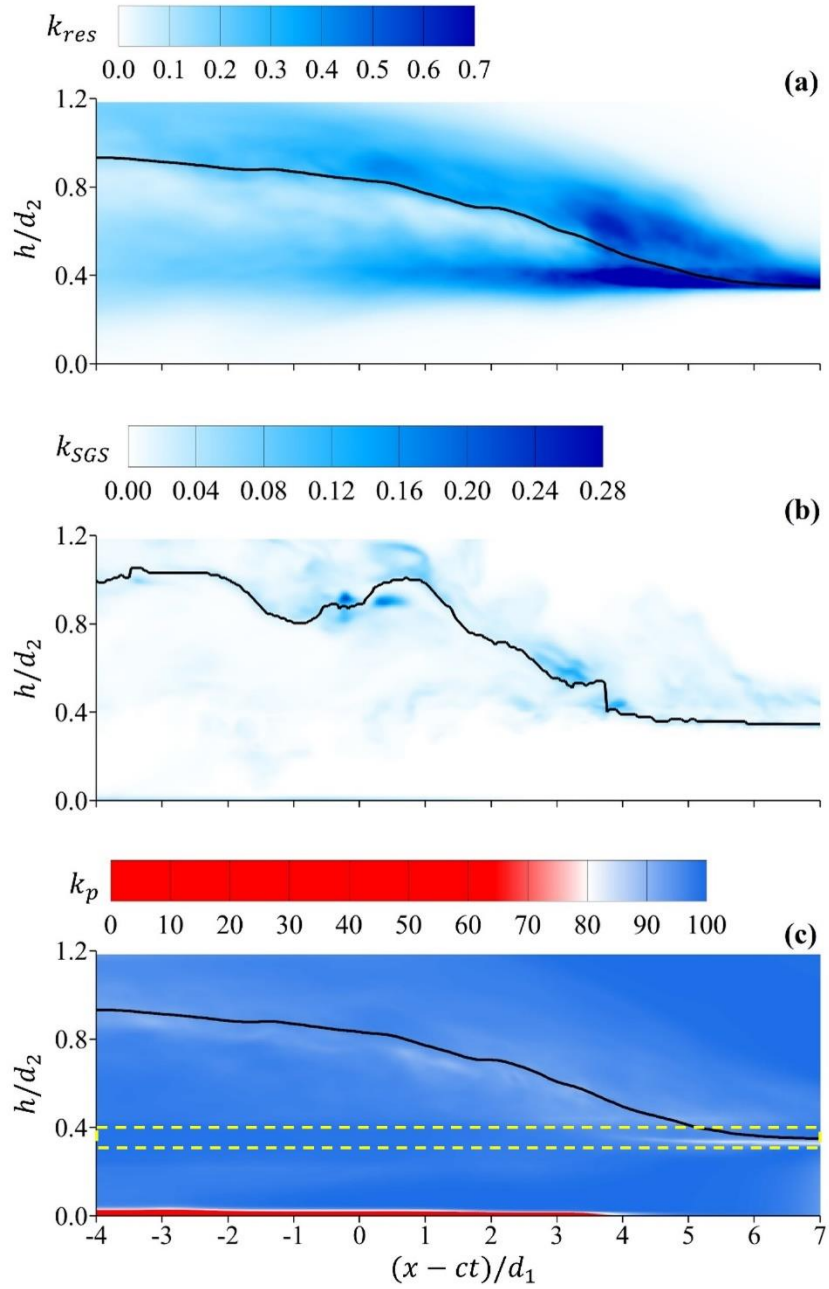


Figure 30. Plots of (a) time and z-averaged k_{res} ; (b) k_{SGS} at $t = 4.2$ s and $z = 0.02$ m; (c) time and z-averaged k_p with 80% as the threshold for case#3 with $Fr_s = 2.49$. Water surface is shown as the black line. Yellow box outlines AR2.

3.5 Water Depth Perturbations

Figures 32(a), 33(a) and 34(a) show the instantaneous water surface profiles, all shown in grey, and the averaged water surface profile in blue. Both are normalized with respect to surge wave height, d_2 , obtained from MOC. Since the averaged water depth changes in the x-direction, this spatially varied averaged water depth is used for normalization.

Water surface perturbation is defined as $h' = h - \bar{h}$. The magnitude of the normalized h' has the expression of $\overline{h'^2}/\bar{h}^2$. In terms of the root mean square (rms), which is defined as:

$$rms = \sqrt{\frac{1}{n} \sum_i h'^2} \quad Eq. 52$$

where n is the amount of data points which will be 100 since there are 100 time instances included in the calculation; h'^2 for the magnitude of water surface perturbation. Thus,

$$\frac{\overline{h'^2}}{\bar{h}^2} = \frac{h'_{rms}{}^2}{\bar{h}^2} \quad Eq. 53$$

which is plotted in Figures 32(b), 33(b) and 34(b) for $Fr_s = 1.71, 2.13$ and 2.49 . The normalized water surface perturbation peaks at $\frac{h'_{rms}{}^2}{\bar{h}^2} = 0.008$ for $Fr_s = 1.71$, at 0.011 for higher Froude number of $Fr_s = 2.13$, and can reach 0.022 for $Fr_s = 2.49$.

Leng and Chanson (2016) summarized several experimental works of both surge wave and hydraulic jump studies about the relation between the Froude number, Fr_s , and the maximum water depth perturbations, h'_{max} . In general, h'_{max} increases with Fr_s , and

maximum water depth perturbation in present study followed the same trend from $Fr_s = 1.71$ to 2.49 . In all three cases, this peak was observed immediately behind the toe.

Higher moments of perturbation, skewness, S_ϕ , and kurtosis, K_ϕ provide deeper insight into the distribution of perturbation and ultimately the physics of the flow. The skewness is the third moment and kurtosis is the fourth moment of perturbation of parameter ϕ , where ϕ can be velocity components, pressure, and water depth, and are defined as:

$$S_\phi = \overline{(\phi'^3)} / \left(\overline{(\phi'^2)} \right)^{\frac{3}{2}} \quad Eq. 54$$

$$K_\phi = \overline{(\phi'^4)} / \left(\overline{(\phi'^2)} \right)^2 \quad Eq. 55$$

The skewness reveals information about the asymmetry of the perturbation, while kurtosis provides information on the flatness of perturbation distribution or their distribution around mean perturbation value. Skewness for a Gaussian distribution is around 0 and a positive skewness means that the perturbation is more likely to take on large positive values than large negative values.

On the other hand, kurtosis for a Gaussian distribution is around 3. Perturbation and measurements leading to kurtosis lower than this value, are mainly clustered around the mean, where perturbation measurements dominated by intermittent extreme events have higher kurtosis.

Around the heel, the depth skewness remains around 0 for three Froude numbers as shown in Figures 32(c), 33(c) and 34(c). However, moving from heel towards the toe, the

skewness starts to rise and reaching as high as 2.0 for $Fr_s = 1.71$ and 2.5 for $Fr_s = 2.13$ and 2.49 around the toe.

This shows the tendency for water surface profile perturbation to experience extreme positive fluctuations. The water surface kurtosis profiles for three Froude numbers exhibit the same behaviour, as shown in Figures 32(d), 33(d), 34(d). In the vicinity of the heel, kurtosis remains at about 3, however, rises to above 3, close to the toe. This confirms that around the toe, flow mainly comprises intermittent extreme water depth perturbations.

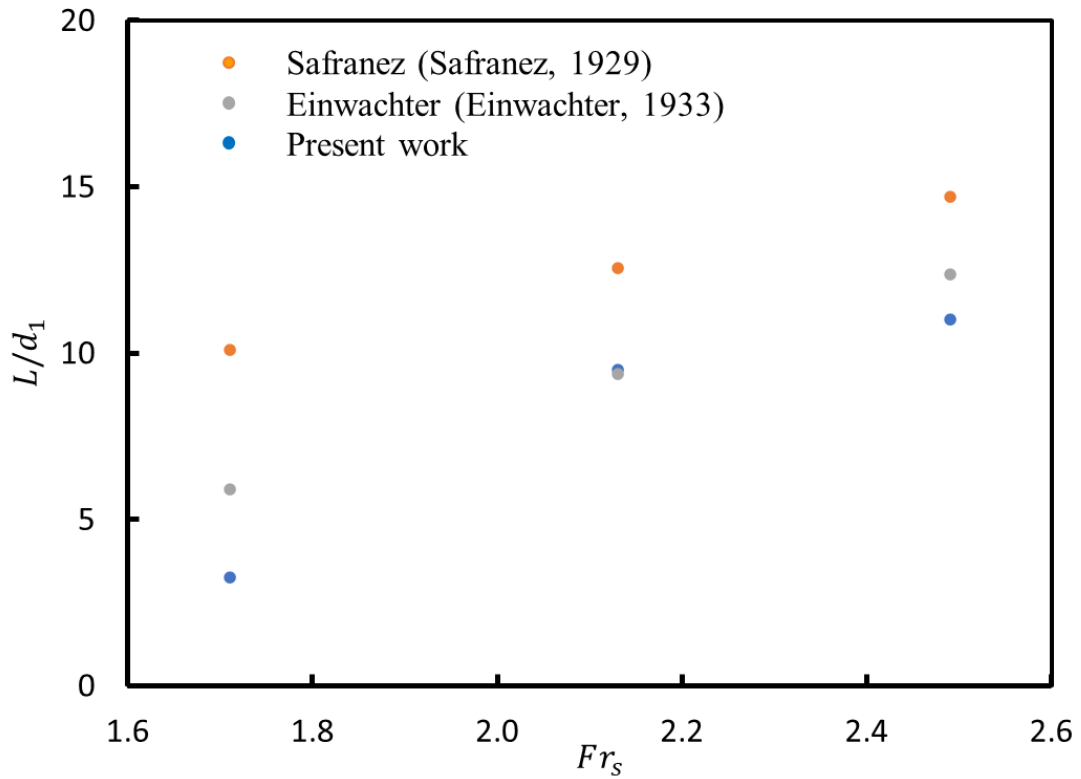


Figure 31. Plot of L/d_1 against Fr_s , where L is the surge length.

The surge lengths L/d_1 are identified and measured for three Froude numbers in Figures 32(a), 33(a) and 34(a). Two analytical methods to calculate hydraulic jump length noted by Mundo-Molina and Pérez (2019) are plotted together with the current simulation in Figure 31. They are:

Safranez (Safranez, 1929):

$$\frac{L}{d_1} = 5.9 * Fr_s \quad Eq. 56$$

Einwachter (Einwachter, 1933):

$$\frac{L}{d_1} = 8.3 * (Fr_s - 1) \quad Eq. 57$$

As shown in Figure 31, the general Fr_s vs. L/d_1 trend for present work agrees with the other two analytical methods, which is the normalized surge length increases as Froude number increases. Safranez's surge lengths are all greater than the simulation surge lengths. For Einwachter, the data points are closer to the current simulation's, especially at $Fr_s = 2.13$, two data points meet at the same location.

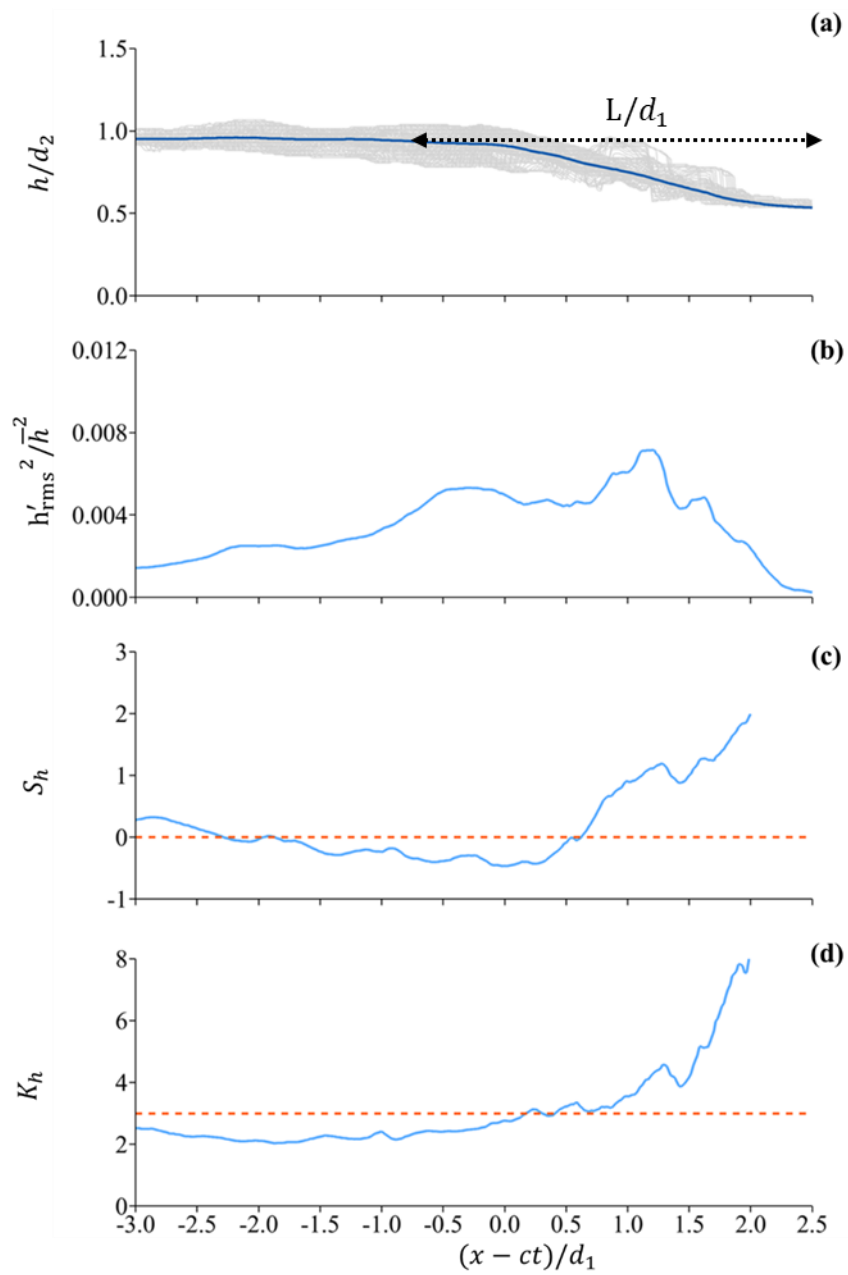


Figure 32. Normalized water surface perturbation analysis: (a) time and z-averaged wave surface (blue line), \bar{h} and instantaneous profiles, h ; (b) Squared rms of h' , $h' = h - \bar{h}$; (c) skewness of h , S_h ; (d) Kurtosis of h , K_h for case#1 with $Fr_s = 1.71$.

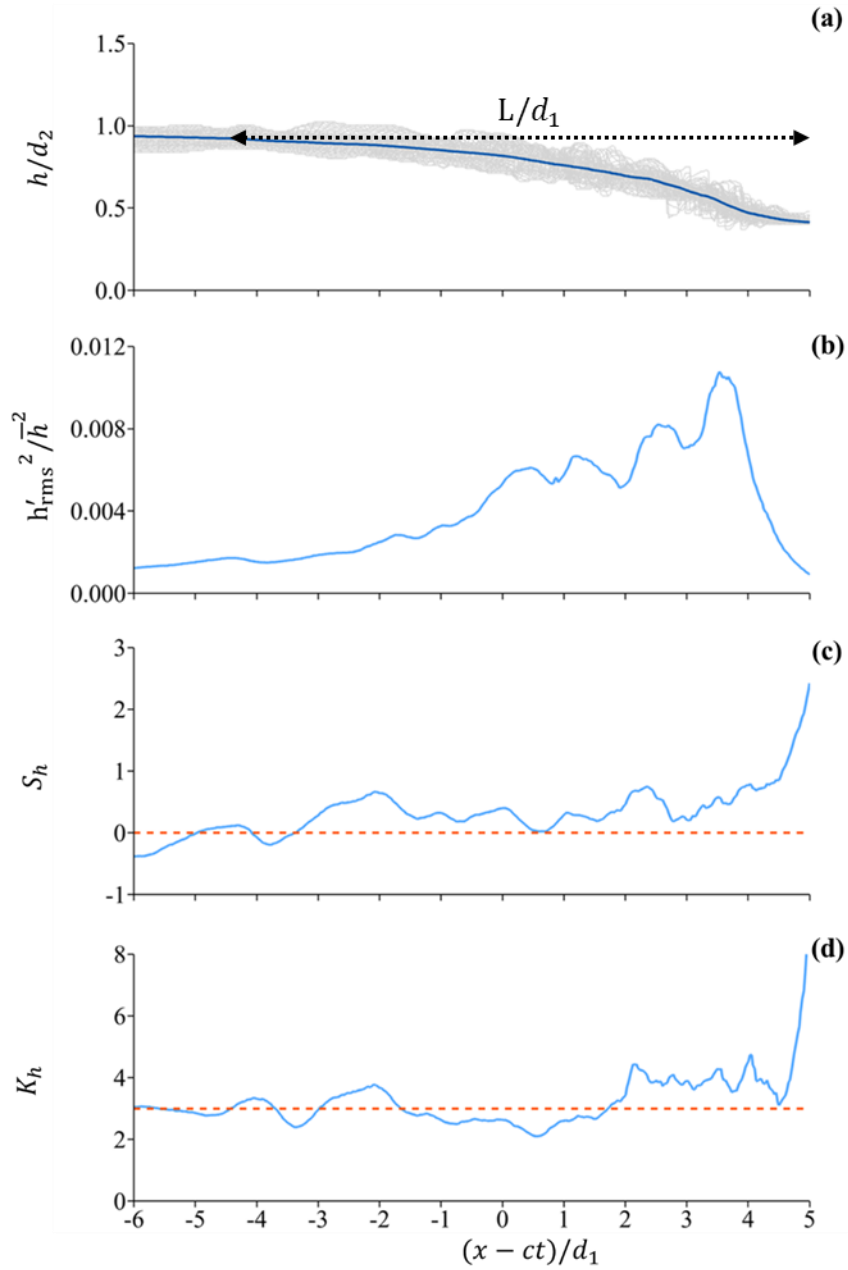


Figure 33. Normalized water surface perturbation analysis: (a) time and z-averaged wave surface (blue line), \bar{h} and instantaneous profiles, h ; (b) Squared rms of h' , $h' = h - \bar{h}$; (c) skewness of h , S_h ; (d) Kurtosis of h , K_h for case#2-3 with $Fr_s = 2.13$.

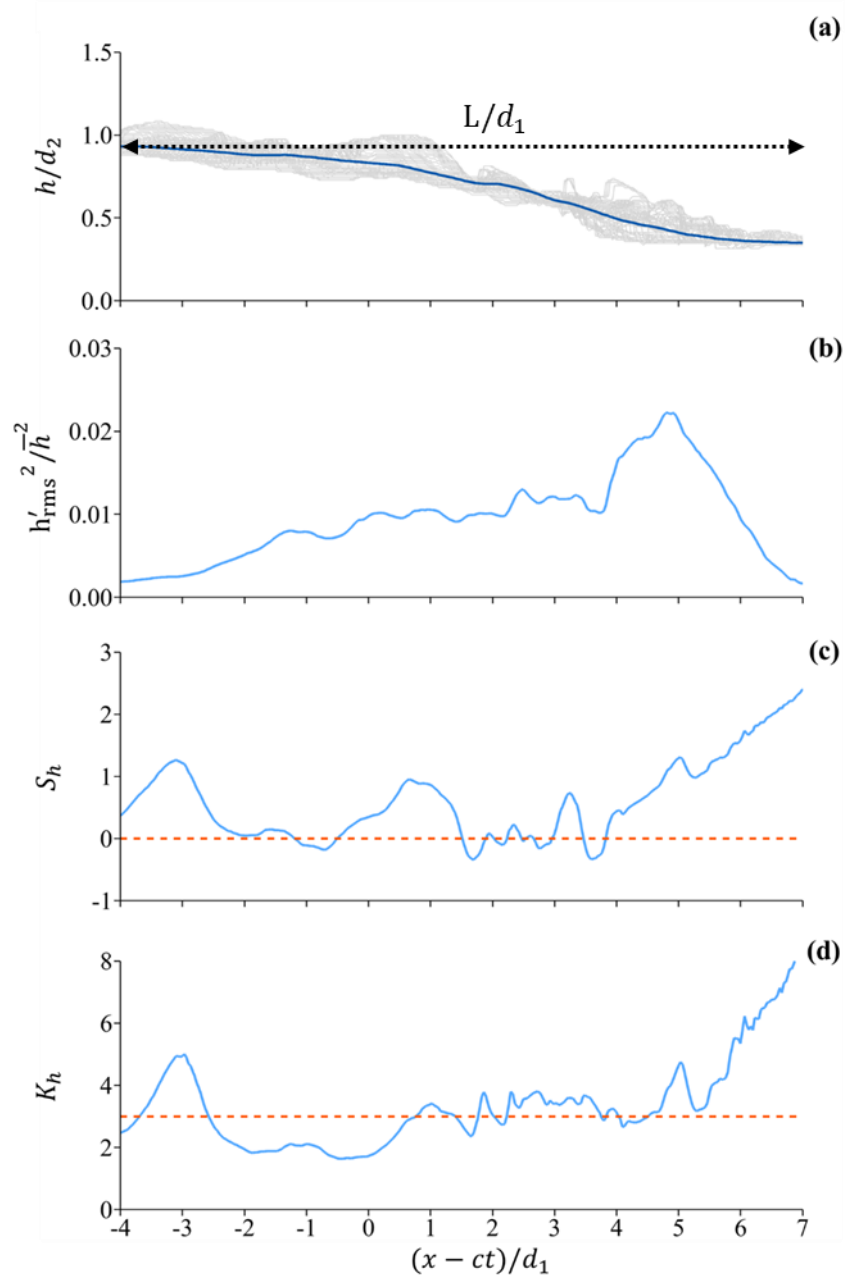


Figure 34. Normalized water surface perturbation analysis: (a) time and z-averaged wave surface (blue line), \bar{h} and instantaneous profiles, h ; (b) Squared rms of h' , $h' = h - \bar{h}$; (c) skewness of h , S_h ; (d) Kurtosis of h , K_h for case#3 with $Fr_s = 2.49$.

3.6 Air Entrainment Profiles and Mixing Cones

Two mechanisms are identified in the literature that contribute to the instability and development of highly turbulent front in a surge wave. These are the advective-diffusion region and the breaking front (Takahashi and Ohtsu, 2017). The first instability is induced by the velocity gradient at the surge toe (Karimpour and Chu, 2019), and the second by the phase discontinuity at the surge front. The formation of this breaking region is independent of the inflow conditions and is dependant on the surge height (Rajaratnam, 1967).

Figures 35(a)(b), 36(a)(b), 37(a)(b) are plots of instantaneous air concentration distribution. The orange lines in these profiles delineate the marginal zero value for eddy viscosity, $\nu_t = \frac{\mu_t}{\rho} = 0.00001 \text{ m}^2/\text{s}$. Along with the water surface profiles, these lines provide an envelope where the velocity perturbations are contained. In Figures 35(c), 36(c) and 37(c), the averaged air concentration and the upper and lower envelopes, y_s and y_b , are plotted for $Fr_s = 1.71, 2.13$ and 2.49 . The averaged lower envelope of air entrainment, y_b , is plotted using both eddy viscosity and $\alpha_a = 0.5$. Both methods yield similar lower envelopes for three Froude numbers. Furthermore, the instantaneous and averaged lower envelopes demonstrate the proximity of the shear layer to the rigid bed. In all cases, this lower envelope is developed at a depth, where the impact of the boundary layer is not present. This is evidently indicating that lower k_p values for near the boundary region, shown in Figures 28, 29 and 30, have no effect on the development of the turbulent region across the surge front, between surge toe and the heel.

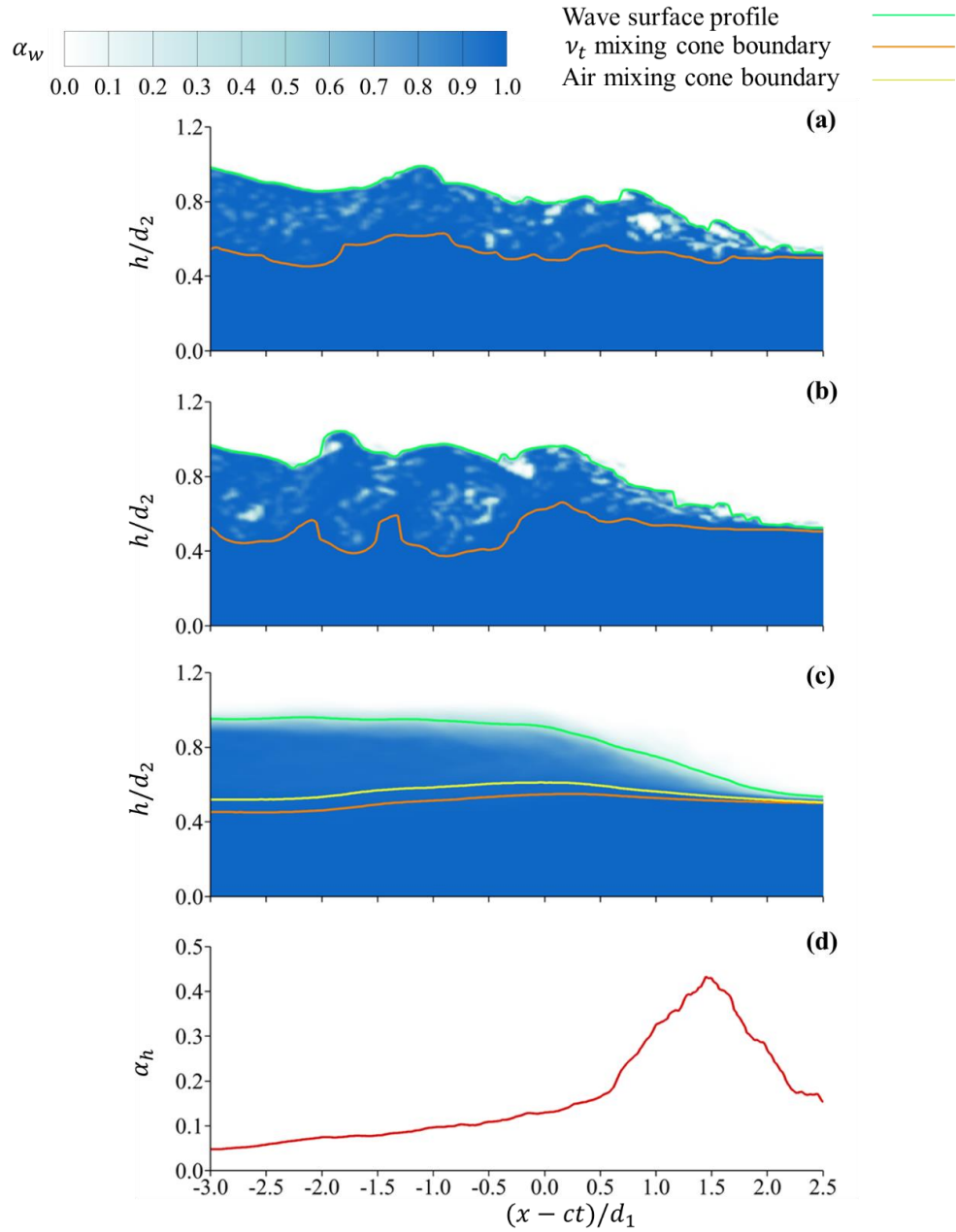


Figure 35. Normalized wave surface, v_t mixing cone boundary, air mixing cone boundary plots of (a) at $t = 4.0$ s, $z = 0.2$ m; (b) at $t = 4.5$ s, $z = 0.2$ m; (c) time and z-averaged; (d) α_h for case#1 with $Fr_s = 1.71$.

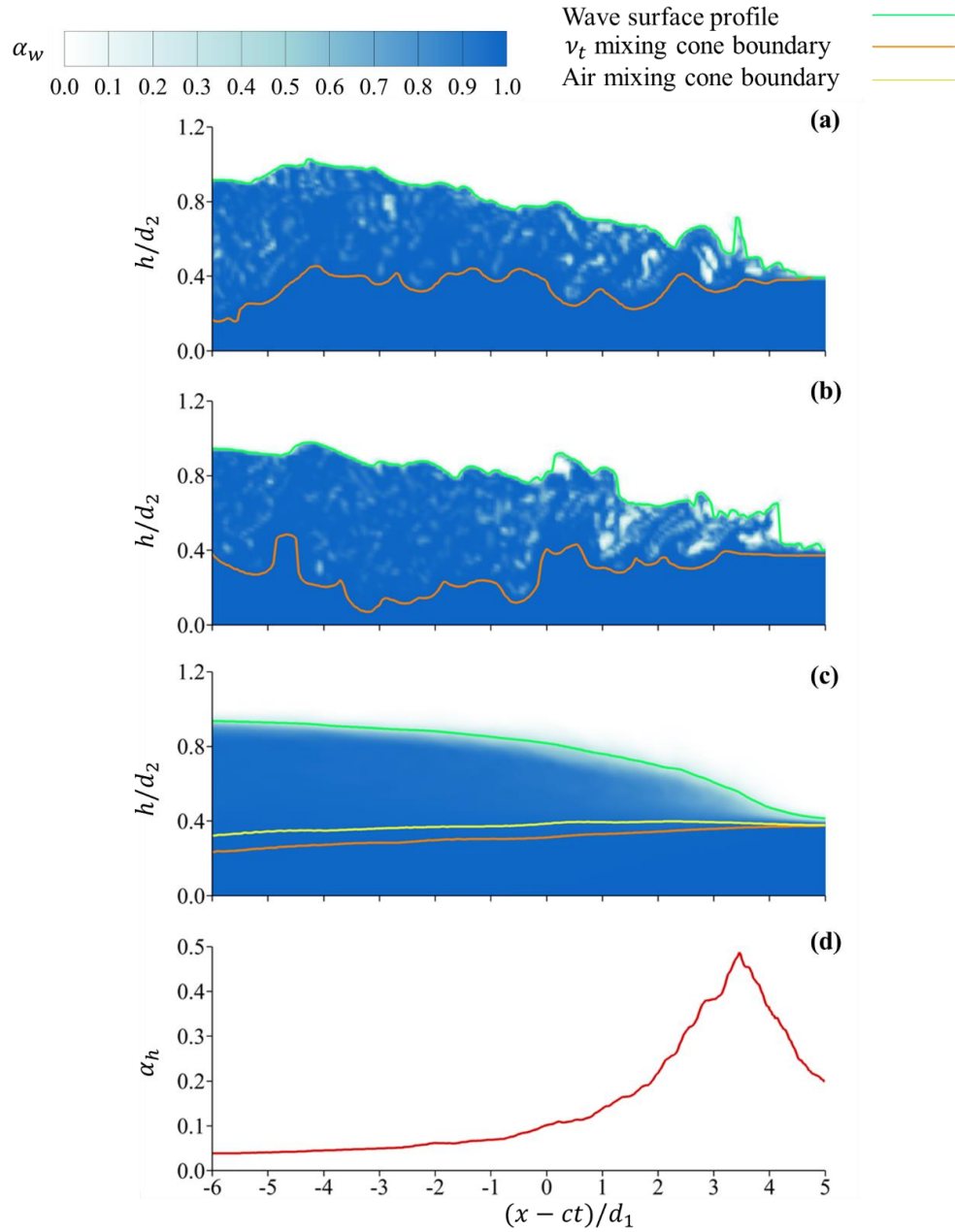


Figure 36. Normalized wave surface, v_t mixing cone boundary, air mixing cone boundary plots of (a) at $t = 4.0$ s, $z = 0.2$ m; (b) at $t = 4.5$ s, $z = 0.2$ m; (c) time and z-averaged; (d) α_h for case#2-3 with $Fr_s = 2.13$.

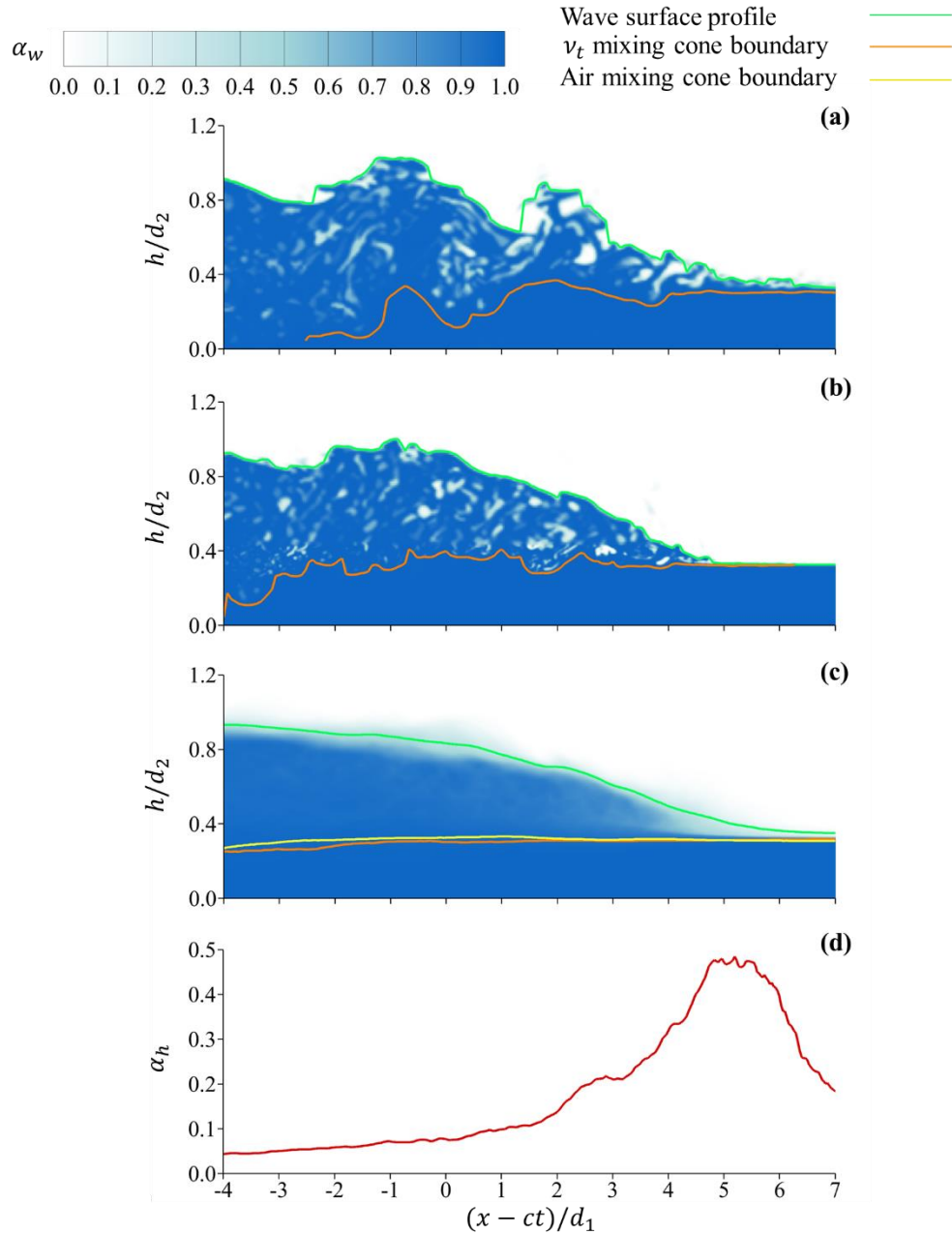


Figure 37. Normalized wave surface, v_t mixing cone boundary, air mixing cone boundary plots of (a) at $t = 4.0$ s, $z = 0.2$ m; (b) at $t = 4.5$ s, $z = 0.2$ m; (c) time and z -averaged; (d) α_h for case#3 with $Fr_s = 2.49$.

Instantaneous and averaged upper and lower bounds, as well as the air concentration contours, indicate the extent of air entrainment grows with Froude number, which has been previously reported by Wüthrich et al. (2020). To quantify the air entrainment across the surge wave, average air concentration, α_h , is defined between the free-surface profile at y_s and the lower boundary of mixing cone in the advective-diffusion region denoted by y_b :

$$\alpha_h = \frac{\sum_{y_b}^{y_s} \alpha_a}{\sum_{y_b}^{y_s} \alpha_w} \quad \text{Eq. 58}$$

The peak value for average air concentration, α_h shown in Figure 36(d), occurs at $x - ct = 3.4d_1$ for $Fr_s = 2.13$, which coincides with the peak of surface perturbation plotted in Figure 33(b). This is supported by the plot of k_{res} for this Froude number in Figure 29(a). The area of high larger than scale perturbation in Figure 29(a), intersects with the free surface right behind the toe, leading to substantial level of air entrainment near the toe. However, the contour implies that the area with intense resolved TKE, k_{res} , deviates from the free-surface moving upstream away from the toe. This plot also demonstrates that the intensity of the resolved TKE reduces behind the toe. Both phenomena combined, lead to rapid induction of air entrainment close to the toe, and subsequently reduction in air entrainment, moving further upstream. A similar pattern is observed for $Fr_s = 1.71$ and 2.49. Three α_h plots for three Fr_s exhibit similar maximum which can be attributed to the similar surge height of about 0.3 m for the 3 cases. As most of the air entrainment exist behind the surge front, therefore, coinciding area behind the surge lead to similar α_h plots.

Chanson (2003) has conducted laboratory experiments to study air entrainment in surge waves by generating dam-break wave. They have reported very high air concentration ratio near the toe which agrees with observation in the present study for α_h . As shown in Figure 3, for the region near the surge toe which was 0-70 mm, Chanson (2003) reported a peak depth averaged air entrainment of 0.77 in the experiment. As moving towards upstream, the depth averaged air entrainment decreased as well. This trend of reducing air entrainment from toe to upstream coincides with the trend of α_h for the three Froude numbers in present simulations. Air concentration, α_a , is also plotted against vertical coordinate at multiple locations between surge toe and heel in Figure 38. Here, three instantaneous profiles as well as the averaged profiles are plotted. The air concentration pattern in depth in shear layer and breaking region is reported in literature for hydraulic jumps (Takahashi and Ohtsu, 2017; Wang and Chanson, 2015). The air parcels at the toe are advected and diffused in the shear layer. The instantaneous profiles often peak at the depth of the shear layer, for instance for $h/d_2 = 0.42$ at $(x - ct)/d_1 = 3.505$, Figure 38(c), and $h/d_2 = 0.48$ at $(x - ct)/d_1 = 0.2505$, Figure 38(b), for $t = 4.25$ s. While this trend is not observed at all times, the averaged profiles also seem to peak where the shear layer forms. The position of this local maximum occurs at slightly higher depths as the profiles move away from the toe, which is consistent with data reported by Wang and Chanson (2015). Afterwards, α_a grows with the depth and reaches one at the free surface. This demonstrates the importance of the TKE across the shear layer in air entrainment and air distribution, as observed in Figures 35(d), 36(d) and 37(d).

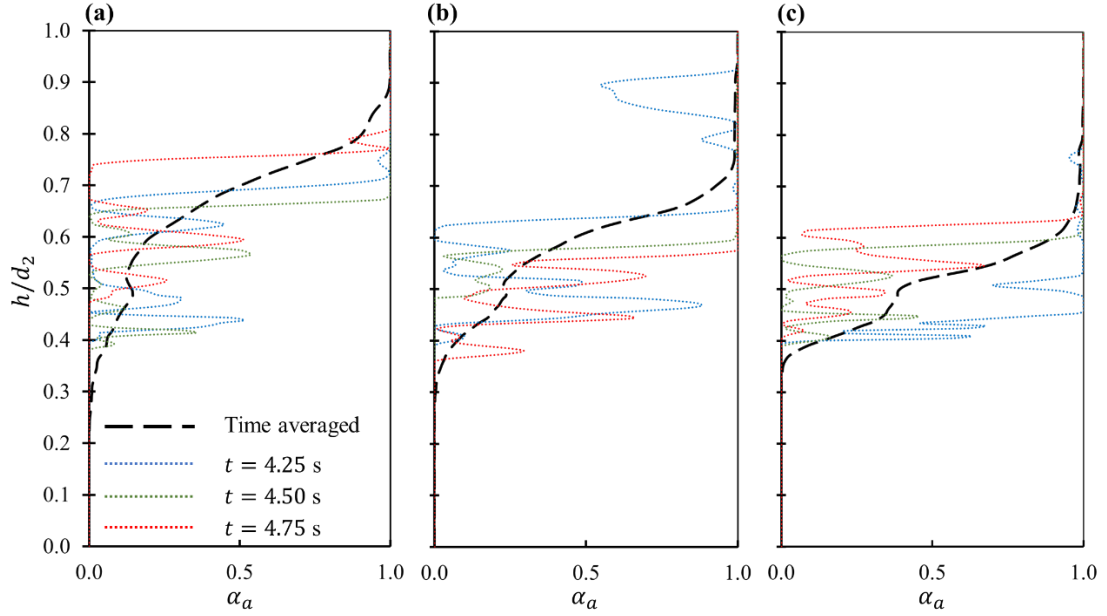


Figure 38. Plots of instantaneous α_a against h/d_2 for $t = 4.25$ s, 4.50 s, 4.75 s, and averaged α_a at $(x - ct)/d_1$ is (a) 1.505 ; (b) 2.505 and (c) 3.505 for $Fr_s = 2.13$.

3.7 Velocity Perturbation and Quadrant Analysis

To quantify the turbulent structures behind breaking surge waves, the instantaneous perturbations are extracted and plotted in Figures 39 and 40. These plots are produced at two depths: at $y = d_1$ for points located behind the surge toe and those located at the midpoint of surge height, $y = d_1 + 0.5(d_2 - d_1)$. Standard Deviational Ellipses (SDEs) are also plotted at 99% and 50%. SDEs delineate the spatial characteristics and distribution of perturbations. The orientation of the SDEs is such that its semi-axes align with the eigenvectors of the covariance matrix of the sample. The plotted SDEs approximate the regions containing 99% and 50% of the perturbations in each perturbation cloud. The quadrant analysis is one of the most conventional methods to identify the dominant

coherent structures in turbulent flow (Lu and Willmarth, 1973; Rajagopalan and Antonia, 1982). In order for us to assess the proper periodic domain size in the z -direction, this study has conducted the simulation for $Fr_s = 2.13$ for three domain sizes of $T = 10\Delta x, 20\Delta x,$ and $40\Delta x,$ in cases#2-1, 2-2, and 2-3, respectively. The plotted perturbations in Figure 39 in columns 1 to 3, represent the progression of perturbation as expanding the domain in the z -direction. As seen in the plot of v'/U_2 against w'/U_2 in $T = 10\Delta x$ at toe in Figures 39(b1), in this narrow domain the v'/U_2 is dominant over w'/U_2 . However, progressively as the domain was expanded, the SDEs got closer in shape to concentric circles, suggesting a comparable magnitude for v'/U_2 and w'/U_2 . From $T = 20\Delta x$ to $40\Delta x$ the impact of the domain width becomes negligible as shown in Figures 39(b2) and (b3). The structure of the perturbations becomes invariant to the domain width at $T = 40\Delta x$. This width, therefore, is selected to demonstrate the structure of perturbations in this thesis. Figures 23, 24 and 25 contain instantaneous plots of Q-criterion in the yz -plane. As evident there, the coherent structures are present in the yz -plane. The width of the domain, $T = 40\Delta x,$ as shown in all instances for three Froude numbers of $Fr_s = 1.71$ in Figure 23, $Fr_s = 2.13$ in Figure 24 and $Fr_s = 2.49$ in Figure 25 is significantly larger than the scale of eddies formed in the yz -plane. This ensures that domain size does not suppress the perturbation growth in the z -direction and therefore, fully-developed 3D structures are not suppressed.

The perturbations in the xy -plane at $y = d_1$ and $T = 40\Delta x,$ u'/U_2 and $v'/U_2,$ are plotted for $Fr_s = 1.71, 2.13$ and 2.49 in Figures 40(a) and 40(c), respectively. The 99%

and 50% confidence SDEs in three Froude numbers are inclined towards the second and the fourth quadrant. In quadrants#2 and 4, the product of perturbations in x and y directions, $u'v'$, is negative. This consequently leads to a positive production of TKE. The xy perturbation cloud is dominated by sweeps (demonstrated by perturbation in quadrant#4) and ejections (quadrant#2) (Lu and Willmarth, 1973). Similar pattern emerges in different depth across the surge height, as plotted for $y = d_1 + 0.5(d_2 - d_1)$ in Figure 40(c).

On the contrary, the yz perturbation cloud, illustrates a different pattern. Figures 40(b), 40(d) show even distribution of perturbation in all 4 quadrants. All 4 mechanisms of outward interactions (quadrant#1), sweeps (quadrant#2), inward interactions (quadrant#3), and ejections (quadrant#4) become equally significant. This indicates that overall product of perturbations in the yz -plane is zero, leading to no turbulent production. A similar trend appears at $y = d_1 + 0.5(d_2 - d_1)$, where the perturbation cloud for u'/U_2 versus v'/U_2 leans towards the second and fourth quadrants. Since the shear instability is in the xy -plane (the gradient of x-component of the velocity in y -direction) the vortices in the vicinity of the toe are expected to have a 2D structure. Similarly, the instability caused by depth discontinuity also occurs in the xy -plane (phase or depth gradient across the surge front in the x -component). Therefore, turbulence production is only observed in the xy -plane but not in the yz -plane from the velocity perturbations. The velocity perturbations in the z -direction, w' are critical for fully cascading turbulent flow and are comparable in size to the velocity perturbation component in the y -direction, v' , as demonstrated in Figures 40(b) and 40(d).

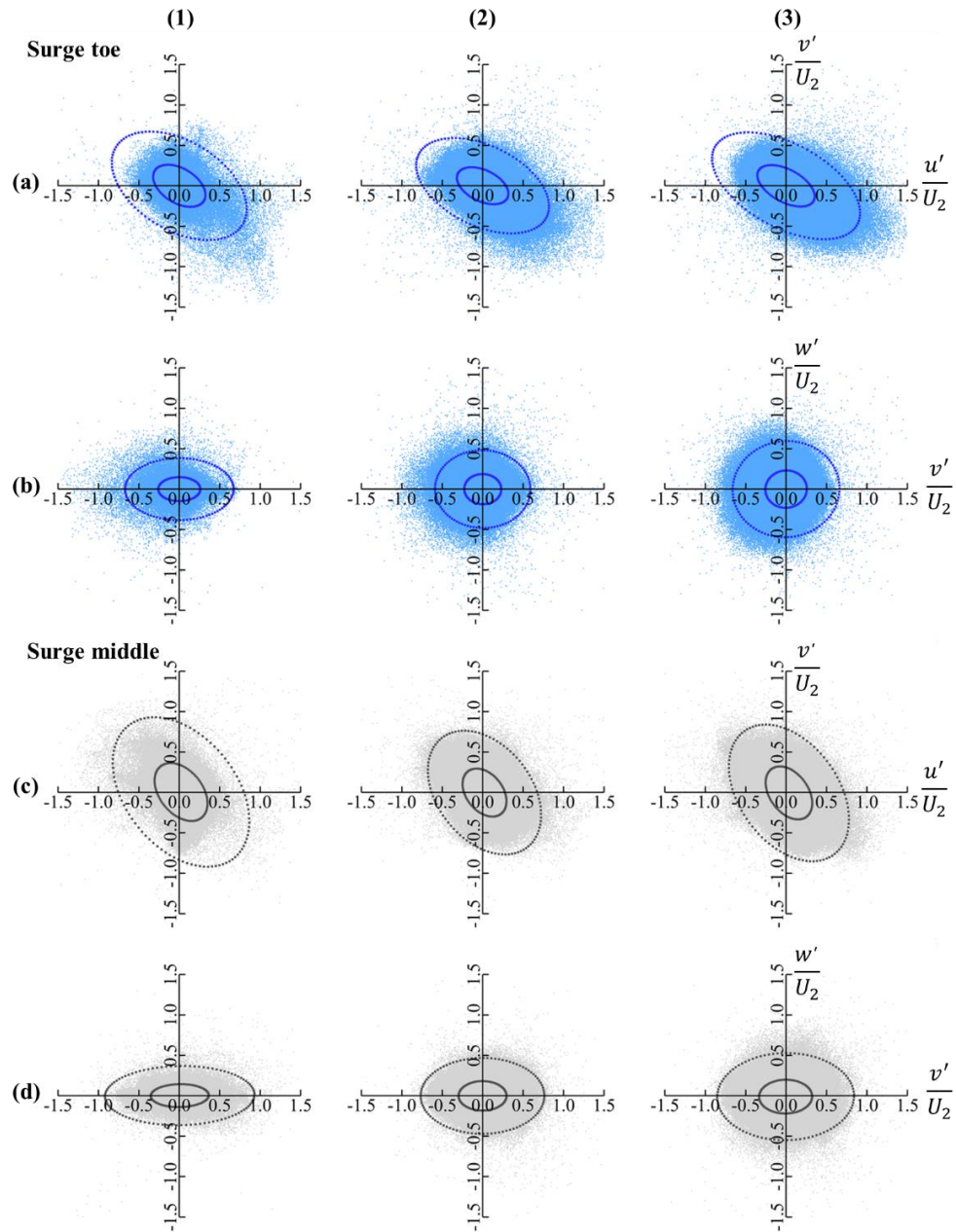


Figure 39. Velocity perturbation plots normalized by U_2 . (a) and (c) are u'/U_2 vs. v'/U_2 ; (b) and (d) are v'/U_2 vs. w'/U_2 at $y = d_1$ and $= d_1 + 0.5(d_2 - d_1)$, respectively. Column (1) is for case#2-1; column (2) for case#2-2 and column (3) for case#2-3.

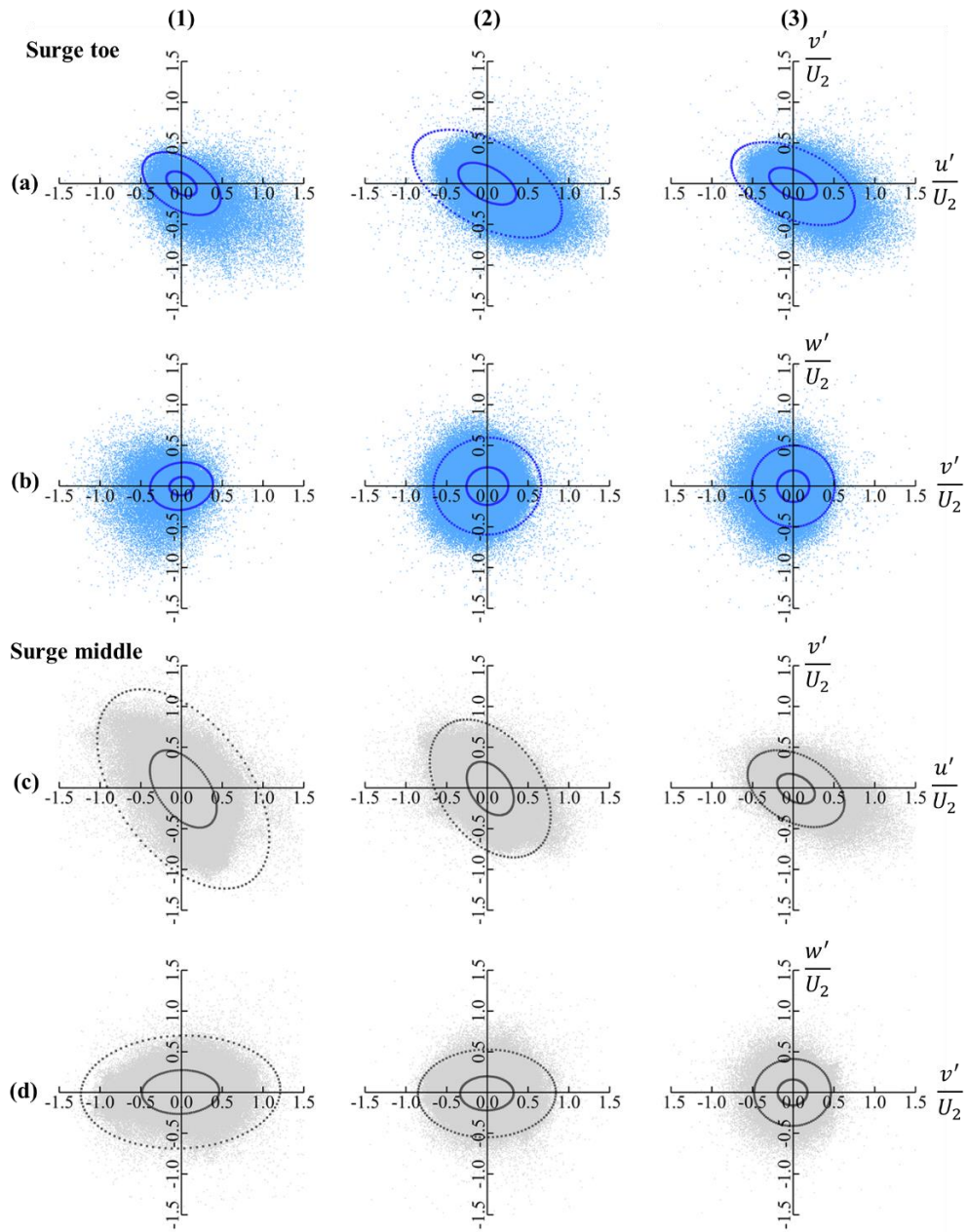


Figure 40. Velocity perturbation plots normalized by U_2 . (a) and (c) are u'/U_2 vs. v'/U_2 ;

(b) and (d) are v'/U_2 vs. w'/U_2 at $y = d_1$ and $= d_1 + 0.5(d_2 - d_1)$, respectively.

Column (1) is for case#1; column (2) for case#2-3 and column (3) for case#3.

3.8 Turbulence Anisotropy

The perturbation clouds have demonstrated the dominance of u' and v' in turbulent production. Plot of Q-Criterion has helped us visualize and investigate the structure of the vortices. However, this is a qualitative measure and cannot quantify turbulent structures. Reynolds stress usually can be utilized to quantify the turbulent structures. The shear and normal Reynolds stresses however is dependent on the choice of the coordinate system. The isotropic stress is to be $\frac{2}{3}k\delta_{ij}$. The anisotropic tensor is defined based on the Reynolds Stresses as:

$$a_{ij} = \frac{\overline{u'_i u'_j}}{2k} - \frac{\delta_{ij}}{3} \quad \text{Eq. 59}$$

$$k = \frac{\overline{u'_n u'_n}}{2} \quad \text{Eq. 60}$$

where δ_{ij} represents Kronecker delta, k is TKE. To present the 3D structure of turbulence in the surge wave, Lumley triangle can be utilized for anisotropic visualization, which is also known as an Anisotropy Invariant Map (AIM) (Emory and Iaccarino, 2014).

Therefore, the eigenvalues for the a_{ij} : $\lambda_1, \lambda_2, \lambda_3$ can be used to calculate a_{ij} invariants. In order to discover the 3D characteristics of turbulence with Lumley triangle, the following invariant needs to be determined from the eigenvalues (Choi and Lumley, 2001):

$$II = \frac{a_{ij}a_{ji}}{2} = \lambda_1^2 + \lambda_1\lambda_2 + \lambda_2^2 \quad \text{Eq. 61}$$

$$III = \frac{a_{ij}a_{jn}a_{ni}}{3} = -\lambda_1\lambda_2(\lambda_1 + \lambda_2) \quad Eq. 62$$

$$\xi^3 = \frac{III}{2} \quad Eq. 63$$

$$\eta^2 = \frac{II}{3} \quad Eq. 64$$

Three sides of the triangle demonstrate 1D (upper corner), 2D isotropic (left corner), and 3D isotropic flow. Sides demonstrate the range between these dimensional behaviours. For instance, moving from 1D towards the 3D corner, two components of the perturbation grow, until all perturbation components reach an equal magnitude. Between 2D isotropic and 3D isotropic, the 3rd perturbation grows. This is often demonstrated as a donut shape vortex, where the 3rd perturbation component is smaller than other two.

The second anisotropy analysis presented here is barycentric map. It is also developed as a function of eigenvalues.

$$x_B = C_{1c} + C_{3c} \frac{1}{2} \quad Eq. 65$$

$$y_B = C_{3c} \frac{\sqrt{3}}{2} \quad Eq. 66$$

where

$$C_{1c} = \lambda_1 - \lambda_2 \quad Eq. 67$$

$$C_{3c} = 3\lambda_3 + 1 \quad Eq. 68$$

The advantage of a barycentric map, is that equal visual representation is given to all limiting states.

This study has selected the data points across different heights of the surge front: $h = d_1$, $d_1 + \frac{1}{4}(d_2 - d_1)$, $d_1 + \frac{1}{2}(d_2 - d_1)$ and $d_1 + \frac{3}{4}(d_2 - d_1)$, for Froude numbers from 1.71 to 2.49. Figures below show the expecting turbulent structure when plotted with ξ vs. η and x_b vs. y_b invariants. The points close to the surge front (within 0.2 m to the front) are light colored and at further behind the front the points are darker colored.

Figure 41, 42, and 43 show the distribution of the anisotropy points at $Fr_s = 1.71$, 2.13, and 2.49, respectively. At a low Froude number of 1.71 most of the points at $h/d_2 = 0.520$ are concentrated to the right side of the Lumley triangle. This indicates that the perturbations at the toe start with a 1D structure. Moving away from the toe, other perturbation components grow and the overall turbulence are between the 1D turbulence and 3D isotropic turbulence, and with the cigar or also known as the rod shape. From the barycentric map, the points also tend to locate between 3D and 1D structure but not as close as in Lumley triangle. The observations of the turbulent structure at toe height are similar for the other two Froude numbers.

At higher depths, such as at the middle of surge height (grey), the perturbation close to the surge front is initiated somewhere near 3D and moves towards rod shape behind the front at $Fr_s = 1.71$. For all three Froude numbers, the grey points behind surge have rod shape in both maps. At a higher Fr_s of 2.13, the turbulence at a higher elevation than the

toe move toward the left side of the Lumley triangle so the turbulence moves towards pancake shape structure between 2D isotropic and 3D isotropic points.

Similarly, for the barycentric map, higher points are near the 2D and 3D boundary. The turbulence at $\frac{h}{d_2} = 0.546$ (orange points) are reaching toward the 3D isotropy or a spherical shape as shown in both methods. At $Fr_s = 2.49$, both maps show that points at the higher elevation locate closer to the left side as pancake shape than the previous Fr_s .

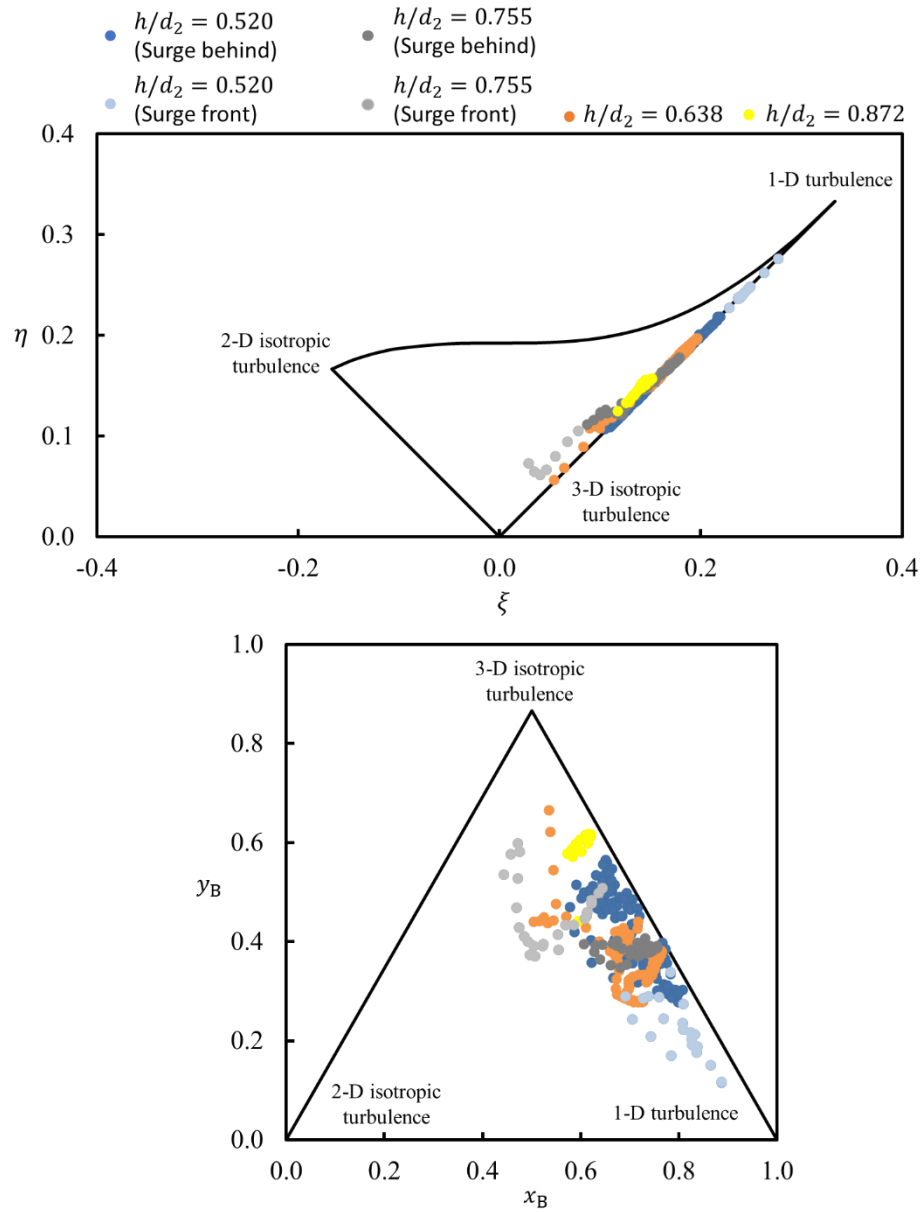


Figure 41. Lumley triangle (upper) and barycentric map (lower) of surge front turbulence at $Fr_s = 1.71$. Blue dots are given at $h/d_2 = 0.520$ at the toe, orange points are given at $h/d_2 = 0.638$ at a quarter of surge, grey points are given at $h/d_2 = 0.755$ at half of surge and yellow points are given at $h/d_2 = 0.872$ at three quarters of surge.

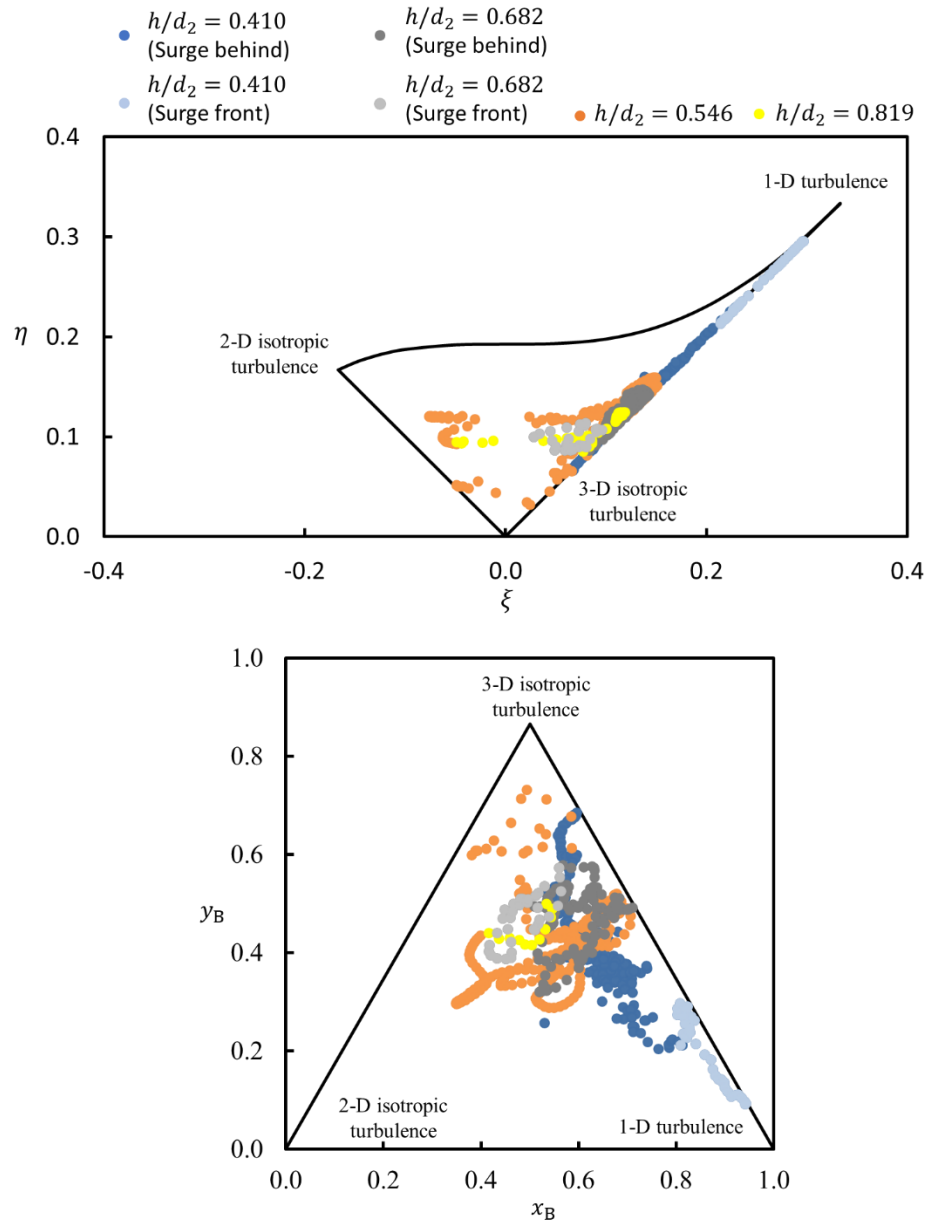


Figure 42. Lumley triangle (upper) and barycentric map (lower) of surge front turbulence at $Fr_s = 2.13$. Blue dots are given at $h/d_2 = 0.410$ at the toe, orange points are given at $h/d_2 = 0.546$ at a quarter of surge, grey points are given at $h/d_2 = 0.682$ at half of surge and yellow points are given at $h/d_2 = 0.819$ at three quarters of surge.

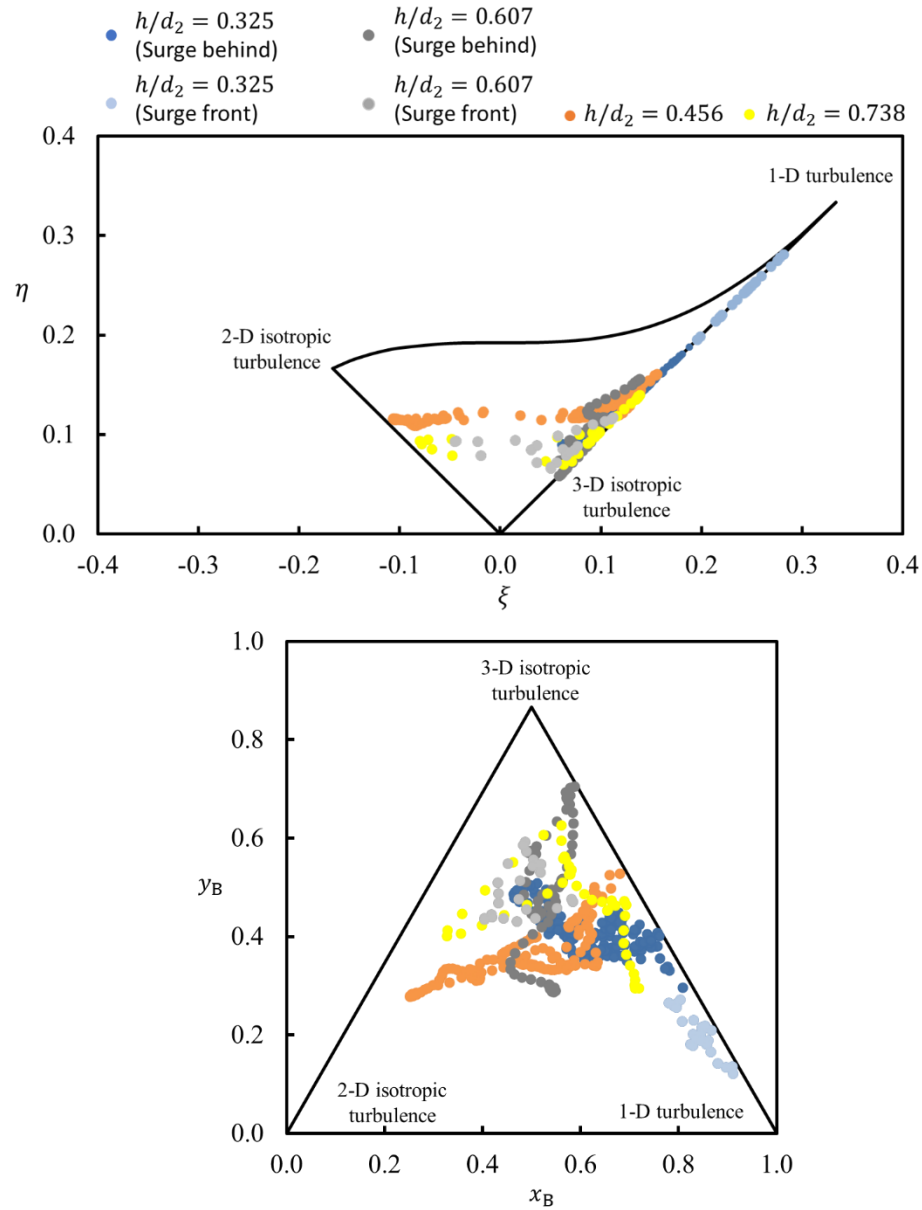


Figure 43. Lumley triangle (upper) and barycentric map (lower) of surge front turbulence at $Fr_s = 2.49$. Blue dots are given at $h/d_2 = 0.325$ at the toe, orange points are given at $h/d_2 = 0.456$ at a quarter of surge, grey points are given at $h/d_2 = 0.607$ at half of surge and yellow points are given at $h/d_2 = 0.738$ at three quarters of surge.

In this chapter flow characteristics have been reported, using different illustrations and figures, that indicate the existence of two mechanisms causing turbulent behaviour of the surge waves. One is the shear instability near the surge toe, which leads to intense TKE in Figures 28(a), 29(a), and 30(a). The intense TKE contributes to peak of surface perturbations shown in the moments plot of water depth in Figure 32(b), 33(b), 34(b) and strong air entrainment at toe in Figures 35(d), 36(d), 37(d). Velocity perturbation also indicates the effect of shear instability in xy -plane, since Figure 40 shows positive turbulent production at toe in xy -plane as well but no turbulent production in yz -plane. Similar observation at surge middle due to the second mechanism phase discontinuity in xy -plane. Lastly, the shear instability also contributes to Q-criterion in Figures 20, 21, and 22 show concentration of vortices near the surge toe which in the anisotropy maps (Figures 41, 42 and 43) are identified as 1D structure near the toe and become rod shape as moving away from the toe for three Froude numbers. All evidence, from anisotropy analysis to air concentration profiles, highlight the role of toe and shear layer initiated from it on the formation of a breaking surge wave.

Chapter 4

Summary and Recommendations

4.1 Summary

Existing computational studies of breaking waves lack the investigation between air entrainment and turbulent characteristics, while many did not account for the 3D structure at the front. Present study conducted a series of numerical simulations of breaking surge waves with Froude numbers of $Fr_s = 1.71, 2.13$ and 2.49 , using a Large Eddy Simulation with k-equation subgrid scale three-dimensional model. By implementing a Volume of Fluid (VOF) solver, it accounted for air entrainment and linkage to the coherent structures across the surge wave. To solve the partial differential governing equations for the variables, discretization schemes are different. The time derivatives are discretized with Euler scheme, convection terms of k_{SGS} and velocity are discretized with upwind scheme and linear upwind scheme for higher accuracy, respectively. For the critical α_w fields, van Leer TVD scheme is used to provide higher accuracy and maintain stability. The computational domain is designed with MOC to generate fully developed surge. Periodic boundary condition is applied with a size to accommodate the largest eddy in the spanwise. In a highly turbulent breaking surge, two mechanisms contribute to instability: formation of shear layer, due to the velocity gradient, at the toe, and wave breaking at the air-water interface due to phase discontinuity. Present analysis of the water surface perturbation patterns, including higher moments, indicate extreme water surface perturbations near the toe. This is attributed to the steep wave front and high level of Turbulent Kinetic Energy

(TKE) at the toe, which leads to strong aeration as well. The simulation also produced air concentration profiles, with the TKE contour and surface perturbations are consistent with the data obtained from existing laboratory observations.

Furthermore, present analysis highlights the role of spanwise perturbations in the development of fully-developed turbulent structures behind the surge wave. Using a periodic boundary condition, this study ensured that domain size does not constrain the growth of spanwise perturbations. The Standard Deviational Ellipses (SDEs) in the xy velocity perturbations cloud for three Froude numbers were oriented towards the second and fourth quadrants, leading to positive TKE production. Figures 40(a) and (c) exhibit the velocity perturbations in the xy -plane for surge toe and middle. For example, at $Fr_s = 2.13$ at toe, u' ranges from -1.37 m/s to 2.73 m/s; v' ranges from -1.82 m/ to 0.91 m/s. The yz velocity perturbations demonstrate that the magnitude of the spanwise perturbations are comparable to other perturbation components. The SDEs, however, suggest that yz perturbations do not contribute to TKE production. Figures 40(b) and (d) exhibit the velocity perturbations in the yz -plane for surge toe and middle. For example, at $Fr_s = 2.13$ at toe, v' ranges from -1.638 m/s to 1.1 m/s; w' ranges from -1.092 m/s to 1.456 m/s. This illustrates the role of spanwise perturbation in the distribution of TKE and the evolution of three-dimensional turbulent structure in a breaking surge wave. The Q-criterion plots visualize the vortices concentrate near the toe due to shear instability. Furthermore, the anisotropy maps quantify the vortices' structure. 1D behaviour is observed at toe and transform to rod shape behind the toe for three Froude numbers. This

along with the dominance of production in the xy - plane, highlight the role of the mixing layer in a breaking surge wave.

The numerical study presented in this thesis, signify the role of the shear layer at the toe on i) air entrainment; ii) surface profile perturbation; and iii) turbulent development at the toe and behind the wave. This study presented the capability of using Large Eddy Simulation model to produce a positive breaking surge wave numerically. High performance computer and parallel processing technique made the simulations of 3D structure and complex nature of surge waves possible. In addition, the selected 2-phases solver effectively exhibited the sharp interface between water and air, and generated a realistic and vivid view of breaking surge waves.

4.2 Recommendations for Future Work

The 2-phases VOF interFoam solver applied in the current case did not distinguish two phases in terms of their fluid properties and velocity field. Therefore, in the future, it is also my interest to study the results based on a multiphase solver that separates two phases. Secondly, further study is required to investigate the distribution of the anisotropy behind the toe and investigate further the interaction of the mixing layer with the surge front. The Lumley triangles can exhibit the anisotropy behaviour of the perturbation but do not indicate the specific directions for the 1D, 2D or 3D behaviour. Therefore, further work is required to investigate anisotropy direction and distribution behind a breaking surge.

Bibliography

- Afzal, A., Ansari, Z., Faizabadi, A. R., & Ramis, M. K. (2017). Parallelization strategies for computational fluid dynamics software: state of the art review. *Archives of Computational Methods in Engineering*, 24(2), 337-363.
- ANSYS, Inc. (2010, December). *Introduction to ANSYS FLUENT*. ANSYS Academic Support. Retrieved from https://imechanica.org/files/fluent_13.0_lecture06-turbulence.pdf.
- ASDSO. (2020). *Dam Failures and Incidents: Association of State Dam Safety*. Dam Failures and Incidents. Association of State Dam Safety. <https://damsafety.org/dam-failures>.
- Barletta, A., di Schio, E. R., Comini, G., & D'Agaro, P. (2009). Wall coupling effect in channel forced convection with streamwise periodic boundary heat flux variation. *International journal of thermal sciences*, 48(4), 699-707.
- Bennetsen, J. C. (2000). Numerical simulation of turbulent airflow in livestock buildings.
- Blenkinsopp, C. E., & Chaplin, J. R. (2011). Void fraction measurements and scale effects in breaking waves in freshwater and seawater. *Coastal Engineering*, 58(5), 417-428.
- Bradbrook, K. F., Lane, S. N., Richards, K. S., Biron, P. M., & Roy, A. G. (2000). Large eddy simulation of periodic flow characteristics at river channel confluences. *Journal of Hydraulic Research*, 38(3), 207-215.
- Chachereau, Y., & Chanson, H. (2011). Free-surface fluctuations and turbulence in hydraulic jumps. *Experimental Thermal and Fluid Science*, 35(6), 896-909.
- Chanson, H. (1995). Air entrainment in two-dimensional turbulent shear flows with partially developed inflow conditions. *International Journal of Multiphase Flow*, 21(6), 1107-1121.

- Chanson, H. (2003). Two-phase flow characteristics of an unsteady dam break wave flow. 30th IAHR Biennial Congress, Thessaloniki, Greece, 24-29 August, 2003. Greece: THEMA.
- Chanson, H. (2004). *Hydraulics of open channel flow*. Elsevier.
- Chanson, H. (2010). Unsteady turbulence in tidal bores: effects of bed roughness. *Journal of Waterway, Port, Coastal, and Ocean Engineering*, 136(5), 247-256.
- Chanson, H., & Tan, K. K. (2010). Particle dispersion under tidal bores: Application to sediments and fish eggs.
- Chanson, H. (2005). Air–water and momentum exchanges in unsteady surging waters: an experimental study. *Experimental Thermal and Fluid Science*, 30(1), 37-47.
- Chanson, H., & Toombes, L. (2002). Experimental investigations of air entrainment in transition and skimming flows down a stepped chute. *Canadian Journal of Civil Engineering*, 29(1), 145-156.
- Chanson, H., Reungoat, D., Simon, B., & Lubin, P. (2011). High-frequency turbulence and suspended sediment concentration measurements in the Garonne River tidal bore. *Estuarine, Coastal and Shelf Science*, 95(2-3), 298-306.
- Chanson, H. (2007). Dynamic similarity and scale effects affecting air bubble entrainment in hydraulic jumps.
- Chanson, H., Lubin, P., & Glockner, S. (2012). Unsteady turbulence in a shock: physical and numerical modelling in tidal bores and hydraulic jumps.
- Chanson, H., & Toi, Y. H. (2015). Physical modelling of breaking tidal bores: comparison with prototype data. *Journal of Hydraulic Research*, 53(2), 264-273.
- Choi, K. S., & Lumley, J. L. (2001). The return to isotropy of homogeneous turbulence. *Journal of Fluid Mechanics*, 436, 59-84.
- Cifani, P., Michalek, W. R., Priems, G. J. M., Kuerten, J. G., van der Geld, C. W. M., & Geurts, B. J. (2016). A comparison between the surface compression method and an interface reconstruction method for the VOF approach. *Computers & Fluids*, 136, 421-435.

- Department of Environment and Resource Management of Queensland. (2009). What Causes Streambed Erosion? *Government Publications*, Queensland, Australia.
- Docherty, N. J., & Chanson, H. (2012). Physical modeling of unsteady turbulence in breaking tidal bores. *Journal of Hydraulic Engineering*, *138*(5), 412-419.
- Emory, M., & Iaccarino, G. (2014). Visualizing turbulence anisotropy in the spatial domain with componentality contours. *Center for Turbulence Research Annual Research Briefs*, 123-138.
- Einwachter, J. (1933). Der Wechselsprung mit gestauter Deckwalze. *Wasserkraft und Wasserwirtschaft*, *28*(17), 200-202.
- Ferziger, J. H., Perić, M., & Street, R. L. (2002). *Computational methods for fluid dynamics* (Vol. 3, pp. 196-200). Berlin: springer.
- Frazao, S., & Zech, Y. (2002). Undular bores and secondary waves-Experiments and hybrid finite-volume modelling. *Journal of hydraulic research*, *40*(1), 33-43.
- Gilmore, F. R., Plesset, M. S., & Crossley Jr, H. E. (1950). The analogy between hydraulic jumps in liquids and shock waves in gases. *Journal of Applied Physics*, *21*(3), 243-249.
- Gualtieri, C., & Chanson, H. (2011). Experimental study of a positive surge. Part 2: Comparison with literature theories and unsteady flow field analysis. *Environmental fluid mechanics*, *11*(6), 641-651.
- Gualtieri, C., & Chanson, H. (2012). Experimental study of a positive surge. Part 1: basic flow patterns and wave attenuation. *Environmental fluid mechanics*, *12*(2), 145-159.
- Greenshields, C. J. (2015). OpenFOAM user guide. *OpenFOAM Foundation Ltd, version*, *3*(1), 47.
- Hunt, J., Wray, A., & Moin, P. (1988). Eddies, stream, and convergence zones in turbulent flows. *Studying Turbulence Using Numerical Simulation Databases-II*, 193.

- Karimpour, S., & Chu, V. H. (2019). The role of waves on mixing in shallow waters. *Canadian Journal of Civil Engineering*, 46(2), 134-147.
- Karimpour, S., & Chu, V. H. (2015). High-order interpolation schemes for shear instability simulations. *International Journal of Numerical Methods for Heat & Fluid Flow*.
- Keough, S. (2014). *Optimising the parallelisation of openfoam simulations*. DEFENCE SCIENCE AND TECHNOLOGY ORGANISATION FISHERMANS BEND (AUSTRALIA) MARITIME DIV.
- Kucukali, S., & Chanson, H. (2008). Turbulence measurements in the bubbly flow region of hydraulic jumps. *Experimental Thermal and Fluid Science*, 33(1), 41-53.
- Kim, J., Moin, P., & Moser, R. (1987). Turbulence statistics in fully developed channel flow at low Reynolds number. *Journal of fluid mechanics*, 177, 133-166.
- Kimmoun, O., & Branger, H. (2007). A particle image velocimetry investigation on laboratory surf-zone breaking waves over a sloping beach. *Journal of Fluid Mechanics*, 588, 353-397.
- Koch, C., & Chanson, H. (2009). Turbulence measurements in positive surges and bores. *Journal of Hydraulic Research*, 47(1), 29-40.
- Kuang, S. B., Li, K., Zou, R. P., Pan, R. H., & Yu, A. B. (2013). Application of periodic boundary conditions to CFD-DEM simulation of gas–solid flow in pneumatic conveying. *Chemical Engineering Science*, 93, 214-228.
- Labovský, J. (2011). Verification of CFD pollution dispersion modelling based on experimental data. *Journal of Loss Prevention in the Process Industries*, 24(2), 166-177.
- Leng, X., & Chanson, H. (2015). Turbulent advances of a breaking bore: preliminary physical experiments. *Experimental Thermal and Fluid Science*, 62, 70-77.
- Leng, X., & Chanson, H. (2016). Coupling between free-surface fluctuations, velocity fluctuations and turbulent Reynolds stresses during the upstream propagation of

- positive surges, bores and compression waves. *Environmental Fluid Mechanics*, 16(4), 695-719.
- Leng, X., & Chanson, H. (2017). Unsteady velocity profiling in bores and positive surges. *Flow Measurement and Instrumentation*, 54, 136-145.
- Leng, X., & Chanson, H. (2017). Upstream propagation of surges and bores: free-surface observations. *Coastal Engineering Journal*, 59(01), 1750003.
- Leng, X., Simon, B., Khezri, N., Lubin, P., & Chanson, H. (2018). CFD modeling of tidal bores: development and validation challenges. *Coastal Engineering Journal*, 60(4), 423-436.
- Leng, X., & Chanson, H. (2018). Transverse velocity profiling under positive surges in channels. *Flow Measurement and Instrumentation*, 64, 14-27.
- Li, H., Rutland, C. J., Pérez, F. E. H., & Im, H. G. (2020). A sub-grid scale energy dissipation rate model for large-eddy spray simulations. *arXiv preprint arXiv:2001.07654*.
- Li, Y., & Chanson, H. (2018). Sediment motion beneath surges and bores.
- Liu, H., Liu, H., Guo, L., & Lu, S. (2017). Experimental study on the dam-break hydrographs at the gate location. *Journal of Ocean University of China*, 16(4), 697-702.
- Lu, S. S., & Willmarth, W. W. (1973). Measurements of the structure of the Reynolds stress in a turbulent boundary layer. *Journal of Fluid Mechanics*, 60(3), 481-511.
- Lubin, P., & Glockner, S. (2015). Numerical simulations of three-dimensional plunging breaking waves: generation and evolution of aerated vortex filaments. *Journal of Fluid Mechanics*, 767, 364-393.
- Lubin, P., Chanson, H., & Glockner, S. (2010). Large eddy simulation of turbulence generated by a weak breaking tidal bore. *Environmental Fluid Mechanics*, 10(5), 587-602.
- MADSEN, P.A. (1981). "A Model for a Turbulent Bore." Ph.D. thesis, Tech. Univ. of Denmark, Inst. of Hydrodynamics and Hyd. Eng., Copenhagen, Denmark, 149

- pages. (also Series Paper No. 28, Tech. Univ. of Denmark, Inst. of Hydrodynamics and Hyd. Eng., Copenhagen, Denmark, 149 pages.)
- Matheou, G., & Chung, D. (2014). Large-eddy simulation of stratified turbulence. Part II: Application of the stretched-vortex model to the atmospheric boundary layer. *Journal of the Atmospheric Sciences*, 71(12), 4439-4460.
- Menon, E. S. (2014). *Transmission pipeline calculations and simulations manual*. Gulf Professional Publishing.
- Mouaze, D., Chanson, H., & Simon, B. (2010). Field measurements in the tidal bore of the Sélune River in the Bay of Mont Saint Michel (September 2010).
- Munters, W., Meneveau, C., & Meyers, J. (2016). Shifted periodic boundary conditions for simulations of wall-bounded turbulent flows. *Physics of Fluids*, 28(2), 025112.
- Murzyn, F., & Chanson, H. (2009). Free-surface fluctuations in hydraulic jumps: Experimental observations. *Experimental Thermal and Fluid Science*, 33(7), 1055-1064.
- Murzyn, F., Mouazé, D., & Chaplin, J. R. (2007). Air–water interface dynamic and free surface features in hydraulic jumps. *Journal of Hydraulic Research*, 45(5), 679-685.
- Murzyn, F., & Chanson, H. (2009). Experimental investigation of bubbly flow and turbulence in hydraulic jumps. *Environmental Fluid Mechanics*, 9(2), 143-159
- Mundo-Molina, M., & Pérez, J. L. D. (2019). Proposed Equation to Estimate the Length of a Hydraulic Jump in a Rectangular Open Channel Hydraulic with Variable Slope, and Its Comparison with Seven Theoretical Equations of Specialized Literature. *Journal of Water Resource and Protection*, 11(12), 1481-1488.
- Misra, S. K., Thomas, M., Kambhamettu, C., Kirby, J. T., Veron, F., & Brocchini, M. (2006). Estimation of complex air–water interfaces from particle image velocimetry images. *Experiments in fluids*, 40(5), 764-775.

- National Geographic Society. (2012, October 9). *Tidal bore*. National Geographic Society. Retrieved December 2, 2021, from <https://www.nationalgeographic.org/encyclopedia/tidal-bore/>.
- Pope, S. B. (2001). *Turbulent flows*. Cambridge university press.
- Rajagopalan, S., & Antonia, R. A. (1982). Use of a quadrant analysis technique to identify coherent structures in a turbulent boundary layer. *The Physics of Fluids*, 25(6), 949-956.
- Rajaratnam, N. (1967). Advances in hydrosience, vol. 4. Ven Te Chow.
- Souders, D. T., & Hirt, C. W. (2004). Modeling entrainment of air at turbulent free surfaces. In *Critical Transitions in Water and Environmental resources Management* (pp. 1-10).
- Safranez K. (1929). Unter. Wechse, 341.
- Takahashi, M., & Ohtsu, I. (2017). Effects of inflows on air entrainment in hydraulic jumps below a gate. *Journal of Hydraulic Research*, 55(2), 259-268.
- Ting, F. C. (2006). Large-scale turbulence under a solitary wave. *Coastal Engineering*, 53(5-6), 441-462.
- Toi, Y. H., & Chanson, H. (2013, September). Turbulent mixing in breaking tidal bores: comparison between field and laboratory data. In *Proceedings of 35th IAHR World Congress, Chengdu, China A* (Vol. 10201). IAHR, Beijing, China, Paper.
- Wang, H., & Chanson, H. (2015). Air entrainment and turbulent fluctuations in hydraulic jumps. *Urban Water Journal*, 12(6), 502-518.
- Wang, H., & Chanson, H. (2015). Experimental study of turbulent fluctuations in hydraulic jumps. *Journal of Hydraulic Engineering*, 141(7), 04015010.
- Wang, H., Murzyn, F., & Chanson, H. (2014). Total pressure fluctuations and two-phase flow turbulence in hydraulic jumps. *Experiments in fluids*, 55(11), 1-16.
- Wang, H., Leng, X., & Chanson, H. (2017). Hydraulic jumps and breaking bores: modelling and analysis. *Proceedings of the Institution of Civil Engineers-Engineering and Computational Mechanics*, 170(1), 25-42.

- Watanabe, Y., Saeki, H., & Hosking, R. J. (2005). Three-dimensional vortex structures under breaking waves. *Journal of Fluid Mechanics*, 545, 291-328.
- Wüthrich, D., Shi, R., & Chanson, H. (2020). Physical study of the 3-dimensional characteristics and free-surface properties of a breaking roller in bores and surges. *Experimental Thermal and Fluid Science*, 112, 109980.
- Xie, P., & Chu, V. H. (2019). The forces of tsunami waves on a vertical wall and on a structure of finite width. *Coastal Engineering*, 149, 65-80.
- Ye, S., Lin, Y., Xu, L., & Wu, J. (2020). Improving Initial Guess for the Iterative Solution of Linear Equation Systems in Incompressible Flow. *Mathematics*, 8(1), 119.
- Yeow, S. C., Wang, H., & Chanson, H. (2016). Effect of a large bed roughness on positive surge propagation in canals. IAHR International Symposium on Hydraulic Structures, Portland, OR, United States, 27-30 June 2016. Logan, UT, United States: Utah State University. <https://doi.org/10.15142/T3600628160853>.
- Yoshizawa, A., & Horiuti, K. (1985). A statistically-derived subgrid-scale kinetic energy model for the large-eddy simulation of turbulent flows. *Journal of the Physical Society of Japan*, 54(8), 2834-2839.
- Zech, Y., Soares-Frazão, S., Spinewine, B., & Le Grelle, N. (2008). Dam-break induced sediment movement: Experimental approaches and numerical modelling. *Journal of Hydraulic research*, 46(2), 176-190.
- Zheng, F., Li, Y., Xuan, G., Li, Z., & Zhu, L. (2018). Characteristics of positive surges in a rectangular channel. *Water*, 10(10), 1473.